1999

An Experimental investigation of the flow boiling heat transfer and critical heat flux in a vertically oriented heated tube

Dominic Peters

AN EXPERIMENTAL INVESTIGATION OF THE FLOW BOILING HEAT TRANSFER AND CRITICAL HEAT FLUX IN A VERTICALLY ORIENTED HEATED TUBE

Dominic T. Peters

Mechanical Engineering Department
Rochester Institute Of Technology
Rochester, NY

A Thesis Submitted
in
Partial Fulfillment
of the
Requirements for the

MASTER OF SCIENCE

in

Mechanical Engineering

Approved by:

Professor_____
Dr. S. G. Kandlikar, Thesis Advisor

Professor_____
Dr. P. Venkataraman

Professor_____
Dr. A. Nye

Professor_____
Dr. C. Haines, Deparment Head

PERMISSION TO REPRODUCE

Thesis Title: "AN EXPERIMENTAL INVESTIGATION OF THE FLOW BOILING HEAT TRANSFER AND CRITICAL HEAT FLUX IN A VERTICALLY ORIENTED HEATED TUBE."

I, Dominic T. Peters, hereby grant permission to the Wallace Memorial Library of the Rochester Institute of Technology to reproduce my thesis in whole or part.

Any reproduction can not be used for commercial use or profit.

1999

FORWARD

I would like to thank my parents, Raymond and Solemna Peters for nurturing my mechanical inclinations. If it weren't for them buying me new toys every time I took apart my old ones to see how they worked when I was a kid, I probably wouldn't be where I am today.

Thanks to my wife Karen are definitely in order. She has been my inspiration and my support throughout my years at RIT. Were it not for her I would be both a nerd and a geek. Buying me a high-powered calculator and presenting it to me with the words "Here, this better get you home earlier at night" says it all.

I would like to express my sincere appreciation to my thesis advisor, Dr. Satish Kandlikar for his motivation and his enthusiasm. He has taught me the value of accomplishment and the rewards of pursuing my interests.

Much appreciation also goes out to the following people

- Robert Zimmer for his support in Labview
- Todd Laging and Sherry Zheng for helping me get this project started in the Boiling and Condensation course
- Jim Greanier, Tom Locke and David Hathaway for their excellent advice
- The inventors of compression fittings, I couldn't live without them

ABSTRACT

Boiling and single-phase heat transfer data were taken for water flowing in a vertically oriented circular tube. Heat fluxes of up to 2MW/m^2 and wall temperatures up to 135°C were obtained in nucleate flow boiling. In film boiling, wall temperatures of up to 400°C were obtained with a ninefold decrease in the heat transfer effectiveness after critical heat flux (CHF) was reached. A computer model was undertaken using computational fluid dynamics (CFD) software to assist in the design process as well as to provide insight into the transport phenomena not realizable from the instrumentation. Validations of the instrumentation used in the experiment were accomplished using single-phase results in conjunction with heat transfer data exported from the CFD model. The accuracy and understanding of the experiment in the single-phase mode was used as a basis to correlate the data in flow boiling. Finally, a database in transient transition flow boiling was created for future study.

Nomenclature

B = Bias Limit [%]

c_p = Specific heat [J/(kg*K)]

D = Channel diameter [m]

f = Friction factor

F_{fl} = Fluid surface parameter

G = Mass flux [kg/(m^2*s)]

h_{lf} = Heat of vaporization [J/kg]

k = Thermal conductivity [W/mK]

L = Channel length

$\dot{m}$ = Mass flow rate [kg/s]

NPSH = Net positive suction head

P = Precision limit [%]

P = Pressure [N/m^2]

q" = Wall heat flux [W/m^2]

r = Radial thermocouple location [m]

T = Temprature [°C,K]

T_A,T_B = Generalized thermocouple designations at z=2

$T_{est,z=zi}$ = First iteration of fluid temperature estimation [°C]

$\Delta T_{fl,total}$ = Total rise in temperature over test section [C°]

T_f = Fluid temperature [°C]

T_2,T_4 = Radial thermocouple designations at z=2

T_{wall} = Wall surface temperature [°C]

$T_{f,x}$ = Local bulk mean temperature at axial length L [°C]

$T_{f,I}$ = Inlet temperature of fluid [°C]

U = Uncertainty limit [%]

z = Axial location within test section [in]

ΔT_{sub} = Liquid subcooling $=T_{sat}-T_{fluid}$ [C°]

Greek Letters

μ = Viscosity [(N*s)/m^2]

ρ = Density [kg/m^2]

Dimensionless Parameters

Bo = Boiling number

Nu = Nusselt number

Pr = Prandtl number

Re = Reynolds number

L/D = Length to diameter ratio

Gz = Graetz number

Subscripts

atm = Atmospheric pressure

CHF = Critical heat flux

D = Heat flux at point D on boiling curve diagram (Forster & Grief analysis)

FDB = Fully developed boiling condition

lo = Single phase

ONB = Onset of nucleate boiling

1. Introduction

Water subcooled flow boiling can accommodate very high heat fluxes under conditions of high mass flux, high liquid subcooling and small channel diameters.

Critical heat flux (CHF) is an important limitation which must be avoided in the design of boiling heat transfer systems. As surface temperatures are increased in nucleate boiling, heat flux increases and reaches a maximum. Beyond this, a transition from nucleate boiling to film boiling takes place resulting in inefficient heat transfer. Exceeding CHF can result in catastrophic material failures from high temperature burnout, such as in meltdowns of liquid cooled nuclear reactors. In the engineering literature, there is presently no accepted model of the post CHF transition boiling phenomena.

There is currently great practical interest in understanding the mechanisms of CHF and being able to predict it. Some components of fusion thermonuclear reactors such as divertors, plasma limiters, or first wall armor are believed to be subject to extremely high thermal operating conditions. Normal and emergency operation of these components often rely on subcooled flow boiling heat transfer to maintain their structural integrity.

1.1 Objective

The objective of the present work is to study the heat transfer characteristics of flow boiling in a circular tube. Emphasis is placed on steady state subcooled flow boiling at high heat fluxes and CHF. Transient

studies in film boiling are also carried out to simulate quenching or emergency cooling situations. This has been achieved by both a literature review and by establishing an experimental test stand to gather data. Recommendations are made for further research based on the results of the present work.

2 Overview of physical phenomena in flow boiling

2.1 Boiling overview

2.1.1 Single phase heat transfer

Knowledge of the single phase heat transfer mechanisms are important in the prediction of the Onset of nucleate boiling as well as the calculation of a single-phase heat transfer coefficient for a boiling heat transfer parameter. Forced convection from the heater surface into the thermal boundary layer and to the bulk fluid is the dominant mode of heat transfer. The flow may be laminar, turbulent or transitional, fully or non-fully developed hydrodynamically and fully developed or thermal entry length problem. Quantization of the heat transferred in single phase forced convection is well established by both empirical and analytical means.

2.1.2 Flow Boiling

Flow Boiling is differentiated from pool boiling by movement of a bulk liquid. In pool boiling, fluid flow is attributed to the buoyancy driven motion of the bubbles coming from the heater surface. The fluid motion in internal flow boiling is caused by a pressure potential difference between the inlet and outlet of a duct, inertial effects and gravitational effects directing the bulk motion of the fluid.

The first bubbles occur on the heater surface at the onset of nucleate boiling (ONB) which is the transition point from single-phase heat transfer.

Bubble activity continues to increase along the wall as more nucleation sites are activated. Partial nucleate boiling is a transition zone where the inlet liquid is in a subcooled state and the wall heat flux is too great to be removed by single phase convection alone. Vapor bubbles are formed at the wall and may make it into the bulk liquid before collapsing.

Fully developed boiling is characterized by rapid boiling on the heater surface and the bubbles detach from the surface. Here the convective contribution becomes insignificant and heat transfer is dominated by nucleate boiling heat transfer. The fluid temperature and vapor generation increases leading into saturated boiling where the liquid and vapor phases are at saturation temperature.

As vapor emanation increases at the surface, a transition in the hydrodynamic flow pattern takes place when liquid cannot be replenished to the wall at a sufficient rate, marking the maximum heat flux attainable. After this occurrence the heat transfer rate drops considerably as the flow boiling dynamics transitions from nucleate boiling to film boiling.

The practical interest in transition boiling is limited because it can be sustained in the steady state only by controlling the surface heater temperature. Physically, liquid contacts in transition film boiling are of short duration and occur randomly over the heat transfer surface. The slope of the heat flux versus wall superheat curve is negative in this region.

Stable film boiling is characterized by dominant effects of the Leidenfrost phenomena, explained in the section below. The tube surface is

covered by a stable vapor film and the liquid flows in a cylindrical core. Heat transfer is accomplished principally through by conduction and convection through the vapor film with radiation becoming significant as the surface temperature is increased.

The Leidenfrost phenomenon refers to classically, the boiling of liquid droplets on surfaces with high degrees of superheat. When a droplet is brought close to such a surface, the liquid may vaporize so rapidly that the vapor production on the side of the droplet facing the surface creates a pressure field which acts to repel the droplet away from the surface. The droplet will hover over the surface supported by the vapor cushion as shown in figure 2a. The Leidenfrost phenomenon's application to the work at hand is in the end of the transition boiling mode and the onset of the stable film boiling mode.

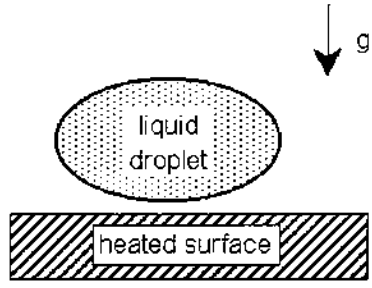

Figure 2a

2.2 Flow patterns in vertical tubes

Flow patterns in vertical flow boiling can be very complex but for general purposes they can be classified in four patterns. The conditions are vertical flow in a uniformly heated tube. The patterns below originate from single phase flow and develop as the bulk fluid and the wall temperature increases.

Bubbly flow occurs when vapor or gas is distributed as discrete bubbles in a continuous liquid phase. In flow boiling, this indicates the occurrence of nucleate boiling.

Slug flow features some of the vapor bubbles moving along the channel in bullet like shapes, taking up nearly the entire cross section. The bubbles are separated by lengths of liquid which may contain dispersed bubbles.

In annular flow, the gas flows through the central core while a liquid layer covers the tube surface. The gas core may contain a large amount of liquid particles.

Mist flow occurs after the dryout of the tube wall from the liquid and the vapor stream carries fine droplets. A variation of this concept is a pattern called inverted annular flow which occurs in film boiling. The tube surface is covered by a vapor blanket and the fluid flows through the core. In a short tube as in the case of this study, inverted annular flow is the more likely possibility for annular flow.

3 Literature overview

3.1 Boiling heat transfer and CHF

Subcooled nucleate boiling has been studied extensively. The correlation of Jens and Lottes (1951) was one of the first to be reported with water data. Kandlikar recently proposed a correlation (1990,1991) based on the wall superheat and the single phase heat transfer coefficient, taking into account the correct physical relationship between q" and ΔT_{sat}.

Reviews have been reported on CHF in subcooled flow boiling with special regard to the high heat flux region (Celata (1998)). There are a few parametric trends that are of practical and intellectual interest which are described below.

The functional dependence of CHF on subcooling appears to be practically linear all the way up to very high subcooling and very high liquid velocity. The absolute increase appears to be constant, with CHF vs. ΔT_{sub} curves being almost parallel.

Mass flux has a direct relationship on increasing CHF in the subcooled region. Boyd (1985) carried out tests at a constant inlet temperature of 20°C. The CHF increases with mass flux G in a less than linear fashion. It is possible to observe that passing from 10 to 40 Mg/m^2s the CHF can be increased up to a factor of about three and more.

The influence of pressure on CHF has been observed to be weak for the range of 0.1 to 5.0 Mpa with other conditions being equal.

Recognizing this, increasing pressure still has the effect of enhancing CHF because of higher inlet subcoolings possible.

Numerous studies on the channel diameter parameter have been conducted with data reported in a total range of 0.3 to 32 mm tube diameter. In general, CHF increases with the decrease of the tube inside diameter, the effect being less significant for decreased mass fluxes. An equation proposed by Doroshcuk et al. (1975a, 1975b) and later improved by Groeneveld et al. (1986) and Celata et al. (1993b) found the following relationship between CHF and channel diameter

$$\frac{(CHF)_D}{(CHF)_{D=8mm}} = \left(\frac{D}{8}\right)^n \qquad \textbf{(3.1)}$$

where $(CHF)_D$ is the the CHF for a diameter of interest and $(CHF)_{D=8mm}$ is a reference value specific to the CHF in an 8mm tube. The exponent n has an accepted value of –0.3.

Bergles (1963) explained the dependence on diameter by stating that a tube with a smaller diameter will have (1) a small bubble diameter, (2) an increased velocity of the bubbles with respect to the liquid and (3) the fluid subcooled bulk closer to the growing bubbles (which collapse in the bulk).

Nariai and Inasaka (1992) explained the relationship in terms of the void fraction, concluding that as tube diameter decreases and mass velocity increases, the thickness of the two phase boundary layer becomes smaller due to the intense condensation effect by subcooled

water at the core region. The void fraction becomes smaller making CHF higher.

Nariai et al (1987) reported that the heated length of the channel is inversely related to CHF, with L/D being the characteristic length. Experiments have also shown the presence of a threshold (L/D > 40) beyond which CHF is practically independent of L/D.

3.2 Theoretical CHF models in Subcooled Boiling

Reviews on efforts to model the main cause of CHF occurrence have be given recently by Katto (1994, 1995), Weisman (1992) and Celata et al. (1994c). The major theoretical approaches can be categorized into 6 major groups.

(1) **Liquid layer superheat limit model**. The resistance to heat transport through the bubbly layer causes a critical superheat in the liquid layer adjacent to the wall, giving rise to CHF. [Tong, et al, (1965)]

(2) **Boundary layer separation model**. This is based on the assumption of an injection of vapor from the heated wall to the liquid stream. This is thought to cause a reduction in the velocity gradient close to the wall. The resulting flow stagnation is assumed to facilitate CHF. [Kutateladze and Leonitiev (1966)]

Fiori and Bergles (1970) conducted studies that demonstrated the weak physical basis for this model.

(3) **Liquid flow blockage model**. It proposes that CHF occurs when the liquid flow normal to the wall is blocked by the vapor flow. [Bergelson (1980)].

(4) **Vapor removal limit and near wall bubble crowding model**. Assumes that the turbulent interchange between the bubbly layer and the bulk liquid may be the limiting mechanism leading to CHF. CHF occurs when bubble crowding near the heated wall prevents the bulk cold liquid from from reaching the wall. [Hebel et al. (1981)]. Weisman and Ying postulated that CHF occurs when the void fraction in the bubbly layer exceeds a critical value of 0.82. Styrikovich et al showed that measured void fraction at CHF ranged significantly, making the validity of this model questionable.

(5) **Liquid sublayer dryout model** is based on the dryout of a thin liquid sublayer underneath an intermittent vapor blanket or elongated bubble, due to coalescent bubbles, flowing over the wall. [Lee and Mudawar (1988), Katto (1990a), Celata et al. (1994)]

(6) **Superheated layer vapor replenishment model.** This describes a limited superheated layer where bubbles can only exist. Because of the accumulation and condensation of the

vapor generated from the heated wall, a thin elongated bubble (vapor blanket) is formed. CHF is postulated to occur when the vapor blanket replaces the superheated layer, coming into contact with the heated wall. [Celata et al (1998a)]

Currently, only the near wall bubble crowding model, liquid sublayer dryout model and the superheated layer vapor replenishment model are receiving significant attention for the prediction of CHF in the highly subcooled region.

3.3 Transition and Film boiling.

Most of the modeling approaches follow the superposition hypothesis of Berenson (1962) that transition boiling is a combination of nucleate boiling during liquid contact and film boiling during vapor contact on the heater surface

$$\bar{q} = F\,\bar{q}_l + (1-F)\,\bar{q}_v \qquad \textbf{(3.2)}$$

Where

$\bar{q}$ = time averaged heat flux

q_l = average heat flux during liquid contact

$\bar{q}_v$ = average heat flux during vapor contact

F = the statistical fraction of surface under liquid contact

In literature, transition film boiling is recognized as the least understood area on the topography of boiling regimes.

France, et. al (1978) examined the thermal fluctuations in transition boiling in liquid metal fast breeder reactors (LMFBR's) where sodium heated steam generators operate at CHF or transition boiling under all or partial load ranges. The major thermo-hydraulic design problem associated with the transition boiling zone was found to be related to the characteristics of the thermal fluctuations induced on the tube walls. Due to the fact that transition boiling and the associated thermal fluctuations may occur under all or most operating conditions, the potential for high cycle fatigue due to thermal stress was found to be an important consideration in determining the lifetime of the tubes.

The periodic local heat transfer has been approached in another way by Chen and Hsu (1995). They outlined the details of an experiment which would allow data to be gathered for the local instantaneous heat flux $q_l(t)$ with transient liquid contact. Their microthermal test probe was capable of a 95 percent response in detecting a step temperature change in 0.1 ms. To capitalize on this, they also caused the drops of liquid to fall at the sensing junction of the probe so that there was control over the location and the surface superheat at the initial moment of contact. They reported average heat fluxes for liquid contact ranging from 10^5 to 10^7 W/m^2 for water as wall superheat was varied from 50°C to 450°C.

4 Experimental Setup

4.1 Scope

This section outlines the purpose and specifications of the components used for the experimental part of the present study. First an overview of the experimental circuit will be presented, followed by a section on the details of each component.

The basis of the experimental work is to acquire heat transfer data in the single phase and boiling regimes for flow in a circular tube. The processed data can then be compared to other engineering methods capable of simulating the physical model.

4.2 Approach

An experimental apparatus was constructed to generate the data required for the present study. First, a copper alloy test section was designed and fabricated and fitted to a fluid flow circuit. Second, appliances were used to vary the heat energy added and extracted from the system. Third, a sophisticated data acquisition system and program was used to collect the data generated.

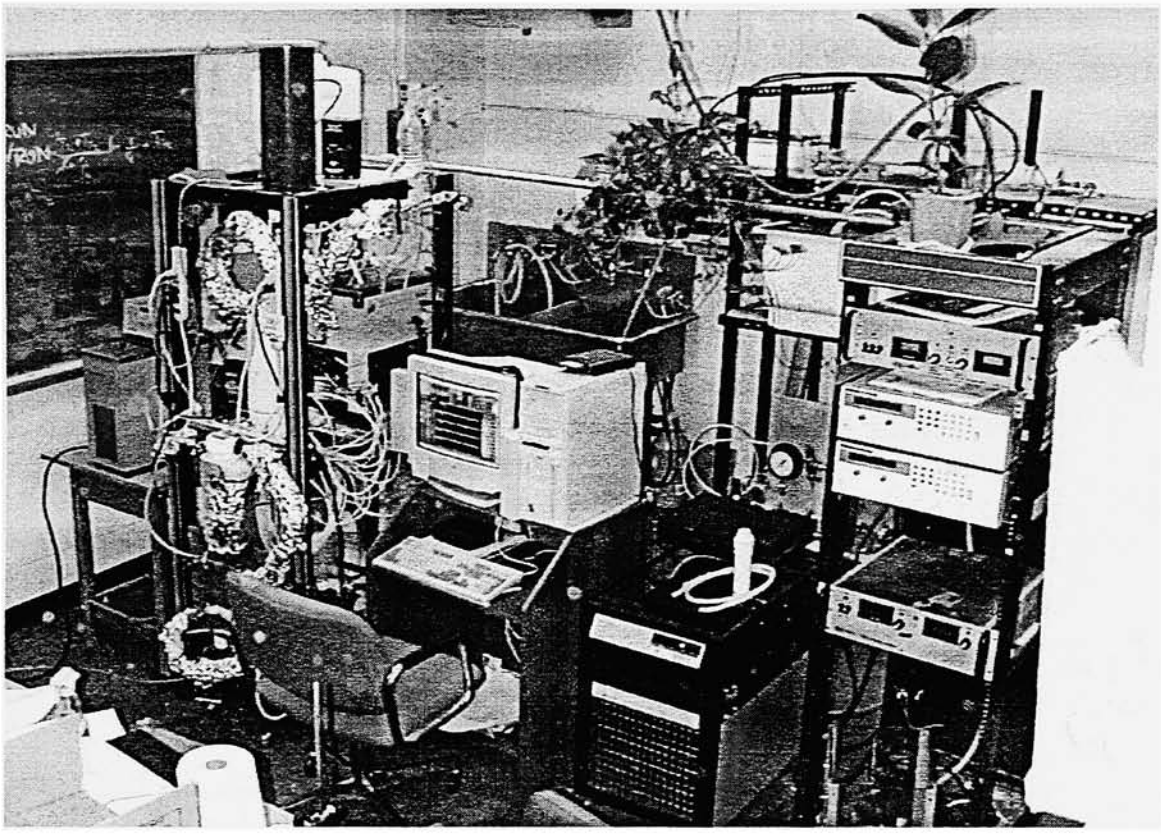

Figure 4a, a perspective view of the entire experimental setup. From left to right: test stand, data acquisition computer, high wattage recirculator, power supplies.

4.3 Overview

4.3.1 Figure 4b shows a schematic drawing of the experimental setup and its components.

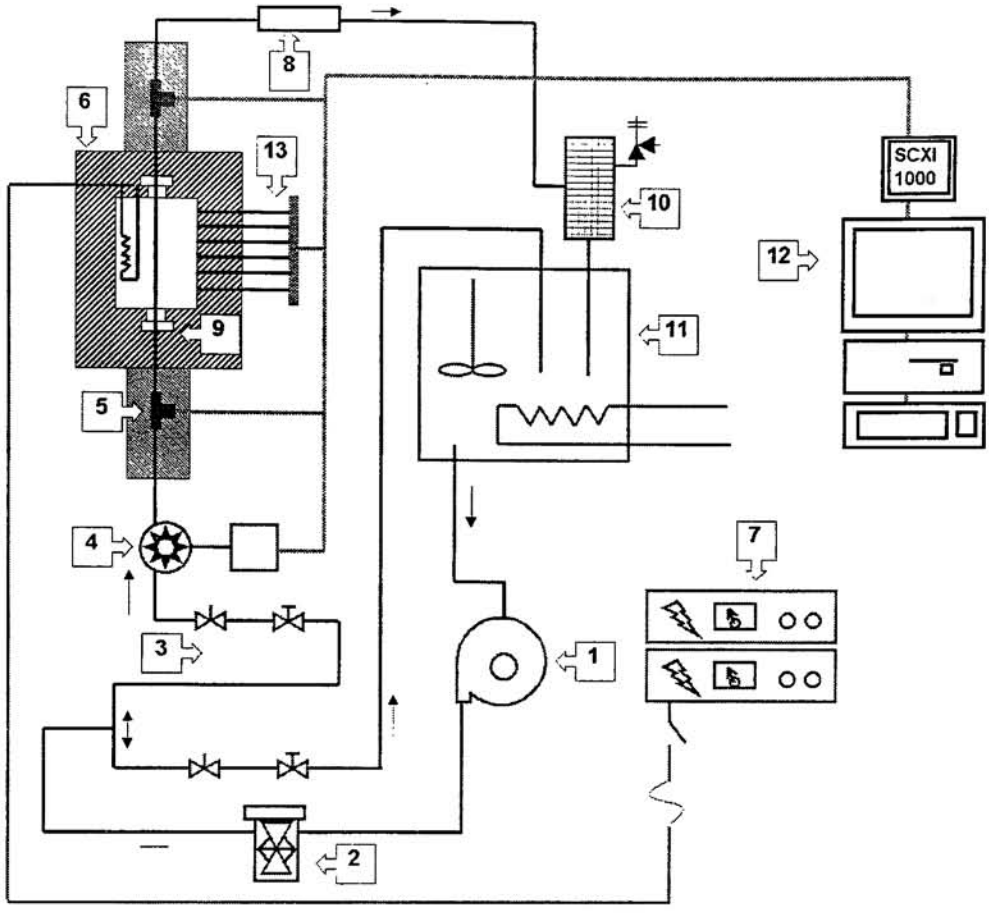

Figure 4b, Schematic representation of the experimental setup showing flow loop, electrical utilities and data acquisition system. Numbered locations are referred to in the body of this section.

Components: (1) Pumps, (2) Filter, (3) Metering valves, (4) Flowmeter, (5) Thermowells, (6) Insulation, (7) Power supplies, (8) Flow visualization section, (9) Fittings, (10) Vapor separation chamber, (11) Refrigeration, (12) Data acquisition, (13) Thermocouples. The test section is shown encased in insulation.

4.3.2 Walkthrough [(*) denotes station on figure 4b]

Fluid is stored in the refrigeration reservoirs (11) where excess heat is extracted from the system. It is pumped (1) from here through a filter (2) and towards the test section. A double set of valves (3) regulates the flow rate, returning the unused portion back to the reservoir. The designated flow runs through a flow meter (4) and into one of two thermowells (5) that measure the inlet and outlet temperatures. The flow (now at known inlet temperature and flow rate) enters the test section fully developed and undisturbed at (9). Temperature measurements are made by the thermocouples embedded in the solid (13) and exported to the data acquisition system (12) along with the flow rate and fluid temperatures. Saturated flow boiling dynamics can be observed through the flow visualization section (8) before the vapor is extracted in the chamber at (10). The fluid is returned to the reservoir and reconditioned to the desired temperature.

4.4 Flow loop

4.4.1 Tubing:

Tubing is used in this setup as the conduit for fluid distribution. It is pliable which reduces the number of junctions and is easily connected with compression fittings. The material and diameter of the tubing varied depending on the service it saw. For the greater portion of the test stand,

the material was polyethylene tubing. In the service it was installed for, it withstood temperatures from the 10°C to 99°C range and pressures of 0 to 138 kPa without yielding. In the legs of the flow loop adjacent to the test section, the higher temperature service required metal tubing. Copper refrigeration-type tubing was used because it remains functional up to 950°C which is well above the 650°C maximum service temperature anticipated in the present work. A leader with an equivalent length of 60 tube diameters was placed before the test section to develop the flow hydrodynamically.

4.4.2 Pumps

The purpose of the pump within the flow loop is to provide a smooth, constant flow rate to the test section. Its functional location in the present work is seen at station number 1 in figure 4b. The backpressure caused by the generation of vapor in the test section restricts the category of pumps to those which provide high discharge heads and moderately low flow rates. In single-phase studies, there are no issues with backpressure at the test section or near-saturation cavitation, so circulation pumps like the 40 kPa (5.5 psi) / 630 cm^3/s (10 gallons per minute) centrifugal pump on the high capacity recirculator are sufficient.

This study focuses on critical heat flux with low subcooled inlet temperature, so a certain type of pump called a positive displacement pump is required because of cavitation issues at near saturation

temperatures. Where conventional centrifugal pumps have capacity-versus-head curves that gently slope downward with increasing flow rate, positive displacement pumps such as gear pumps have near vertical curves, implying that the discharge heads can be very high for one target flow rate. Gear pumps move fluid by squeezing it, not by imparting momentum to it. It is well known that in centrifugal pumps' impeller vanes, the surface of the trailing edge experiences a much lower pressure than the leading edge. If the vapor pressure of the fluid is close to its saturation pressure, it will begin to vaporize. A liquid increases in volume greatly when vaporized, so it is important to keep it in the liquid form to pump it effectively.

The engineering terminology used to express this concept is called the Net-Positive Suction Head (NPSH). The NPSH required is the positive head in absolute units required at the pump suction to overcome losses in the pump and maintain the liquid above its vapor pressure. Effective pumping demands that the NPSH available is greater than the NPSH required. The strength of gear pumps is their ability to operate at low subcooling temperatures without cavitation. The downfall of gear pumps is that the lack of a volute to smooth out the flow results in a somewhat pulsatile output, which could have an affect on the phenomena occurring in the test section. In this study, a series of pressure drops are placed in between the gear pump and the test section to dampen this effect, the

most significant one being the water filter and the remaining being the contractions at the throttling valves.

In summary of this section, the pumps used in this study are the centrifugal pump in the high capacity chiller and the FPUGR103 model gear pump from Omega engineering.

4.4.3 Fittings

Fittings are used to join tubing in the flow loop to the test section, plumbing hardware and appliances. All fittings, with the exception of those belonging to the test section, are expected to seal while withstanding temperatures of 0°C to 100°C, gauge pressures of 0 to 139 kPa (20 psi) and exposure to an aqueous environment. The fittings for the test section require additional material and structural considerations such as temperature service up to 650°C, resistance to temperature cycle induced thermal stresses and gauge pressures of up to 345 kPa (50 psig), making them the most critical (location 9 on figure 4b). All of the 50+ connections are made with commercial type brass compression fittings except for the two test section fittings which were custom fabricated.

A thumbnail image is shown in figure 4c for reference on how the fittings mate together.

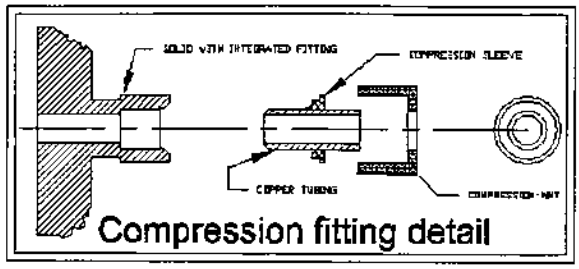

Figure 4c, Detail excerpted from appendix drawing Test section layout.

Each fitting consists of a body, an external ferrule, an internal ferrule, a nut and the tube. The body is machined out of the same stock as the test section to minimize junctions requiring seals. The specifications follow that of commercial compression fittings for 6.35 mm (0.25 inch) tubing, with a pitch of 24 threads per inch.

These fittings are applied by first slipping the nut and the external ferrule over the end of the tube. The tube and the internal ferrule can be received by the body and seated so that the nut can be started. After preloading the set, the end of the tube gets swaged between the two ferrules by the axial compression force between the nut and the body. The deformation combined with the mechanical wedging action creates a leak proof seal. Since no torque is transmitted through the tubing there is no initial strain to weaken the tubing.

Composition wise, the materials are similar and no corrosion problems have been detected during the entire duration of high temperature testing. An experience during the early stages of the project

provided the motivation to use an integral compression fitting. A pilot test section was developed in an aluminum alloy which used stainless steel tubing as leaders and female pipe threads on the test section for attachment. While the stainless steel material was selected for its low thermal conductivity, it behaves cathodically with respect to aluminum according to the galvanic series in seawater.

In electrochemical corrosion, it is the anode that gives up electrons and corrodes. The cathode receives electrons from the circuit. In this case, the two materials were electrically connected by contact. As the reaction progressed, ions were released into the fluid creating a secondary circuit through an electrolytic solution. The result was catastrophic disintegration of the aluminum threads, stripping them.

Sealing was also a problem in the pilot model. The tolerances in the pipe threads were too coarse for tight sealing, especially when differential spatial expansion took place at higher temperatures. Teflon tape could be used at temperatures below 300°C, but it broke down up above this. Copper exhaust manifold silicone was also tried as a gasket, but disintegrated. Based on these events a new fitting strategy was sought and was found in compression fittings.

4.4.4 Vapor separation chamber

Under certain test conditions it is not desirable to have saturated steam discharging directly into the water bath. The refrigeration capacity

of the baths are limited and the extra heat added from the discharging steam adds unnecessary heat load. A separator was constructed that would allow the outflow of the test section to reach the bath in condensed form. In this way it would be easier to maintain the bath at a constant temperature throughout an experimental run. The separator was fabricated from a 13.97 cm (5.5 inch) inner diameter by 44.45 cm (17.5 inch) tall schedule 80 PVC pipe with the ends capped in acrylic sheet. This is designed to handle a temperature range of 20°C to 120°C at atmospheric pressure. An image of the chamber is shown in figure 4d and is also indicated schematically at number 10 on figure 4b.

The wet steam is injected through a nozzle towards the top of the unit and allowed to expand. An aperture at the top can be adjusted to permit variable amounts of steam to escape and cold air to circulate. Condensate is collected from two taps at the bottom and is then returned to the recirculator bath.

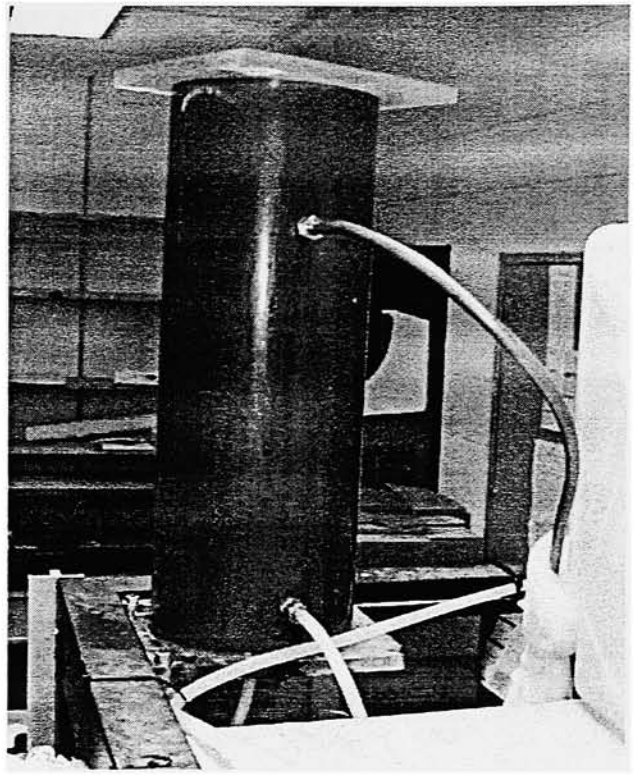

Figure 4d, Vapor separation chamber

4.4.5 Valving

Valving devices are necessary to meter the flow to the test section as well as to provide emergency cutoffs to any part of the test section in the event that the flow of water is not desired. See figure 4e for an image and number 3 on figure 4b for the location of the valves within the system. The two types of valves installed are gate valves and ball valves in brass bodies. They are rated at over 150°C temperature and 1035 kPa (150 psig) pressure. The ball valves are the one-quarter turn type for on-off operation and the gate valves require about 10 turns open to close, so they are suitable for flow metering service.

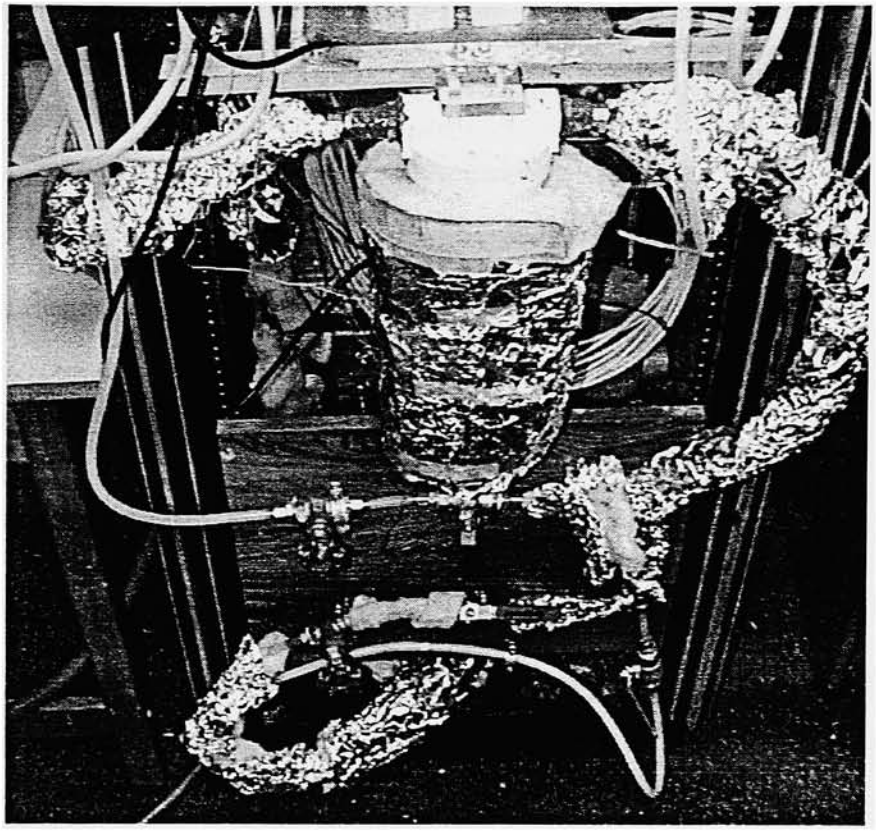

Figure 4e, A section of the flow circuit showing canister filter and metering valves.

4.4.6 Filtration

Fouling and its effects on convective and boiling heat transfer are of concern in this experiment. The deposition of a film or scale on the surface can greatly increase the resistance to heat transfer between the surface and the fluid. (Chenoweth & Impagliazzo 1981). A cartridge type water filter was installed on the main leg of the flow loop to filter out particles greater than 5 microns. The cartridges are composed of a fibrous fabric that are replaced after every 30 hours of operation.

4.4.7 Insulation

Insulation for this test stand is categorized by temperature service. The test section requires insulation to isolate it up to around 650°C, which is the heaters' burnout temperature, as well as to provide the adiabatic-type boundary condition at the walls of the test section.

Calcium silicate insulation has a maximum service temperature of 660°C and a thermal conductivity of 0.055 W/mK at 310K to 0.104 W/mK at 750K. (Incropera and Dewitt, p 835) It is available in sheets and annular shapes that are easily machined to customize a shape for the test section and its fittings. Fiberglass insulation (k=0.04 W/mK at 300K, Incropera and Dewitt, p 834) is used for sealing air gaps in the seams of the calcium silicate blocks and is also used as insulation for the tubing.

All tubing from the water bath to the test section was insulated with 1.27 cm (0.5 inches) of fiberglass insulation and appliances such as the filter were insulated with 5.08 (2 inches) of fiberglass insulation with an R factor of 11. To keep glass fibers from getting airborne, prevent permeation of water into the insulation and provide resistance to radiation losses, foil aluminum was used as a jacket. Location 6 in figure 4b shows the test section insulation shell schematically. The insulated test section can be seen in figure 4g and figure 4e shows the tubing insulation.

4.4.8 Recirculation and refrigeration

Two recirculators have been used in this study, a Brinkmann model RC-20 heater/chiller and a VWR model chiller. The primary purpose of the recirculating baths are to keep a reservoir of constant temperature water to feed into the test section, but they have also been used for their pumps and to degass water. The RC-20 has a refrigeration capacity of 800 watts and the VWR has a capacity of 1600 watts.

4.4.9 Flow visualization section

A transparent tubular flow visualization section was constructed by splicing a piece of glass tubing into the test-section-discharge line. A high intensity fiber optic light was used to illuminate the flow. Its purpose of this section was to provide qualitative insight into the hydrodynamics of two-phase flow by visually noting the change in the superficial liquid and gas velocities as the heat flux was varied at the test section and the amount of vapor generated changed. The section was fashioned from a 9.5 mm (0.375 inch) inner diameter tube with a 10.2 cm (4 inch) viewing section. It is recognized that the diameter differs between this section and the test section, so dimensional similarity is used to conceptualize the flow.

4.4.10 Thermowells

Two main thermowells were fabricated to provide a location to measure the temperature of a fluid stream without diverting or disturbing it.

The fluid stream was maintained in an in-line direction by adapting thermocouples to compression fitting "tees". The main concept was to cut a straight piece of metal tubing, pipe it full of RTV silicone and then insert an epoxy beaded waterproof thermocouple into the tube such that the wire was sealed in the tube with an exposed end on the fluid side. When assembled with the compression nut over the tubing, the thermocouple bead is situated in the middle of the fluid stream and there is absolutely zero leakage. These are found at location 5 on figure 4b.

4.4.11 Test section

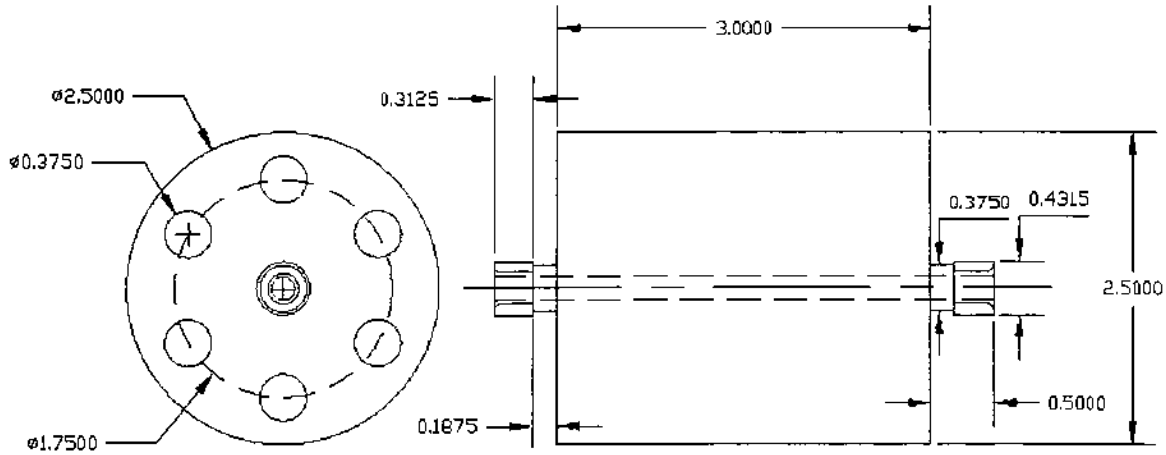

Figure 4f, Dimensioned drawing in inches of the test section

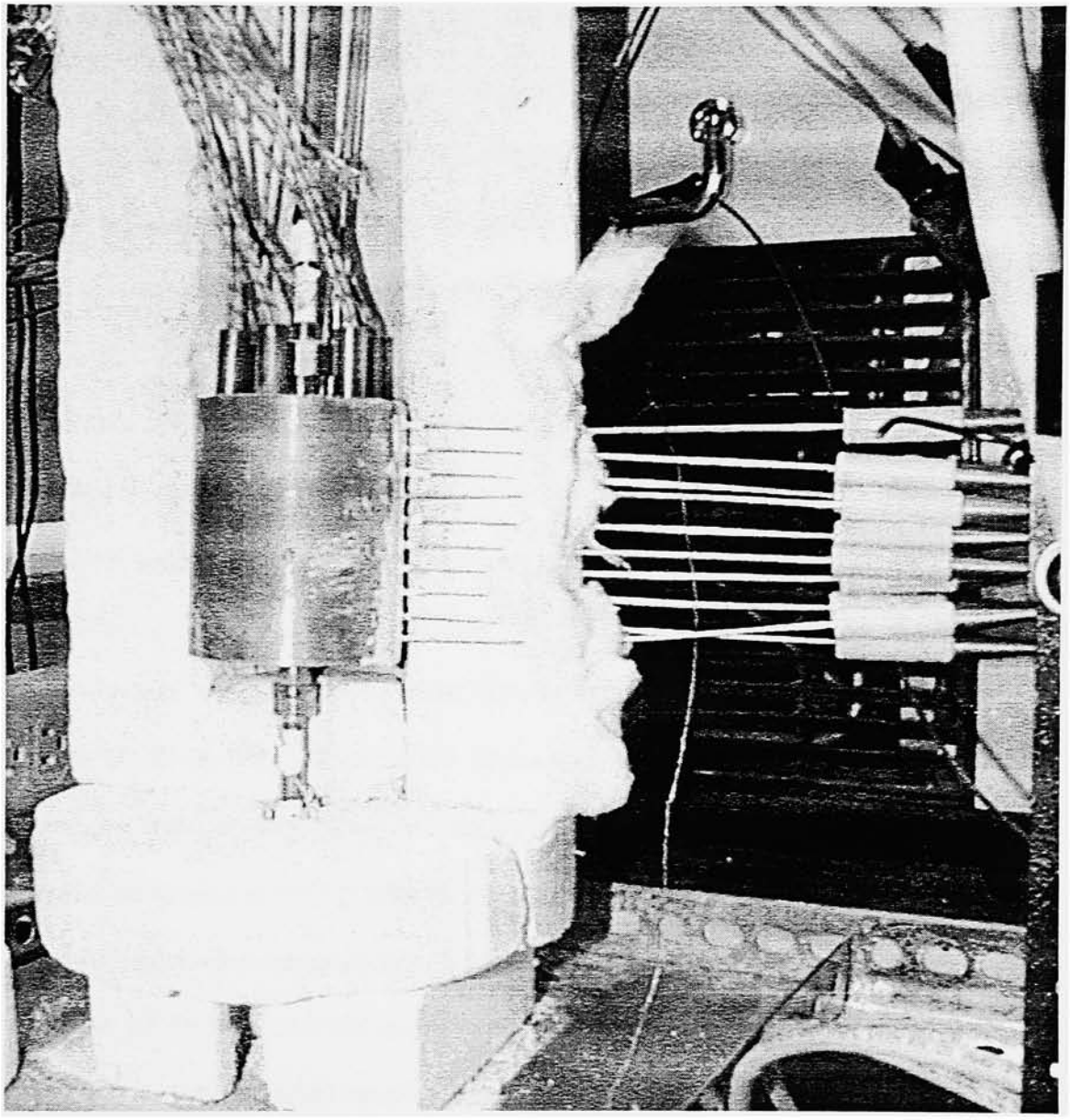

Figure 4g, The test section, exposed showing insulation, heaters, thermocouples and fittings.

The goal of this experiment was to acquire heat transfer data for water flowing through a heated tube. To quantify the heat transferred, knowledge of the heat flux and the surface temperature is required with accuracy. The approach taken was to deliver heat energy through a solid

and measure the steady state changes in temperature within the solid. This test section concept is somewhat like having a tube with a wall thickness to diameter ratio of 10 (t/D=10) as opposed to a ratio of 0.1 (t/D=0.1) such as with stainless steel tubing used by Aggour (1979). Heat rates and temperatures are calculated based on the measured temperature gradient and known dimensions rather than inferring them from outer tube surface temperature measurements and electrical resistive heat generation rates.

The test section consists of a machined cylindrical rod that has been fabricated out of C36000 copper alloy. The material is also referred to as "yellow brass" or "free cutting brass" and its constituents include 61.5% Cu, 35.5% Zn and 3% Pb. Its mass characteristics include a density of 8.5 g/cm^3. Its Thermal properties include a specific heat of 380 J/kg K and a thermal conductivity of 115 W/m K. All properties given in this paragraph are referenced to a temperature of 20 degrees Celsius.

The 63.5 mm (2.5 inch) rod was modified by boring a polar array of holes to insert 6 cartridge heaters and center-drilling a 4.7625 mm (0.1875 inch) channel for fluid flow. Figure 4h shows a photo micrograph of the surface finish created by drilling.

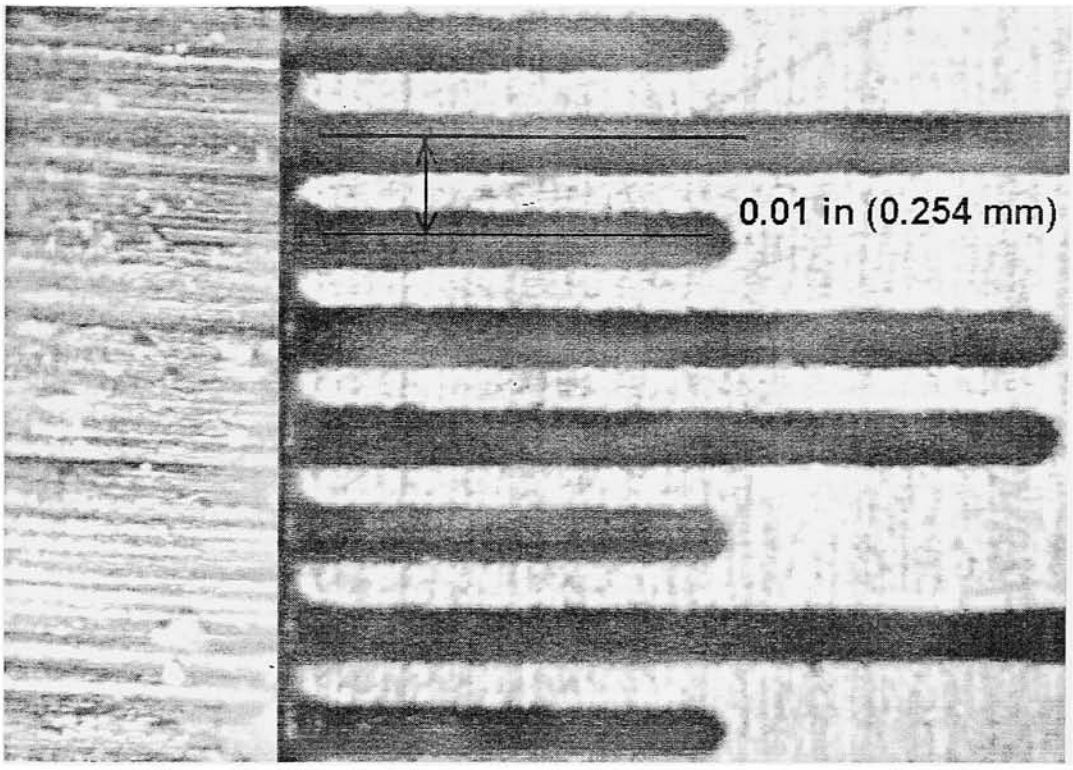

Figure 4h, Magnified view of the channel surface finish that was produced by drilling. Surface roughness was estimated at 1.5 micrometers. (60μ in). (Surface at left, scale on right)

The methods of attachment to the flow loop in this case are two integral compression fittings. The present test section has two custom made male compression fittings which capitalize on the mechanical wedging action of compression rather than the mechanical interference of the bare threads. This promotes a clean seal at high temperatures and pressures and allows the use of an all brass fitting system.

Sixteen 1.5875 mm (0.0625 inch) holes were drilled in the test section for temperature instrumentation providing traverses in the radial and axial directions, as seen in Fig. 4i below.

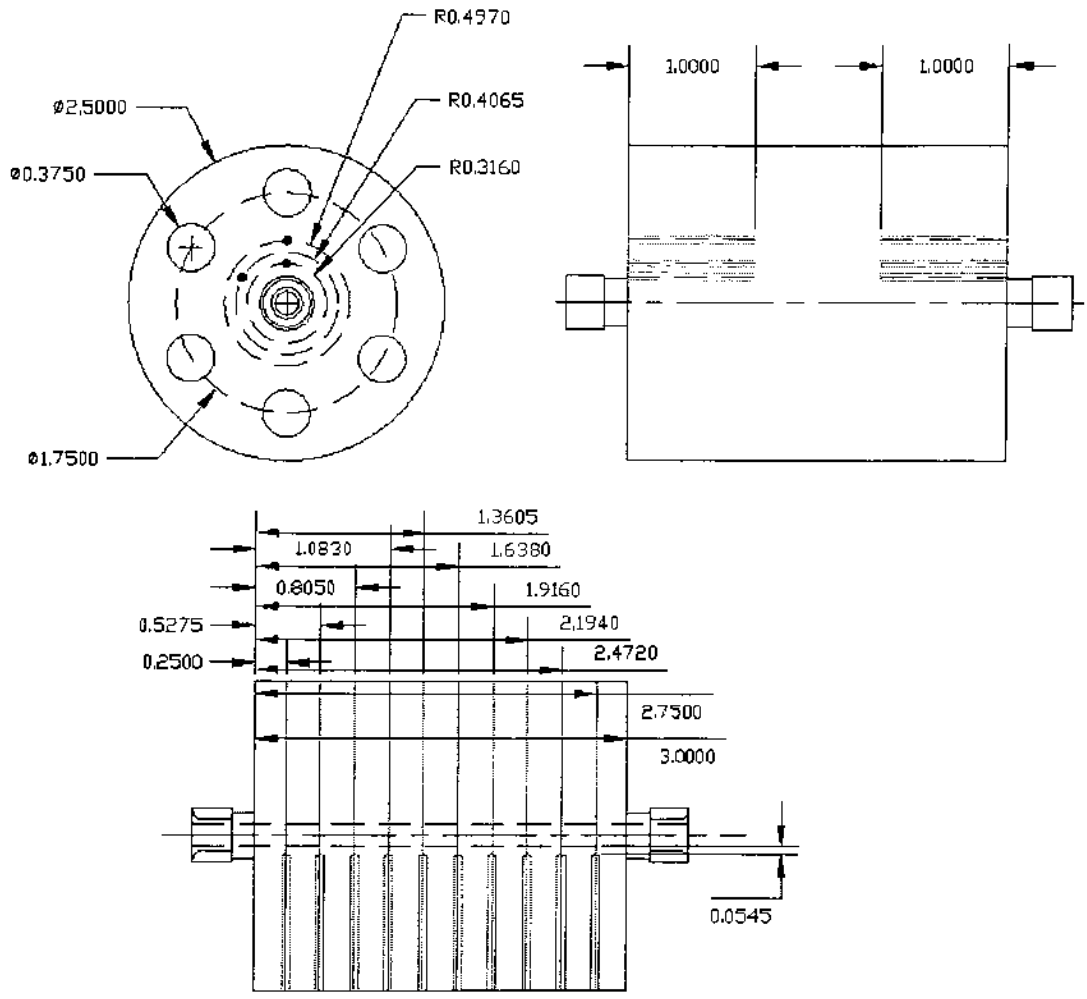

Figure 4i, Thermocouple instrumentation hole location details (inches)

4.5 Power supply

Two power supplies were used to provide enough wattage to the heater array and carry the phenomena inside the test section through the different boiling regimes, especially in the heating up mode. The master

power supply was the EMS 150-16 with a maximum voltage of 150VDC and current of 16amps gives a capacity of 2.4 kW. The secondary power supply was the EMS 150-12 which has a maximum voltage of 150VDC and a current of 12amps, yielding a capacity of 1.8 kW. Neither of the power supplies was rated with an output ripple voltage greater than 200mV nor an output ripple current greater than 20mA. Location 7 in figure 4b depicts these units.

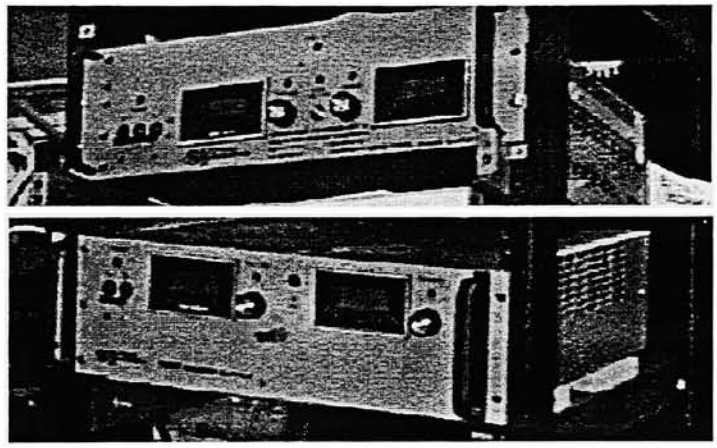

Figure 4j, The DC power supplies used. The 2.4 kW model is shown at the top and the 1.8 kW model is shown at the bottom.

4.5.1 Power distribution

10 gauge wires (AWG) carried the power from the supplies to a box containing copper bus bars. As shown in figure 4k, the circuits of each heater were connected, with one leg passing through a 5 amp fuse panel. At this location, the continuity of each heater circuit can be verified in case of burnout.

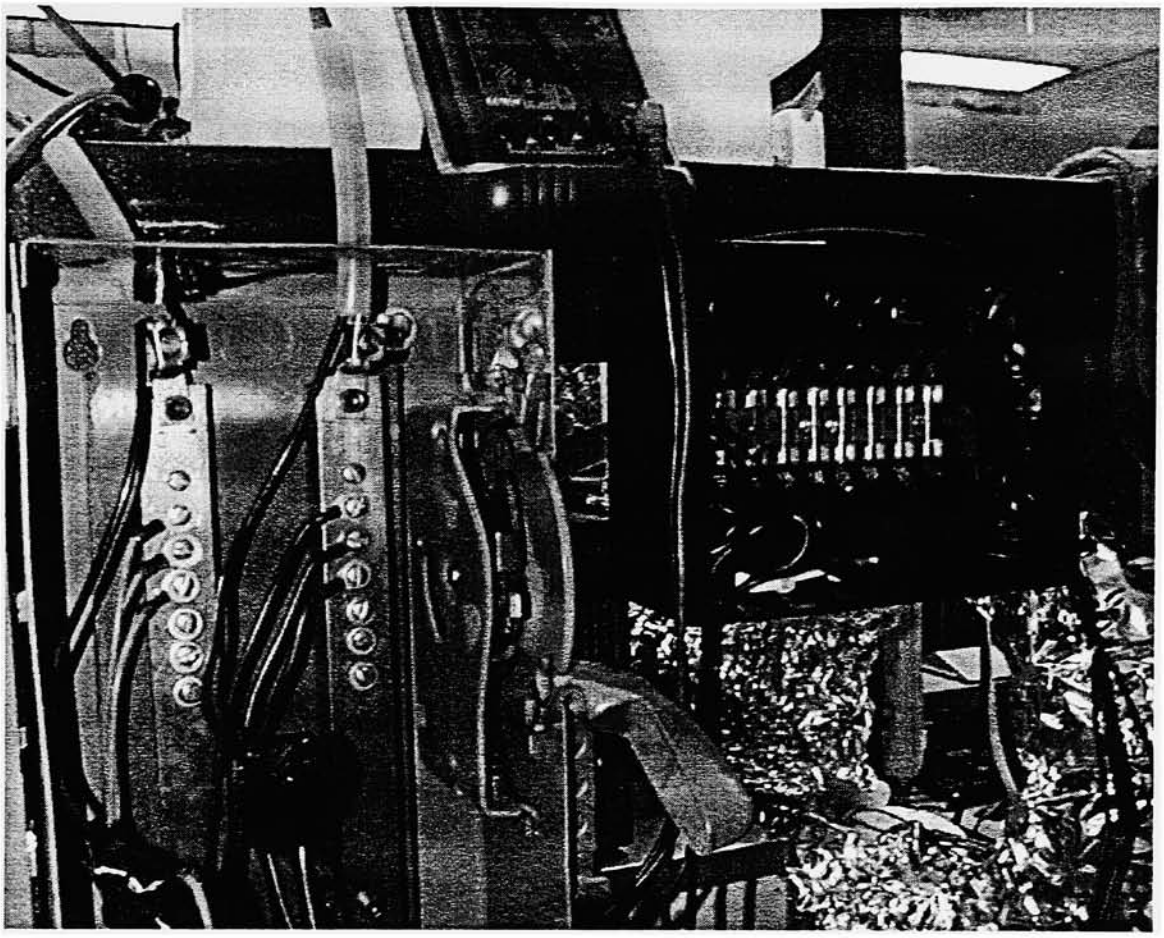

Figure 4k, Power distribution box showing bus bars (left). Also shown is fuse panel providing over current protection to each heater (right)

4.6 Data acquisition

The data acquisition used is Labview from National Instruments inc. The components consist of the transducers, signal conditioning modules, data acquisition and analysis hardware, a personal computer and the software.

4.6.1 Transducers

The transducers in the test stand were either thermocouples or a flow transducer. K type thermocouples were chosen for their performance and reliability at high temperatures. Specifications for the thermocouple probes embedded in the test section solid include those consistent with the Omega model KMTSS, which are a 304 Stainless Steel sheath and a grounded thermocouple bead junction to the tip. Omega uses a two thermocouple alloys in the manufacture of these K type models, which are Chromega and Alomega (Nickel-Chromium). These conform to the NIST standard ITS-90. The manufacture's temperature range spans –328 to 2282 degrees Fahrenheit or –200 to 1250 degrees Celsius. Limits of error are specified at 2.2 °C or 0.75% above 0°C; 2.2°C or 2.0% below 0°C, whichever is greater. Refer to section 5 for information on the calibration procedure used. The length of each K type thermocouple probe was supplemented with about 1m (3.5 feet) of shielded extension grade wire. The junction where the extension wire met the board was made at a screw-down terminal block which was attached to an isothermal block with cold junction compensation. The thermocouples located in the thermowells were Omega thermocouple grade type T with epoxy coated beads.

One transducer was used in the axial turbine flowmeter. The signal of this transducer was of a different scale, so it was read into a separate module in the signal conditioner. The flowmeter required excitation, so it was not a passive transducer like the thermocouples. A separate Hewlett-

Packard 6216C (0-25V, 0-0.4A) power supply was used to excite the flowmeter circuit, which in turn sent a 0-5 volt output to the data acquisition proportional to the flow rate in gallons per minute.

4.6.2 Signal conditioning

The signal conditioning hardware was a very important component of this data acquisition system. This component interfaces the raw signals and the sensor output to the data acquisition board. Signal conditioning improves the quality and reliability of the data acquisition system by amplifying low level signals, isolating and filtering signals; the goal being to produce noise free high level signals for the Data Acquisition board. All of the thermocouples are very low level output and change typically 7mV to 40mV for every 1°C change in temperature. Accurate temperature measurement requires signal conditioning that can amplify the signal with high gain and low noise. Filtering is used to remove unwanted signals from the signals being measured such as noise caused by computer monitors and fluorescent lighting. The signal condition module used for this test stand is a SCXI-1000 from National Instruments and its sub-components are the SCXI-1102/1303 and the 1180/1302. All of the thermocouple channels are connected to the SCXI-1102/1303 sub-module which includes an amplifier and filter for each channel. Amplification can be programmed for a gain of 1 or 100 depending on the range desired, and the amplified signal is then passed through a filter whose cutoff frequency is 2Hz. The 1303 half of the sub-module includes the cold

junction sensor input for an isothermal terminal block which is a significant component for thermocouple accuracy. Since the connections from the extension wires to the terminal block create parasitic (Seebeck) voltages, they need to be compensated for by indexing them in the software based on a reference temperature. The SCXI 1180/1302 is simply a terminal block with a feedthrough panel used to detect 0-5 V DC analog signals and refer them to the Data Acquisition (DAQ) card.

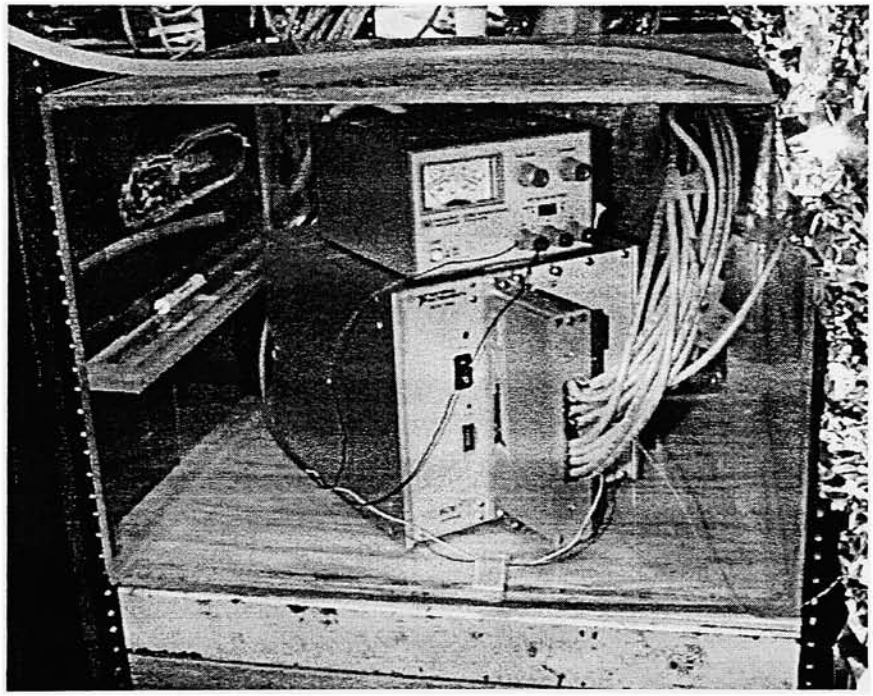

Figure 4l SCXI 1000 signal conditioning hardware used by Labview

4.6.3 Data acquisition

The heart of the data acquisition system is the DAQ card. For this system, there is a AT-MIO-16-E-1mounted inside the computer chassis to provide the interface with the software and the conditioned input signal. The three most important aspects of a data acquisition card are the sampling rate, the resolution and the input range. The performance of this card gives a sampling rate of up to1.25 MS/s ($1.25*10^6$ samples per second). This is the specification of the number of observations per second is made. The faster the sampling rate, the greater the number of points will be acquired in a unit of time. The result is a better temporal representation of the original signal. The signal must be sampled at a sufficiently high rate to capture its essence. If the signal is captured too slowly, it will appear aliased- or appear to be a completely different frequency. The application of sampling speed as it applies to this research is slight in the steady state, but significant for the transient cases. Resolution refers to the discretization of the analog signal and the conversion into a signal that the computer can interpret, or digitization. The signal is broken down in the time and the amplitude domain, the time discretization being handled by the sampling rate. Quantization of the signal amplitude depends on the resolution of the analog to digital conversion card (ADC), the units being the number of binary digits (bits). For an example, 10 bits can be used to resolve a unit change in voltage much more closely than a 3-bit representation. The resolution of the AT-MIO-16-E-1 card is 12 bits with 16 single ended analog inputs. The full

input range for this board is +/-0.05 to +/-10 volts, so the portion of that range focused on with the 12 bits available will determine the discretization available.

4.6.4 Software

The signal now digitized and in the vast domain of the processing circuitry can now interface with the software which is Labview 4.1. It uses a high level programming language called "vi" to create and run virtual instrument panels. In general, the goal of the instrument panel is to establish connections between input channels and indicators, (analog and graphical) to inform the user of the physical conditions as well as to provide file dialog. The file outputs here were post-processed in Excel spreadsheets. Figure 4m shows the front panel that was used in this study to monitor the variables as well as to execute file dialog. A subroutine of this program is presented in figure 4n for an appreciation of the program's sophistication.

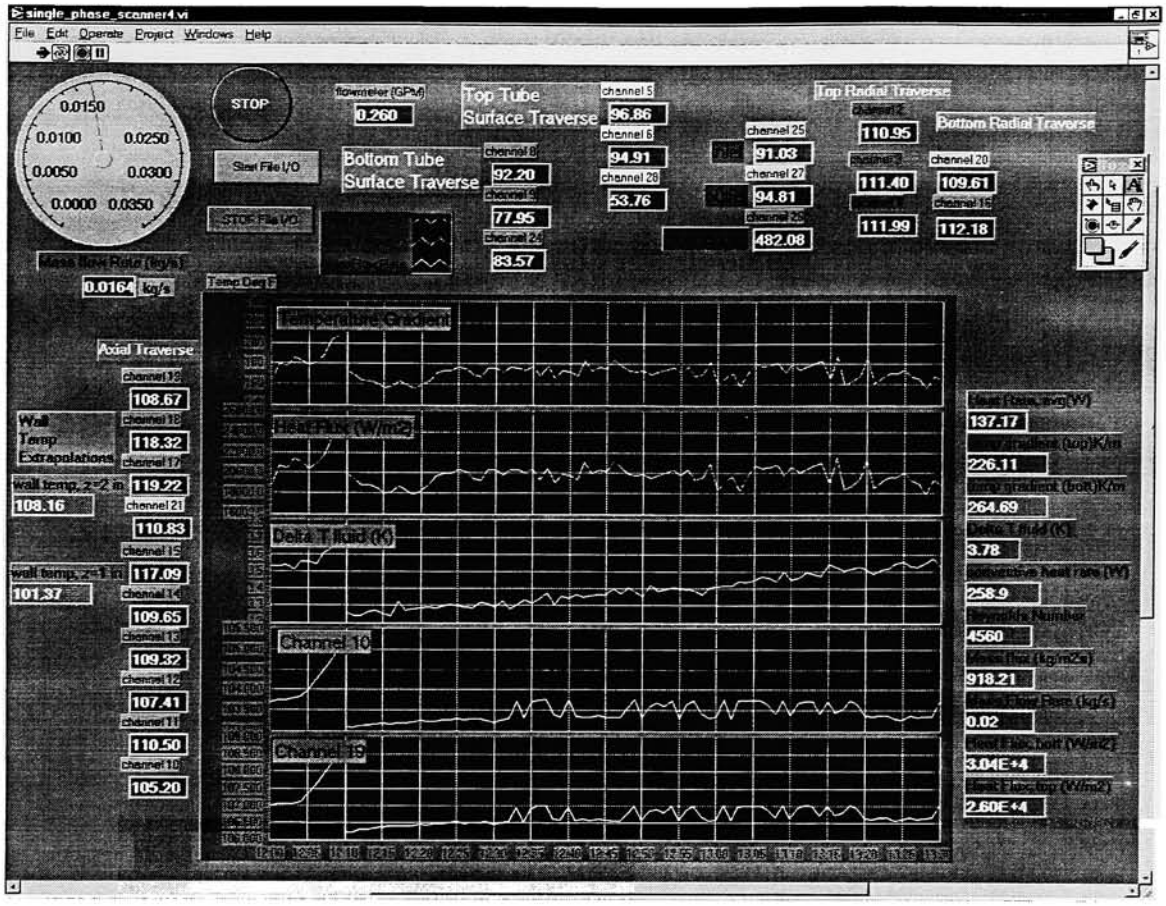

Figure 4m, Labview front instrument panel "VI"

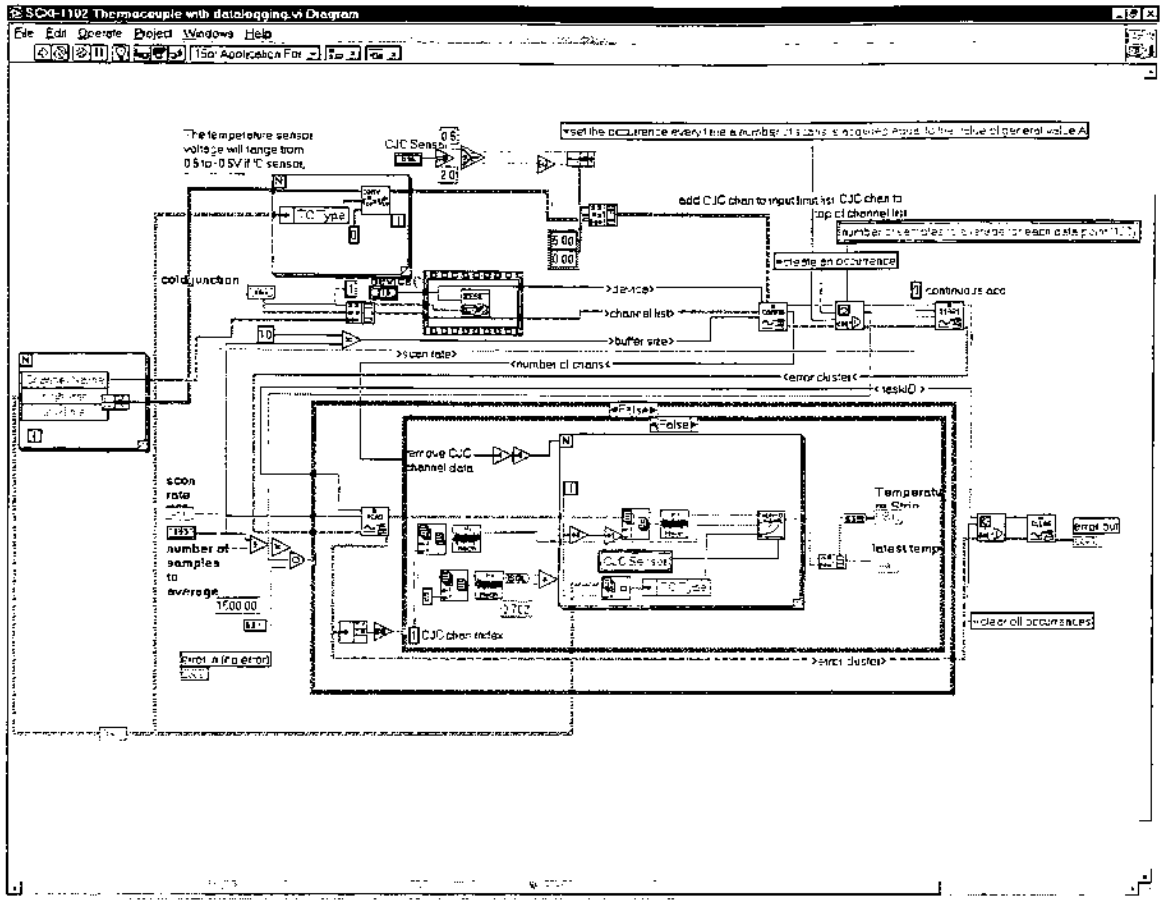

Figure 4n, Labview program in the graphical "vi" language

5 Instrument calibration

5.1 Introductory remarks

This section contains information relating to the scope and procedure for calibrating the thermocouples used in this study.

5.2 Scope

Thermocouples are passive transducers that produce low level voltage outputs proportional to temperature. Manufacturing methods and impurities can affect the response of the probes with errors in accuracy of +/- 1.5K not uncommon. Calibration procedures were used to establish the accuracy and precision of each individual transducer and compare the measurements to accepted error criteria. An equation was derived to compensate for errors built into the transducers when it was greater than the error criteria. Figures are provided in 5a and 5b to illustrate the range of error inherent in the measurements.

5.3 Thermocouple calibration procedure

5.3.1 Preparation

The reference points for the calibration of the thermocouples were the freezing point and the saturation point of water at one atmosphere pressure. All thermocouple beads, if exposed, were coated with epoxy to prevent errors from short-circuiting around the beaded junction. A virtual instrument panel (vi) with file output is opened up and is prepared to run. The thermocouples as a group are prepared by bundling them together and rigging them on a laboratory stand. Crushed ice placed in an insulated dewar flask and a small

amount of de-ionized water is added to the ice to create a saturated solution of ice and water at 0 deg C.

5.3.2 Procedure

The bundle of thermocouples is let down into the dewar so that the thermocouple junctions are completely submerged in 0°C water ice solution. Reflective aluminum foil is used to sleeve the wire/dewar interface and help maintain static conditions. At least 15 minutes is allowed for the system to reach equilibrium before taking any calibration data. The vi program is run for 20 seconds with file output and is stopped. The system is stirred and the process repeated again for a total of 5 runs. Only runs observed to meet steady state conditions are considered. Post processing is done in a spreadsheet for the data collected by averaging the time lapsed values into a single row of values for each run. The summary of these is plotted to determine each thermocouple's accuracy and precision.

For the boiling saturation point, the thermocouples are submerged into a beaker of de-ionized water on a hotplate. The saturation temperature is taken as the fully developed nucleate boiling state and the local atmospheric pressure is also read. The system is insulated radially and aluminum foiled near the top so that steam can escape. The same protocol used above for freezing is used at this temperature.

5.3.3 Results

The results are plotted in figures 5a and 5b for the saturation and freezing point of water, respectively. Each thermocouple number on the x axis contains the results of 5 trials in degrees Celsius.

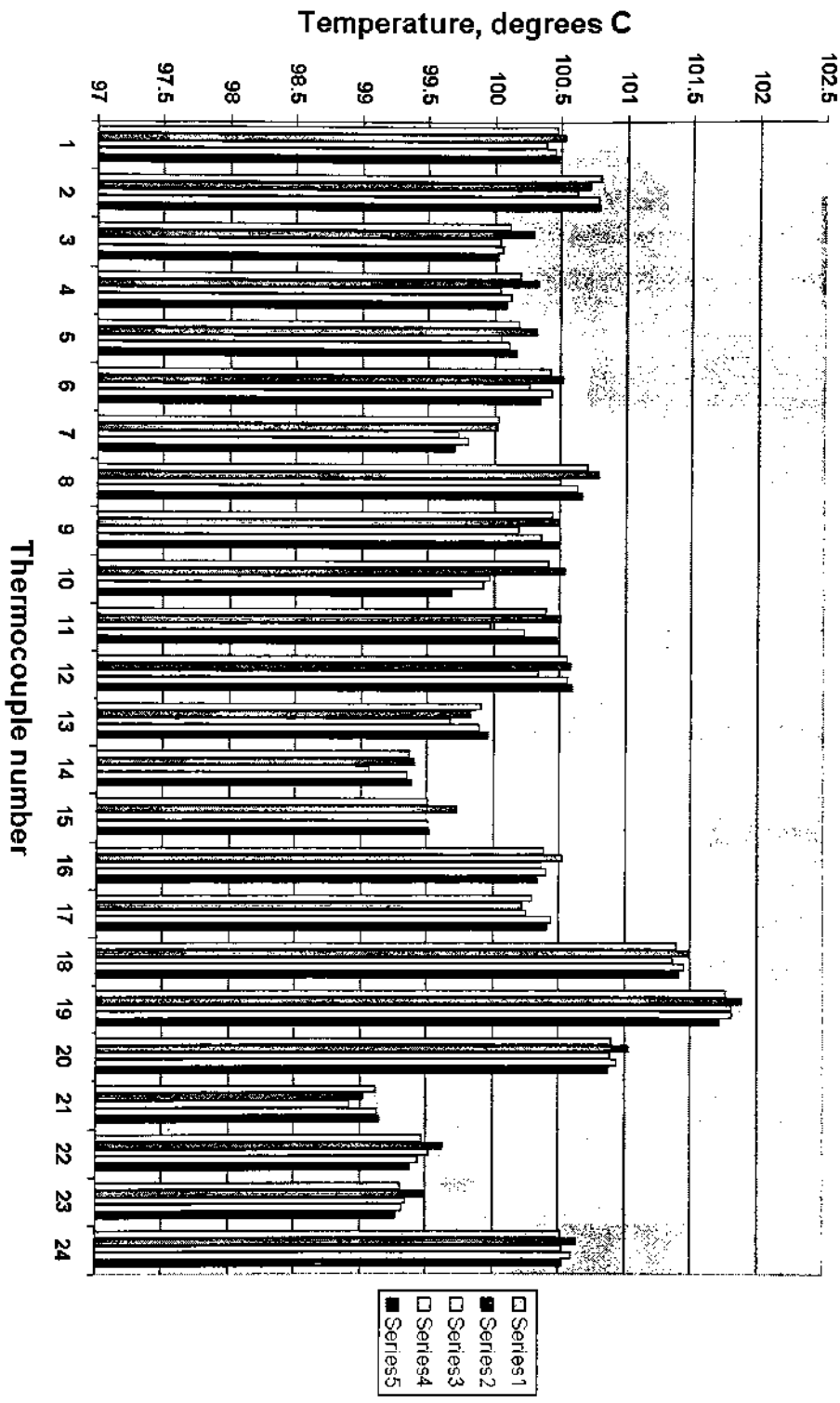

Figure 5a, calibration data for the saturation point of water, p_{atm}=1.0169 bar

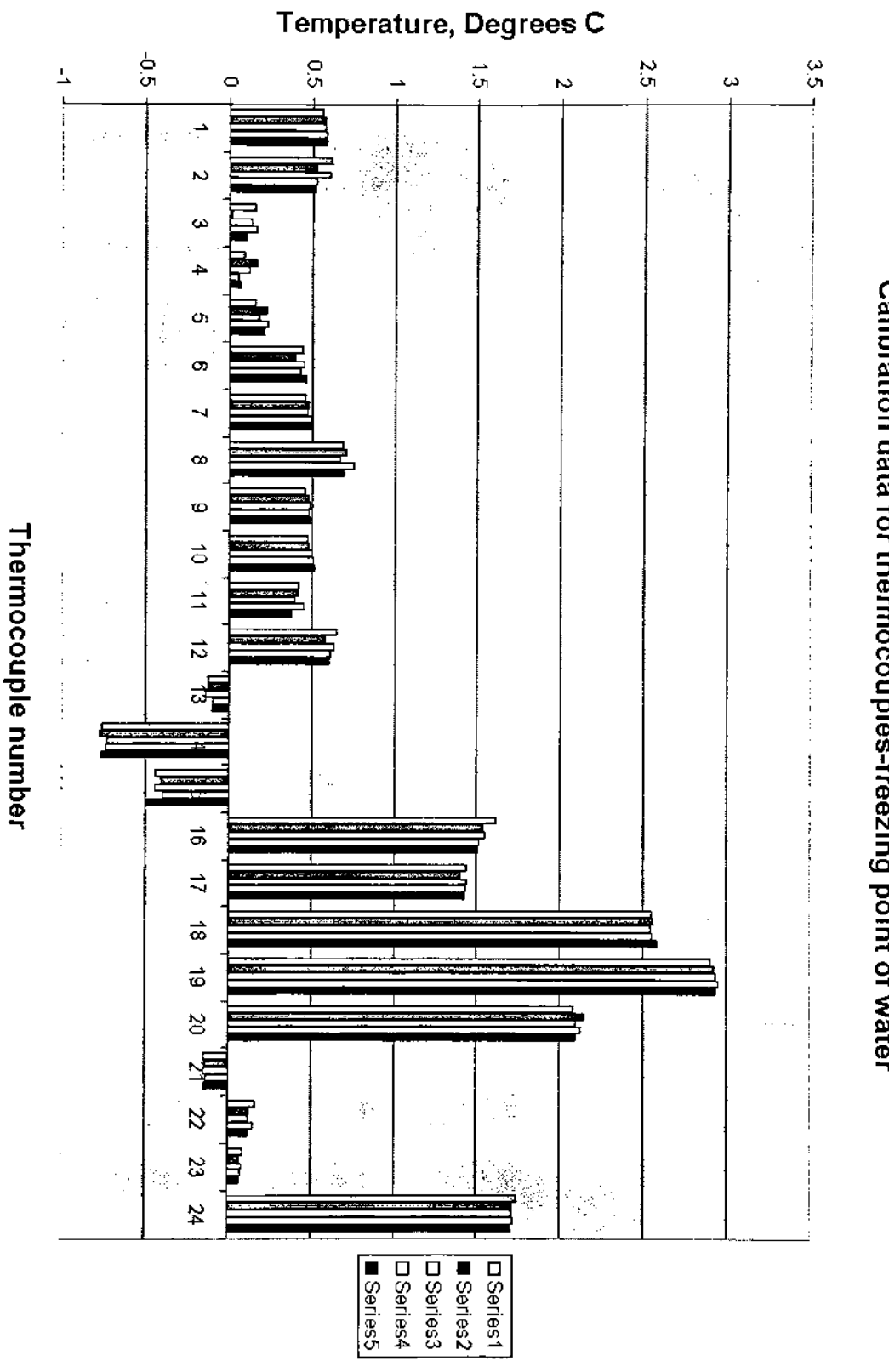

Figure 5b, calibration data for the freezing point of water

5.3.4 Discussion of calibration data

It can be seen from the plots that the majority of the data for each thermocouple's temperature during the 5 runs approaches a specific temperature within +/- 0.2 K.

It is then concluded that the thermocouples are accurate to an extent but very precise, the criterion being +/- 0.2 Kelvin. With the accuracy and precision of each thermocouple determined, an equation was derived to correct the temperature based on the read freezing point and saturation point temperatures.

Consider the following highly exaggerated case: Say at freezing, a certain thermocouple read 5 degrees C instead of zero°C. By the same token, say that the same thermocouple read 95 degrees at a saturation temperature of 100°C. Depending where the reading is taken in between these two points will dictate the amount to be added or subtracted from the read value to get to the corrected value. The figure in 5c below illustrates this point.

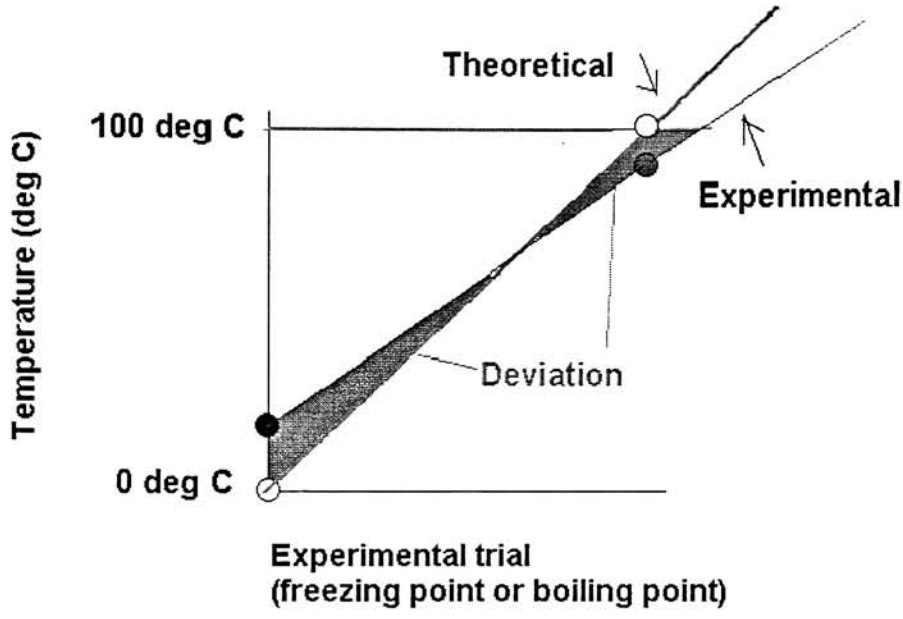

Figure 5c, Visual example for error correction in a linear relationship.

Equation 5.1 is based on the deviations between two intersecting lines and can be applied to precision thermocouples to bring measurement errors back to within the acceptable error criteria.

$$\text{corrected value} = \frac{(\text{acquired value - freezing point reading})}{\left(\frac{\text{boiling point reading - freezing point reading}}{\text{local saturation temperature - ice bath temperature}}\right)} \quad \textbf{(5.1)}$$

For any temperature reading taken as data, equation 5.1 can be applied to the data to correct it. The more accurate the probe, the closer the scale factor will be to unity.

6 Experimental procedure

6.1 Scope

This section outlines the standard that was followed each time an experimental run was performed. It is important that the standard be followed for each new run to ensure consistency in the data.

6.2 Preparation

Each time an experimental run is to be performed the following preparation and maintenance are done.

6.2.1 Degassing

The water circulation bath is filled with pure deionized water. Degassing of the water is accomplished by setting the bath temperature to 100°C, and the water is boiled in the bath for at least 1 hour. Advantage is also taken of the heaters of the test section by running some in-situ degassification to supplement the process in the bath.

6.2.2 Cleaning

Other pre-testing procedures followed include inspecting the water filter for cleanliness and running an 8mm doubled-up pipe cleaner saturated with 1.0 micron deagglomerated alpha alumna polishing compound through the test section bore to remove fouling deposits. Care is taken to make sure the test section and the flow loop is packed in insulation and all of the thermocouples are seated.

6.3 Procedure

6.3.1 Choosing values for the variables

All of the computer and data acquisition hardware is started up so that the Labview instrument panels can be launched and its readouts used to set up the initial conditions of the test. Any of the flow rate, heat rate or inlet temperature variables are set at this time and allowed to reach steady state.

6.3.2 Establishing steady state and the role of Labview

The formal criteria used to determine steady state was to acquire the same temperature within 0.1 K for at least 2 minutes. This was realized in practice through the use of scrolling real-time graphs on the Labview instrument panel. Several representative readouts were selected as indicators of the steady state condition such as the change in fluid temperature over the test section, wall temperature at axial locations and heat flux in axial planes. The time response of these variables could be dynamically monitored to the tenth of a Celsius degree using the scrolling graph on the front panel.

6.3.3 Executing file dialog

When the transients were finished, file dialog was executed from the same program by clicking on the "Start file I/O" button. The file is named and data is written to a tab-delimited text file which can be imported into Microsoft Excel. Clicking a "Stop file I/O" button terminates the data writing while the scanning continues.

6.3.4 Continuation of the experiment

One experimental parameter is then varied and the process is repeated.

7 Data reduction procedure

7.1 Scope

This section outlines the derivations and selection of the equations used in the present work. The data acquisition system provides access to raw temperature and flow data which must then be processed with the equations in this section to result in translated values of significance. These values can be correlated with other investigator's values and compared. The goal of data reduction is to combine the governing equations with the physical model resulting in a set of reduced equations that can be applied to the raw data.

7.2 Approach

The strategy used in the present work is to use three main equations to model the physics at coupled wall and the solid.

7.2.1 Conduction

Fourier's Law in cylindrical coordinates is used to model the heat flux within the solid as it reaches the channel wall.

7.2.2 Convection

Newton's Law of cooling is used to model the convective heat transfer from the channel wall to the fluid flow.

7.2.3 Temperature field

The Heat equation in cylindrical coordinates is used to derive the steady state temperature field within the solid.

7.3 Derivations

The heat equation is used to derive the temperature distribution within the solid based on the known location of thermocouple probes. It is the layout of these probes that are built into the boundary conditions and will result in equations for heat flux and surface temperatures as a function of those probe measurements, explicitly. This is how the data is related to the physical model and translated.

The appropriate form of the heat equation for a hollow cylinder in the radial direction and steady state conditions is:

$$\frac{1}{r}\frac{d}{dr}\left(kr\frac{dT}{dr}\right)=0 \qquad \textbf{(7.1)}$$

The general form of Fourier's law is

$$q''=-k\nabla T=-k\left(\frac{\partial T}{\partial r}\hat{e}_r+\frac{1}{r}\frac{\partial T}{\partial \theta}\hat{e}_\theta+\frac{\partial T}{\partial z}\hat{e}_z\right) \qquad \textbf{(7.2)}$$

With the assumption of conduction in only the radial direction, Fourier's Law reduces to

$$q''=-k\left(\frac{dT}{dr}\right) \qquad \textbf{(7.3)}$$

Turning our attention back to the heat equation, we will need to solve the integrated equation (equation 7.4) in terms of the radial locations of the thermocouples embedded in the solid. In general those locations will be referred to in this section as T_A and T_B. Schematically, this would be represented by the dots at radius 8.02 mm (0.3160 inches) and radius 10.32mm (0.4065 inches) shown in figure 7a.

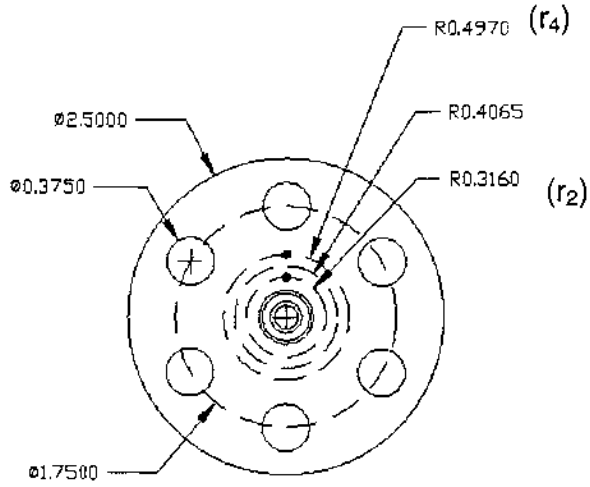

Figure 7a, Radial locations of thermocouples

The variable r_S will be referred to as the radius of the channel surface. We wish to solve equation 7.1 for the temperature distribution of the solid zone. Separating variables and integrating twice, a general solution is obtained.

$$T(r) = (C_1)\ln(r) + (C_2) \qquad \textbf{(7.4)}$$

Applying the boundary conditions

$$T(r_2) = T_2 \qquad \textbf{(7.5)}$$

$$T(r_4) = T_4 \qquad \textbf{(7.6)}$$

The solution can be expressed as

$$T_2 = C_1 \ln(r_2) + C_2 \qquad \textbf{(7.7)}$$

$$T_4 = C_1 \ln(r_4) + C_2 \qquad \textbf{(7.8)}$$

Solving for C_1 and C_2

$$C_2 = T_4 - C_1 \ln(r_4)$$

$$T_2 = C_1 \ln(r_2) + T_4 - C_1 \ln(r_4)$$

$$T_2 = C_1 \left(\ln \frac{r_2}{r_4} \right) + T_4$$

$$C_1 = \frac{T_2 - T_4}{\ln\left(\frac{r_2}{r_4}\right)}$$

$$C_2 = T_4 - \left[\frac{T_2 - T_4}{\ln\left(\frac{r_2}{r_4}\right)} \right] \ln(r_4)$$

Substituting C_1 and C_2 into the general solution

$$T(r) = \frac{T_2 - T_4}{\ln \frac{r_2}{r_4}} \ln(r) + T_4 - \frac{T_2 - T_4}{\ln \frac{r_2}{r_4}} \ln(r_4) \qquad \textbf{(7.9)}$$

$$T(r) = \frac{T_2 - T_4}{\ln \frac{r_2}{r_4}} \ln \frac{r}{r_4} + T_4 \qquad \textbf{(7.10)}$$

This gives the radial temperature distribution in terms of the two thermocouple locations. We wish to have a logarithmic based extrapolation for the temperature at the surface of the channel in terms of the two thermocouple locations. This just requires a value of r_s, the radius of the channel.

$$T_s = \frac{T_2 - T_4}{\ln \frac{r_2}{r_4}} \ln \frac{r_s}{r_4} + T_4 \qquad \textbf{(7.11)}$$

The above equation is specific to the z=2 station (the thermocouples that are located in a plane that is z=2 inches from the inlet plane in the axial direction) and a similar derivation can be made for the situation at z=1. Falling

back on our T_A and T_B notation the most general equation for the surface temperature extrapolation would take the form

$$T_s = \frac{T_A - T_B}{\ln \frac{r_A}{r_B}} \ln \frac{r_s}{r_B} + T_B \qquad \textbf{(7.12)}$$

Another form of the general equation that is needed in the derivation is the first derivative for the temperature distribution in the hollow cylinder.

$$T(r) = \frac{T_2 - T_4}{\ln \frac{r_2}{r_4}} \ln \frac{r}{r_4} + T_4$$

$$\frac{dT}{dr} = \frac{T_A - T_B}{\ln \frac{r_B}{r_A}} \left(\frac{1}{r} \right) \qquad \textbf{(7.13)}$$

The derivative is useful for substitution into the Fourier's law equation from equation 7.3.

$$q'' = -k \left(\frac{dT}{dr} \right)$$

$$q'' = -k \left(\frac{T_A - T_B}{\ln \frac{r_B}{r_A}} \left(\frac{1}{r} \right) \right) \qquad \textbf{(7.14)}$$

The heat flux at the channel wall can be found by replacing the r in equation 7.13 by the radius of the channel, r_s.

The goals of a steady state single phase analysis are to calculate the wall temperature, the heat flux and the local bulk fluid temperature. These variables can be substituted into the Newton's Law of Cooling equation to determine an experimental value for the heat transfer coefficient, h.

$$q'' = h(T_w - T_f) \qquad \textbf{(7.15)}$$

$$h = \frac{q''}{(T_w - T_f)} \qquad \textbf{(7.16)}$$

Since the fluid properties vary as a function of temperature, axially, it is important to extrapolate a local bulk mean temperature at each of the two stations where the heat transfer coefficient is measured. An energy balance at the wall of the tube would be of the form

heat conducted to the tube wall = heat convected away from the tube wall **(7.17)**

$$q'' \pi DL = \dot{m} c_p (T_{f,x} - T_{f,i}) \qquad \textbf{(7.18)}$$

Where $T_{f,x}$ is the local bulk mean temperature at the axial length L to be solved for. $T_{f,i}$ is the inlet temperature. Note that equation 7.17 is valid only for single phase heat transfer.

$$T_{f,x} = \frac{q'' \pi DL}{\dot{m} cp} + T_{f,i} \qquad \textbf{(7.19)}$$

It would seem that an iterative procedure would be necessary to calculate $T_{f,x}$ because of the dependence of fluid temperature on the specific

heat, c_p. If the heated tube is considered to be constant surface heat flux, the change of the mean fluid temperature is linear with respect to axial direction. Knowing the total change in fluid temperature, an approximate value for the local fluid temperature can be calculated based on the fraction of axial length used to heat the fluid. This can be expressed as

$$T_{est,z=1} = \Delta T_{fl,total}\left(\frac{1}{3}\right) + T_{inlet} \quad \textbf{(7.20)}$$

$$T_{est,z=2} = \Delta T_{fl,total}\left(\frac{2}{3}\right) + T_{inlet} \quad \textbf{(7.21)}$$

The fluid property c_p can be calculated based on this temperature.

7.4 Conduction effects from fittings and tubing

One issue that needs to be addressed is the validity of the length L in Equation 7.15. Depending on the mass flow rate, degree of subcooling and the heat flux, the point at which the fluid begins to be heated can start upstream of the test section due to thermal conduction out through the compression fittings. The worst case would be a combination of a highly subcooled inlet temperature, high temperature in the solid, and low mass flow rate. Fluent5 CFD analyses, discussed in section 8, were used to assess the conduction effects with different boundary conditions

7.5 Approximations for physical properties

Steps were taken to improve the robustness of the data processing procedure by automating it. Basically, this involved creating polynomial

approximations to fluid properties as a function of temperature which can be embedded in the spreadsheet equations.

μ, Ns/m^2	=(2.1475E-16*(T^6))+(-1.7243E-13*(T^5))+(5.575E-11*(T^4)) +(-9.3962E-9*(T^3))+(9.0276e-11*(T^2))+(-5.1572E-5*(T))+(1.7408E-3)
c_p, J/kgK	=(3.1739E-11*(T^6))+(-5.8018E-8*(T^5))+(1.6452E-5*(T^4)) +(-1.918E-3*(T^3))+(0.11679*(T^2))+(-3.4636*T)+(4216.9)
Pr	=(2.5571E-7)*(T^4)+(-7.0901E-5*(T^3))+(7.E-36857*(T^2)) +(- 0.4265873*(T))+12.94111
k, fl (W/mK)	=(-7.3318E-6*(T^2))+(1.8418E-3*(T))+0.56947
k, solid (W/mK)	=(-2.71E-7)*T^3 - (2.03E-4)T^2 + (0.213)T+ (111.4)

Table 7.1

All of the trends to these approximations fit the accepted data with a sum-squared-error of no less than 0.9998 R^2.

The reference values used to compare the experimental values against were broken down based on the fluid flow regime present. For fully developed turbulent flow, the Gnielinski (1976) correlation was used to predict a Nusselt number. Its validity has been established for 0.5 ≤Pr ≤ 2000 and 2300 ≤Re ≤ 10^4.

$$Nu_D = \frac{\left(f/8\right)\left(\mathrm{Re}_D - 1000\right)\mathrm{Pr}}{1 + 12.7\left(f/8\right)^{1/2}\left(\mathrm{Pr}^{2/3} - 1\right)} \qquad \textbf{(7.22)}$$

The friction factor f, is given by the equation [Gnielinski (1976)]

$$f = [1.58\ln(\mathrm{Re}) - 3.28]^{-2} \qquad \textbf{(7.23)}$$

Or the relative roughness can be used in obtain a friction factor from the Moody diagram (Moody 1944).

For fully developed laminar flow, the entry region problem must be addressed, again with the assumption of a constant heat flux wall. Figure 7b is a chart that relates the inverse Graetz number to the Nusselt number.

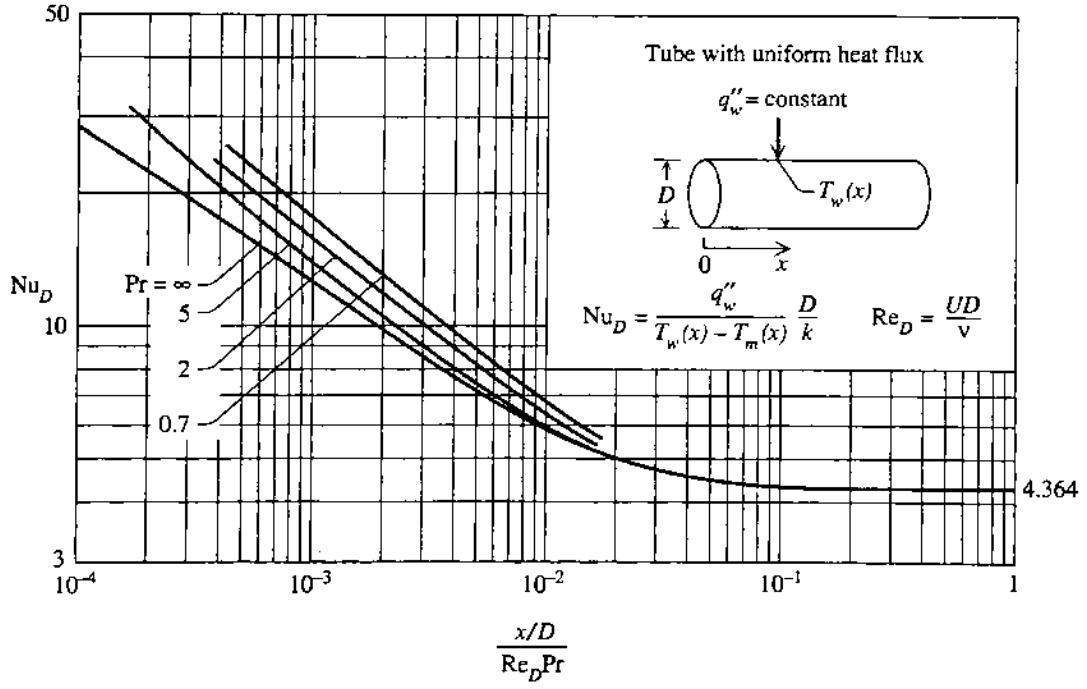

Figure 7b, Thermal entry length considerations using the Graetz number

7.6 Dimensionless Parameters

Reynolds Number $\mathrm{Re} = \frac{4\dot{m}}{\pi D \mu}$ **(7.24)**

Reynolds number (Re) is a ratio of the inertia forces to the viscous forces. Its magnitude can be used to characterize the type of flow regime, be it laminar or turbulent. $\dot{m}$, here is the mass flow rate, D is the internal hydraulic diameter and μ is the dynamic viscosity

Boiling Number: $Bo = \frac{q''}{G * h_{fg}}$ **(7.25)**

The boiling number (Bo) is a ratio of fluid vaporized to that of the incoming flow. Its use is popular in boiling heat transfer correlations. q'' is the heat flux, G is the mass flux and h_{fg} is the heat of vaporization.

Nusselt Number $Nu = \frac{hL}{k_f}$ **(7.26)**

The Nusselt number (Nu) can be conceptualized as the ratio of the convection for the fluid in motion to the conduction for the motionless fluid layer or, it can also be given as the dimensionless temperature gradient at the surface. h is the heat transfer coefficient, L is the characteristic length and k_f is the thermal conductivity of the fluid.

Prandtl Number $\mathrm{Pr} = \frac{c_p \mu}{k} = \frac{\upsilon}{\alpha}$ **(7.27)**

The Prandtl number (Pr) is a dimensionless parameter which characterizes the relative effectiveness of momentum and energy transfer by molecular diffusion within the boundary layer. c_p is the specific heat of the fluid, μ is the dynamic viscosity and k is the thermal conductivity of the fluid. The number can also be expressed in terms of the kinematic viscosity, ν and the thermal diffusivity, α, ($\alpha = k/\rho c_p$).

Graetz Number $Gr = \left(\frac{x/D}{\mathrm{Re}\,\mathrm{Pr}} \right)^{-1}$ **(7.28)**

This number is used in the solution of thermal hydraulic problems where the flow is not fully developed thermally. It is most often used in its inverse form in charts. x is the characteristic length, D is the diameter and RePr is the product of the Reynolds and Prandtl numbers, described above.

8 CFD simulations

8.1 Scope

This section outlines the steps taken to create a computational model of the experiment using commercially available CFD software. Modeling the test section virtually is a valuable tool for visualizing the distribution of the temperature field within the solid as well as modeling the convective heat rate. The test section in the present work was designed to heat the solid with a peripheral array of cartridge heaters. There is expected to be a non-uniform temperature field around the location of the heaters. The temperature field is also expected to converge to a uniform gradient since heat removal is facilitated through the central channel. The entire experiment is based on equations and measurements that assume a uniform temperature field within the solid. A computational model of the experiment is undertaken to verify that these assumptions are correct.

8.2 Approach

The approach taken in this section is to use Computational Fluid Dynamics software (CFD) from Fluent Inc, version 5. The steps followed in using CFD to create a model are outlined below.

8.2.1 Preprocessing

Preprocessing involves defining the geometrical shape of a problem, discretizing the domain of the problem with a mesh and identifying the locations where boundary conditions are to be specified.

8.2.2 Solving

The procedure for solving involves selection of the proper algorithms to go along with the physics of the problem, assigning numerical values for boundary conditions and solving the problem with finite difference equations.

8.2.3 Postprocessing

After solution data is obtained the results are viewed by superimposing them on the domain of the problem.

8.3 Preprocessing

8.3.1 Geometry definition

Definition of the problem as an exact replica of the test is accomplished using Gambit version 1, also from Fluent, Inc. Gambit utilizes an approach called "top down" geometry creation where 3-dimensional primitive shapes are drawn and interfaced with other shapes through Boolean operations and splits. Shapes were created, positioned, interfered and processed with Boolean algebra resulting in the form that is shown in figure 8a.

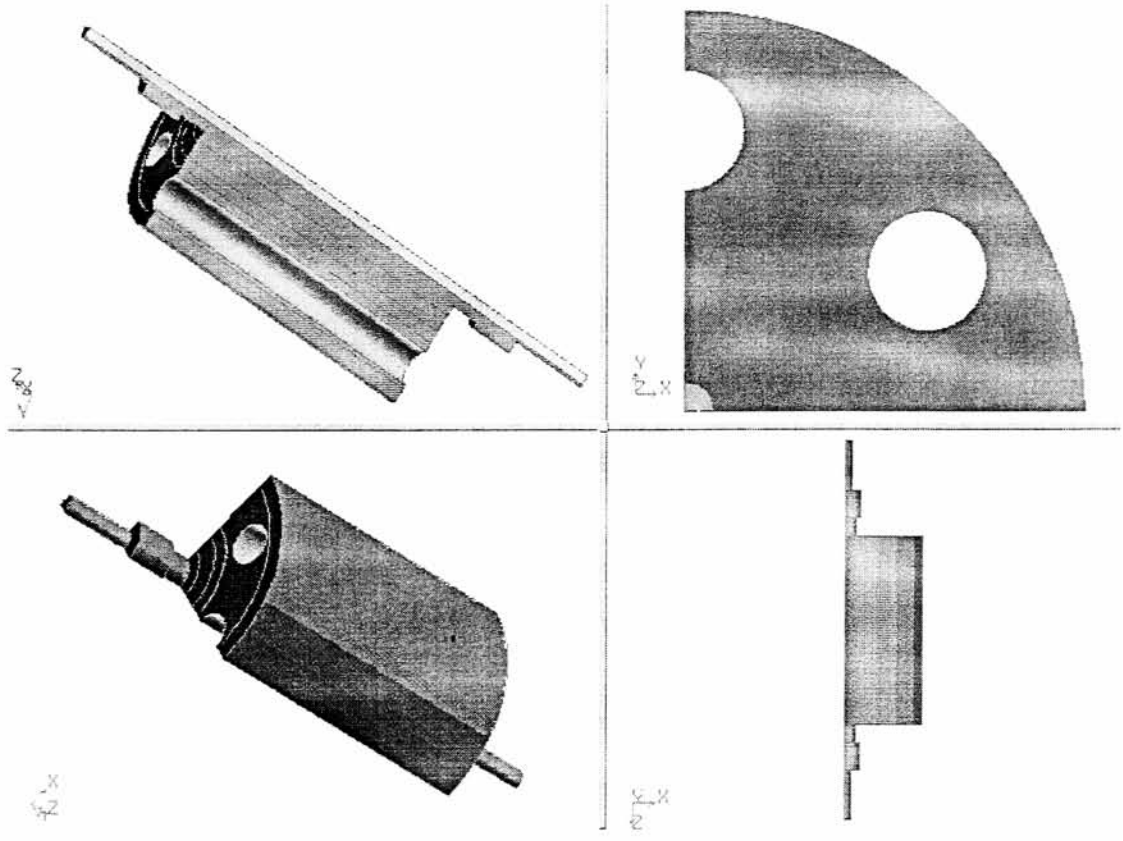

Figure 8a, Sectional views from a rendered solid in Gambit

It is not an efficient use of computer resources to model the entire problem in 3-D, each cell that is added takes extra time to solve over. Only a quarter of the test section was used, taking advantage of the symmetry that exists. The problem cannot be considered fully axisymmetric because of the periodic boundary conditions occurring at the heaters.

8.3.2 Mesh generation, solid

After completing the geometrical details, the next step was to create a mesh. Mesh generation in Gambit can is fully automated, but more control was exercised to refine specific parts of the mesh. Resolution of specific details and the accuracy of the solution require strategic placement of fine

grid elements, whereas areas that are not expected to have large gradients can be discretized with large grid elements. This concept is applied to the resolution of the fluid boundary layer on the channel wall and can be seen in figures 8b and 8c.

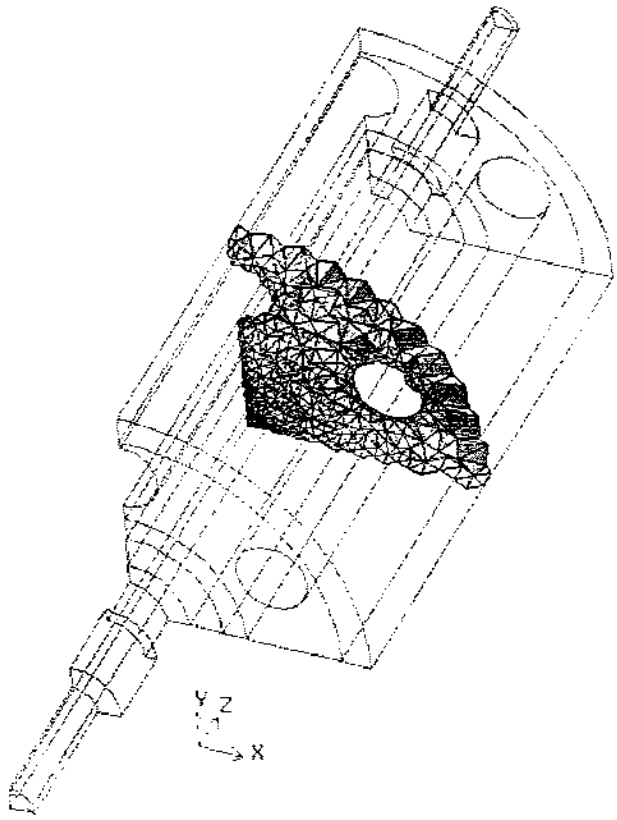

Figure 8b, A mesh quality examination in Gambit showing grid elements with respect to the entire wireframe

All of the grid elements in the solid are tetrahedra. Within the solid, mesh sizes used range from 0.1 inches at the outside wall, 0.05 inches at the heaters, grading all the way down to 0.02 inches at the channel wall. Refer to figures 8b and 8c for a representation of this technique.

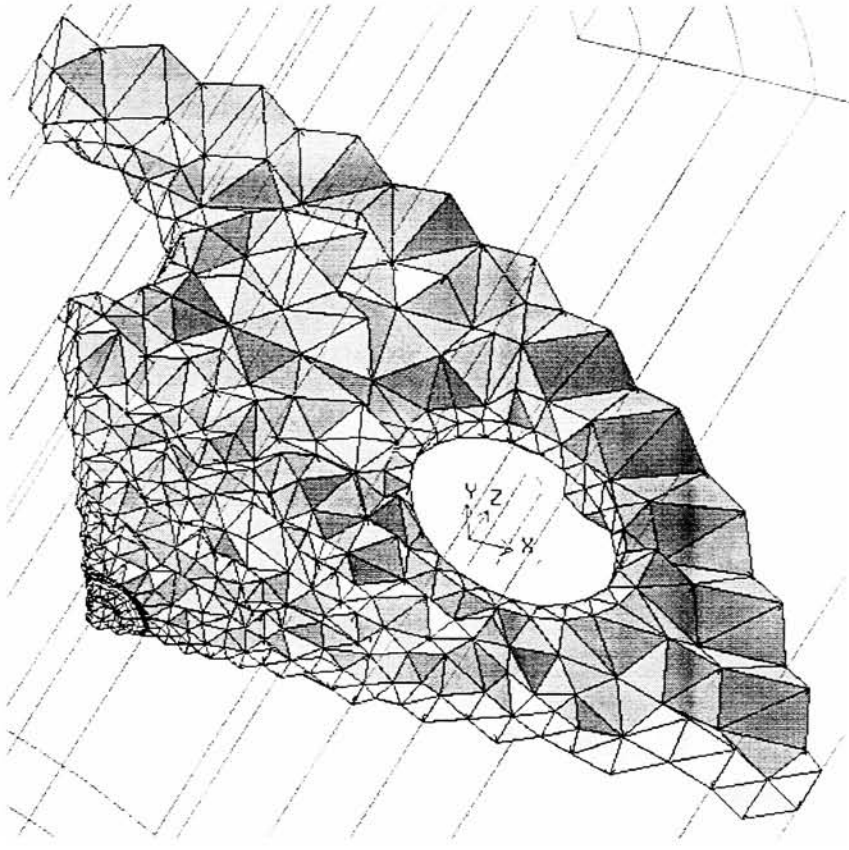

Figure 8c, A close up of the mesh shown above. At the vertex is the fluid channel.

8.3.3 Mesh generation, fluid

The resolution of the boundary layer becomes very important to the accuracy of the solution because of the need to account for viscous effects and development of the fluid temperature. A split operation was performed between two intersecting volumes which created the interface between the solid and the fluid. This created two discrete volumes that share a common wall. In Fluent, this is called a coupled wall and all fluxes are conserved across it. In the fluid zone, a hexehedral mesh scheme devised especially for resolving boundary layers was invoked. This extremely fine, graded mesh

started with a mesh size of 0.002 inches at the wall and grew by a factor of 1.475 toward the center of the channel for each of 4 rows. The remainder of the fluid zone grid was meshed with tetrahedral and pentagonal elements of 0.015 inch size. An image of the meshed fluid zone is shown in figure 8d. The mesh totaled 146636 cells and 46191 nodes for the entire problem.

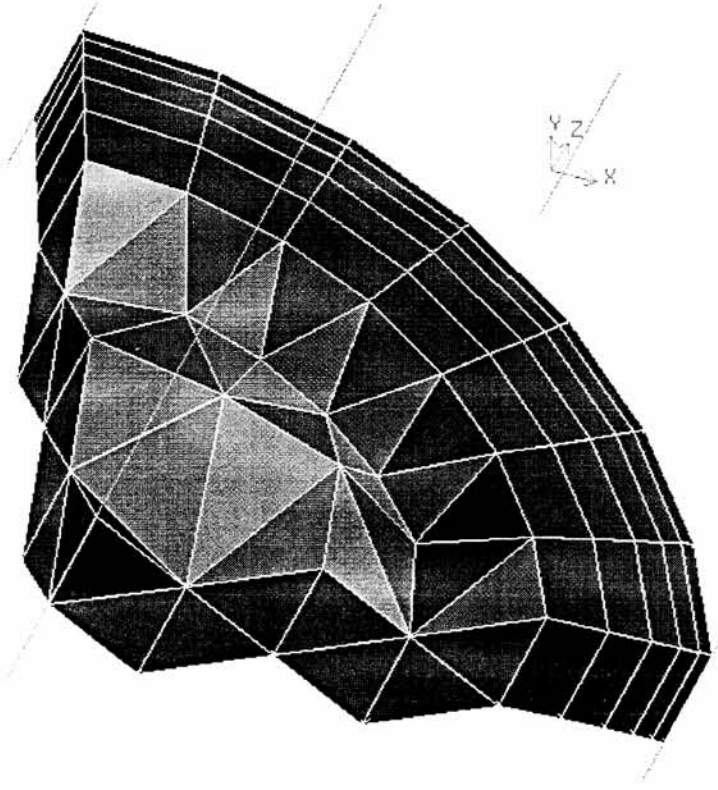

Figure 8d, An extremely enlarged view of the hybrid mesh scheme used in the fluid channel.

8.3.4 Specification of boundary zones

The last step in preprocessing involved specifying the general boundary types and zones. The solid and fluid zones were each flagged so that the solver could differentiate them. Other areas such as inlets, outlets,

walls and symmetry planes were also flagged so that specific boundary conditions could be applied. The last step was to export a file containing the geometry, mesh and boundary types to a file that can be read into the solver.

8.4 Fluent procedure and solving

The software is installed in the Mechanical design lab, Building 17 of Rochester Institute of Technology on 200Mhz Pentium Pro PC computers running with 128 MB of RAM.

8.4.1 File import and preparation

After the case has been successfully created in the preprocessor, it can be saved and directly imported for processing.

The first step is associated with verifying the validity of the grid. The **grid** →**check** command provides volume statistics that can be used to verify that no non-real type grid elements were created in the meshing process. The geometry in this case was intended to have units of inches, so the grid is scaled to match the expected domain extents.

Smoothing and swapping are tools that are used to increase the quality of the final numerical mesh. Smoothing repositions the nodes and face swapping modifies the cell connectivity to achieve these improvements in quality. The grid was smoothed with the **skewness** method to refine the tetrahedral grid elements. The target cells are those whose geometry least resembles an isolateral tetrahedron.

8.4.2 Selection of algorithms

The next steps in creating the case are to define the functions that represent the proper physics. The default **segregated solver** was used in 3D space with implicit formulation. The model is based on steady state conditions, so a steady time formulation is chosen. By virtue of the heat transfer physics present, the **Energy** model must be enabled. For the situations where Re>2300, the κ-ε viscous model can be invoked to model turbulence. The standard κ-ε model is a semi-empirical model based on model transport equations for the turbulent kinetic energy (κ) and its dissipation rate (ε). In the use of the κ-ε model, it is assumed that the flow is fully turbulent, and the effects of molecular viscosity are negligible.

8.4.3 Assignment of values to boundary conditions

In the **define** → **materials** panel, the constants for density, specific heat and thermal conductivity are specified. Since this is a coupled problem, there must be constants for the solid as well as the fluid. The properties of the brass and the water are specified in this step.

The values specific to each boundary condition corresponding to the boundary types created in Gambit are set in **define**→ **boundary conditions**. The walls defining the outer boundaries of the test section are given a heat flux boundary condition of q"=0, making them adiabatic walls effectively. This corresponds to the actual insulated experimental conditions. The wall corresponding to the heater bores are given a heat flux assignment based on the total power supplied by the power supply divided by the total surface area.

At the mass flow inlet panel, a mass flux is specified as well as the total fluid temperature at the inlet. Also designated is the flow velocity vector, which was 0i,0j,1k here. The **intensity and hydraulic diameter** turbulence model was chosen as the turbulence specification method in this case, with an intensity of 10% and a hydraulic diameter of 0.1875 inches. The mass flux and the heat flux at the heater bores are the most significant boundary conditions here, having been set, the solving of the case can commence.

8.4.4 Initialization and execution of the solver

The residual monitor is enabled so that divergence can be detected during the solution process. Initially, the relaxation factors for the flow, energy and turbulence equations are left as default. The default discretization schemes were left as default to begin with, which includes first order momentum, energy, turbulent kinetic energy and turbulence dissipation rate. The last step before solving is to initialize the computational domain with a temperature corresponding to the heater temperature. The solution process is initiated by setting the number of iterations and triggering the solver.

After it is observed that the solution is processing in a generally convergent manner, as indicated by the residual monitor, usually after about 100 iterations, the discretization for momentum, energy, turbulent kinetic energy and turbulence dissipation rate are changed to second order for increased accuracy. The solution generally speeds up in iteration time after the first 50 iterations, reaching rates of up to 6 iterations per minute. Typical trends for the residuals are shown in figure 8e.

8.5 Postprocessing

A certain amount of post processing was required to extract the solution from the computer in graphical form.

8.6 Results of CFD simulations, laminar and turbulent Reynolds numbers

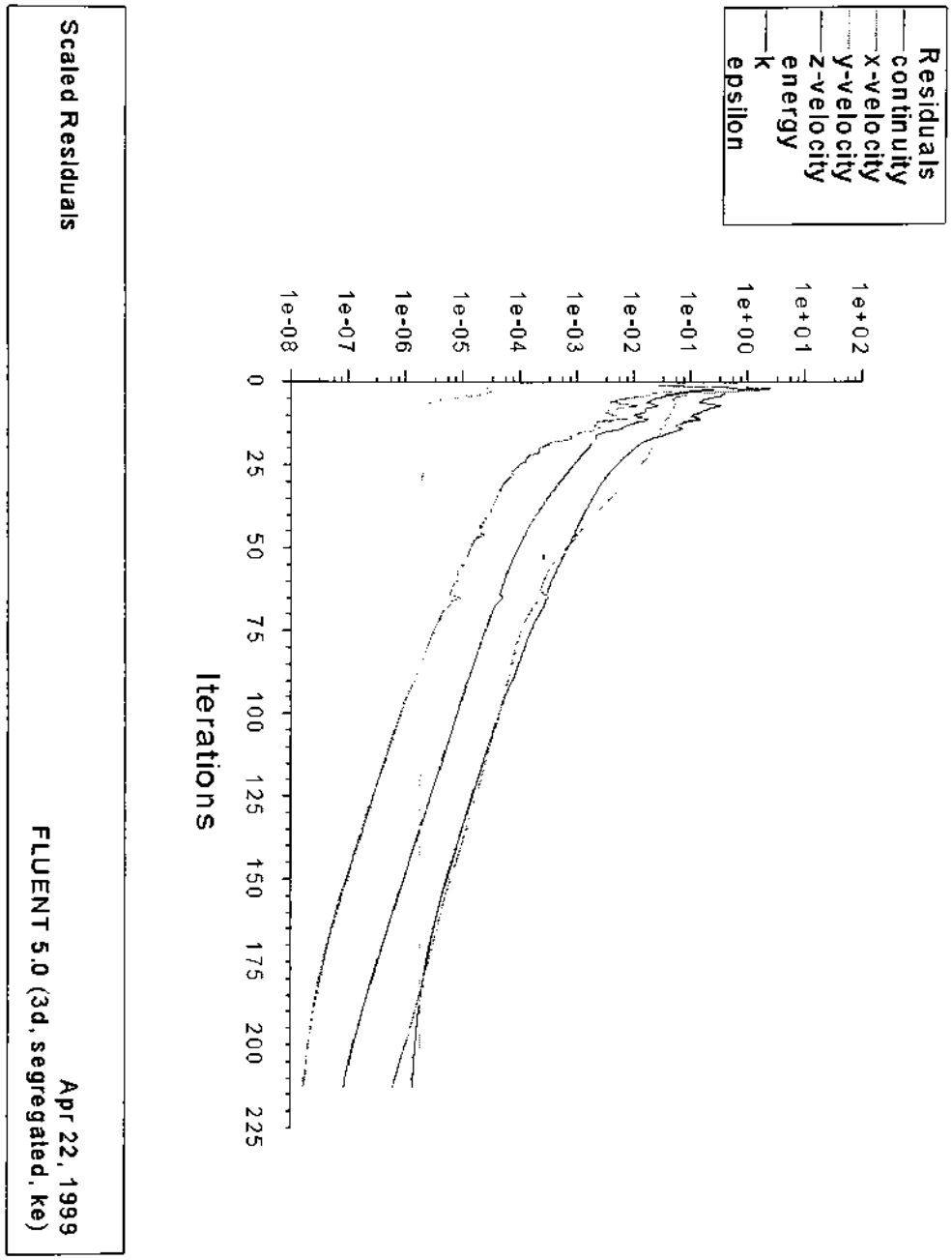

Figure 8e, Residual plot for a turbulent flow simulation. Residuals indicate the sum of the errors and their trend can be used as an indicator of convergence.

8.6.1 Results of CFD simulations, laminar flow case (Re_D<2300)

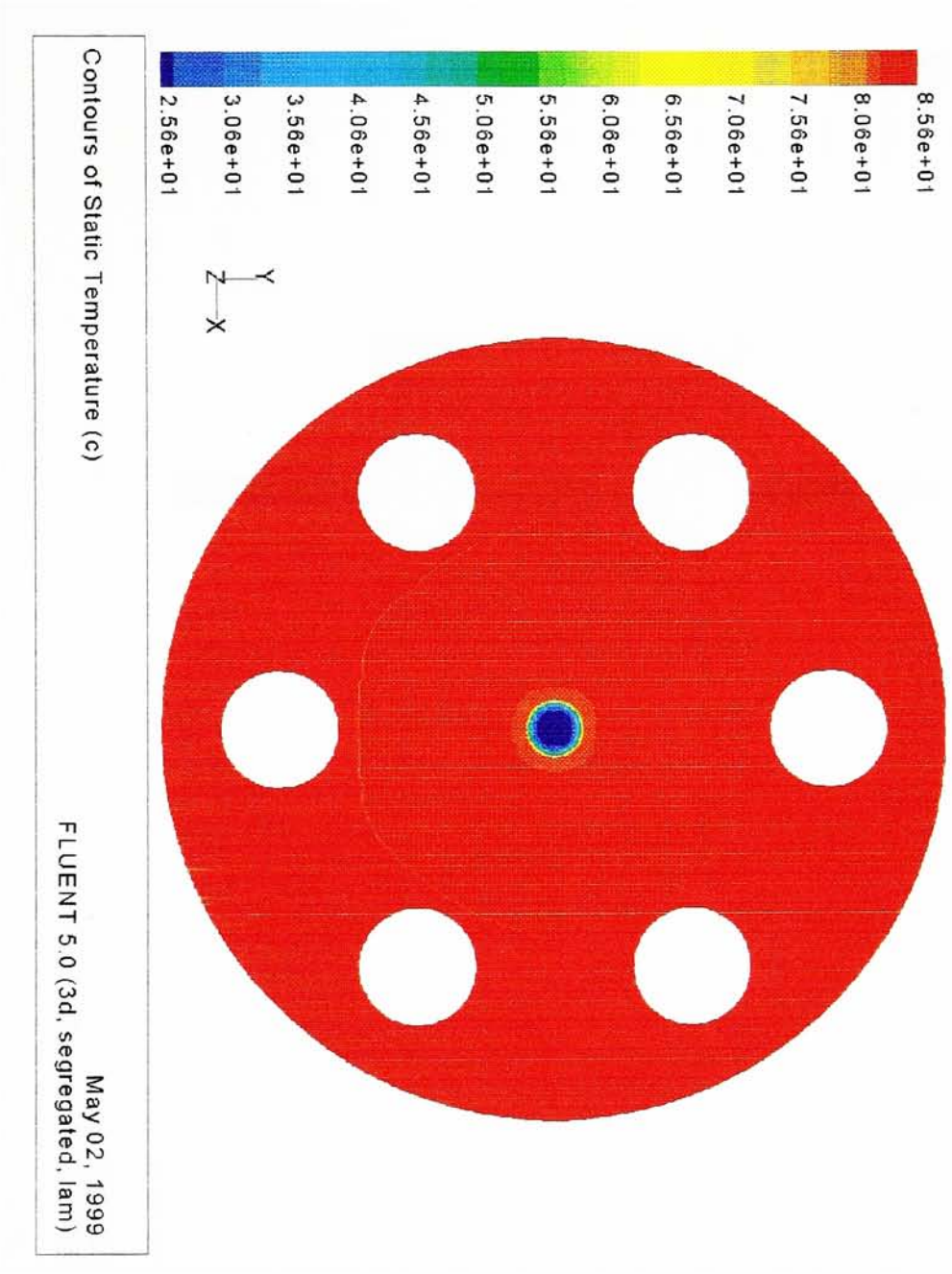

Figure 8f, A contour plot of temperature at a cross section for a laminar flow simulation. At the center is the fluid channel

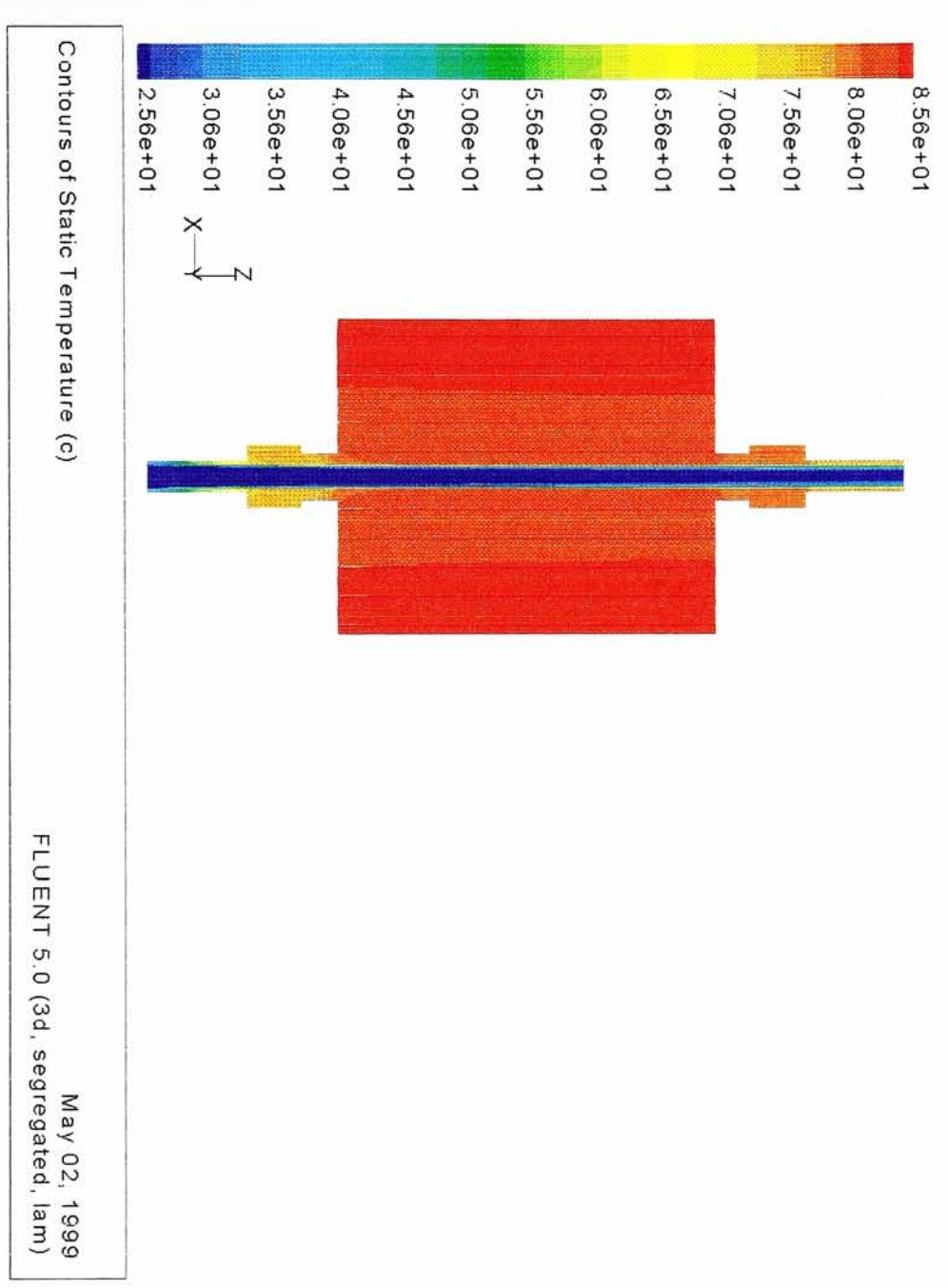

Figure 8g, contours of temperature in a longitudinal cross sectional plane for a laminar flow simulation

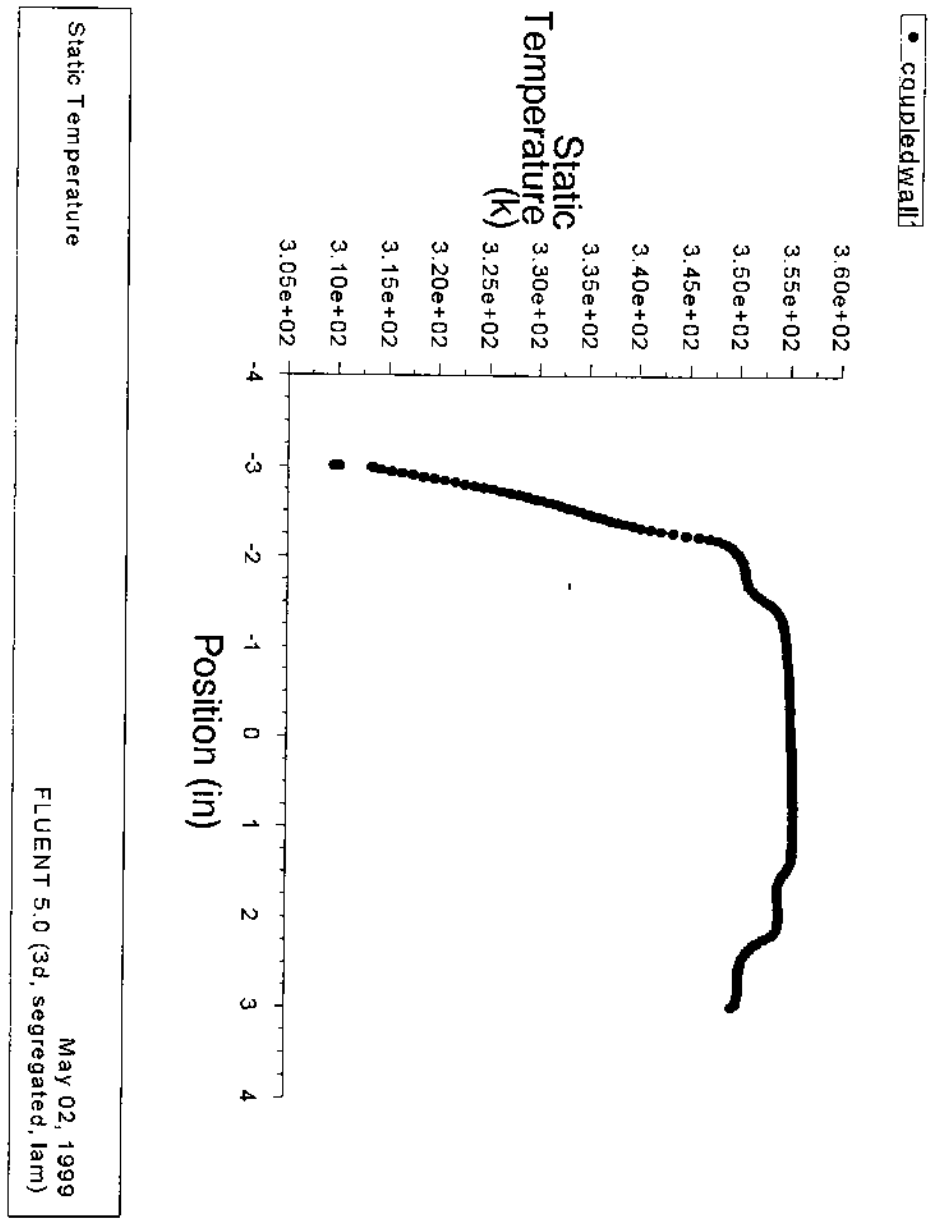

Figure 8h, X-Y plot of the temperature of the channel wall along the axial direction for laminar flow. Flow direction is from (-) to (+) and the axial center is at z=0. Note the temperatures in the fittings at z=-1.8 and z=1.8 inches.

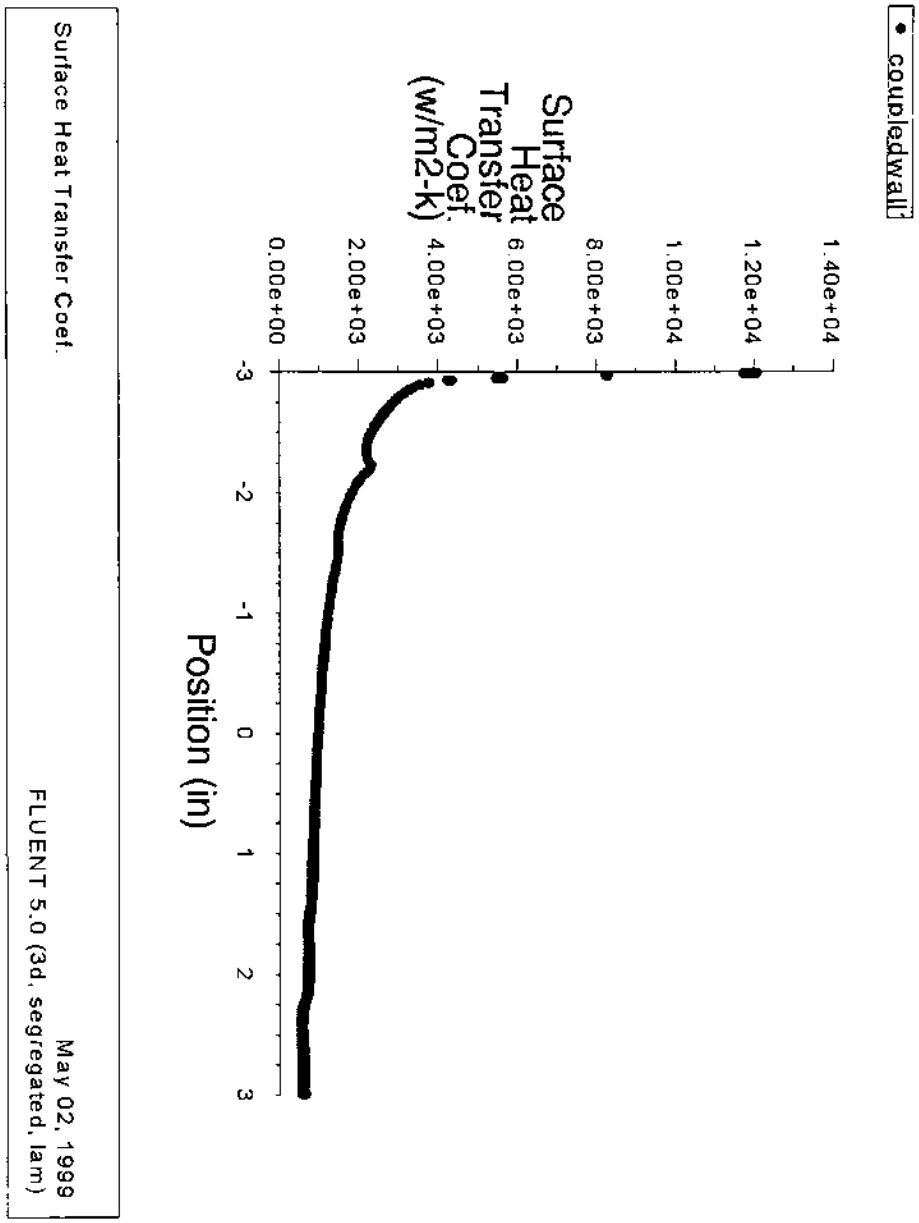

Figure 8i, X-Y plot of the heat transfer coefficient on the channel wall along the axial direction for laminar flow. Flow direction is from (-) to (+) and the axial center is at z=0.

8.5.2 Results of CFD simulations, turbulent flow case (Re_D>2300)

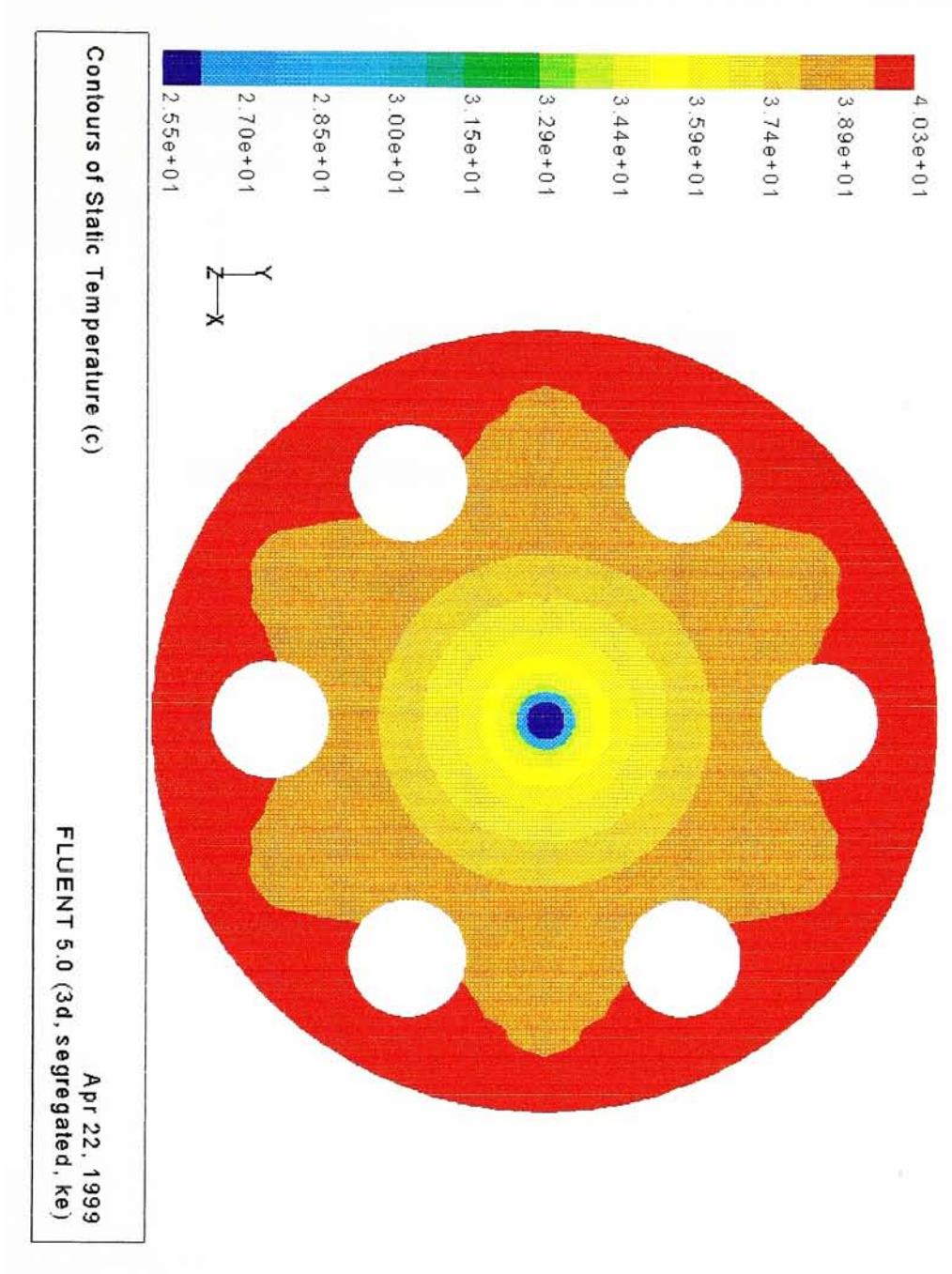

Figure 8j, A contour plot of temperature at a cross section for a turbulent flow simulation. At the center is the fluid channel

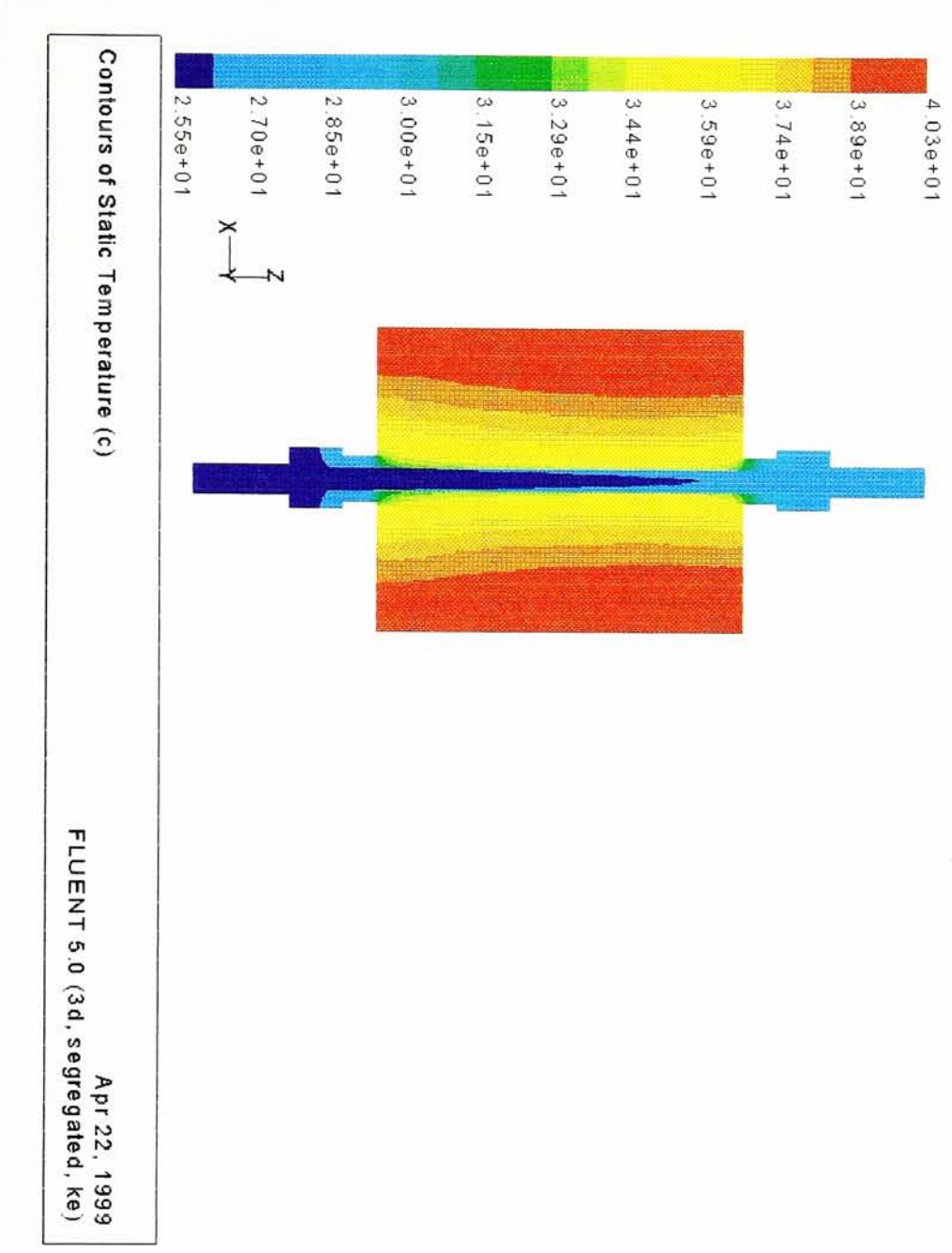

Figure 8k, contours of temperature in a longitudinal cross sectional plane for a turbulent flow simulation

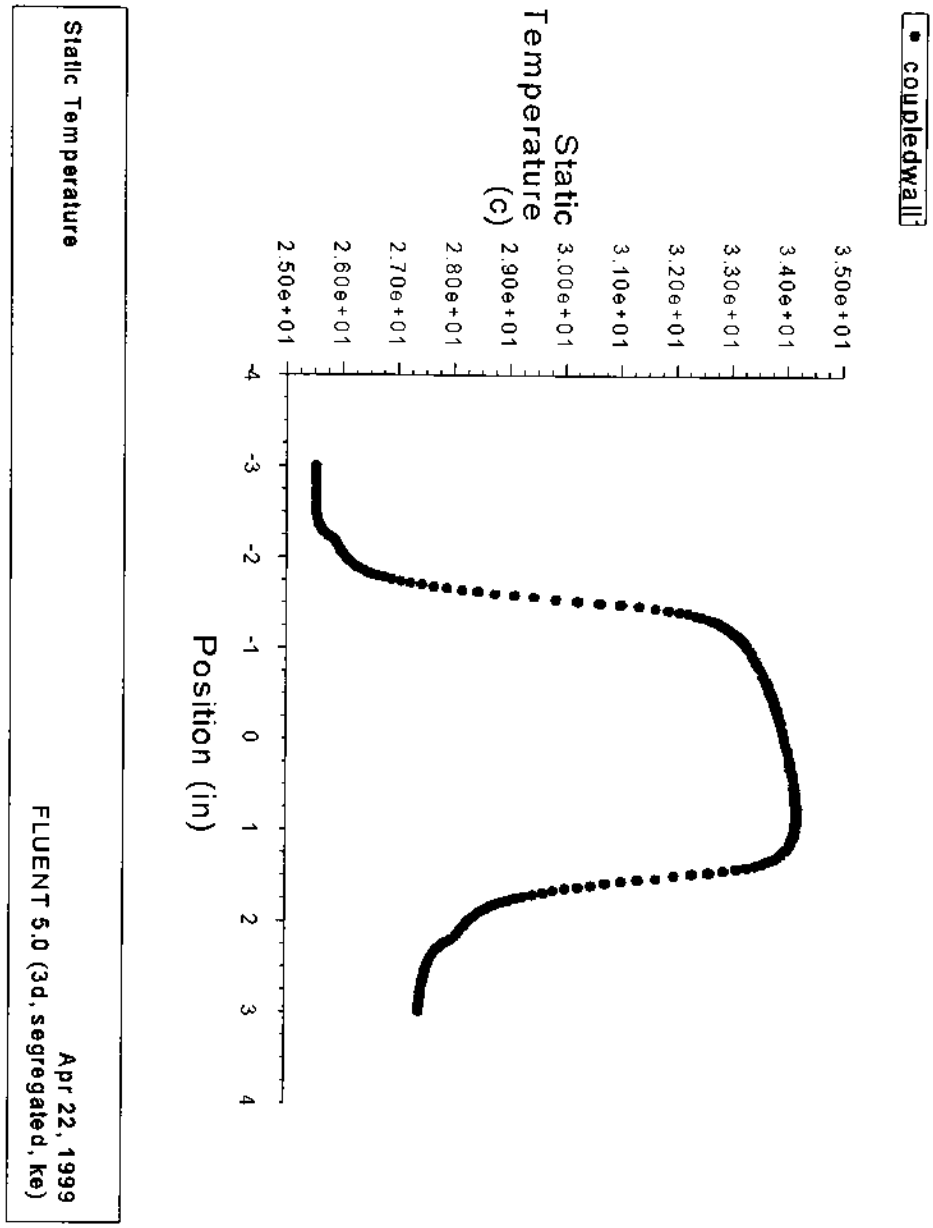

Figure 8l, X-Y plot of the temperature of the channel wall along the axial direction for turbulent flow. Flow direction is from (-) to (+) and the axial center is at z=0. Note how the thermal mass effects of the fittings are less significant in this case due to the increase in the heat transfer effectiveness in the test section.

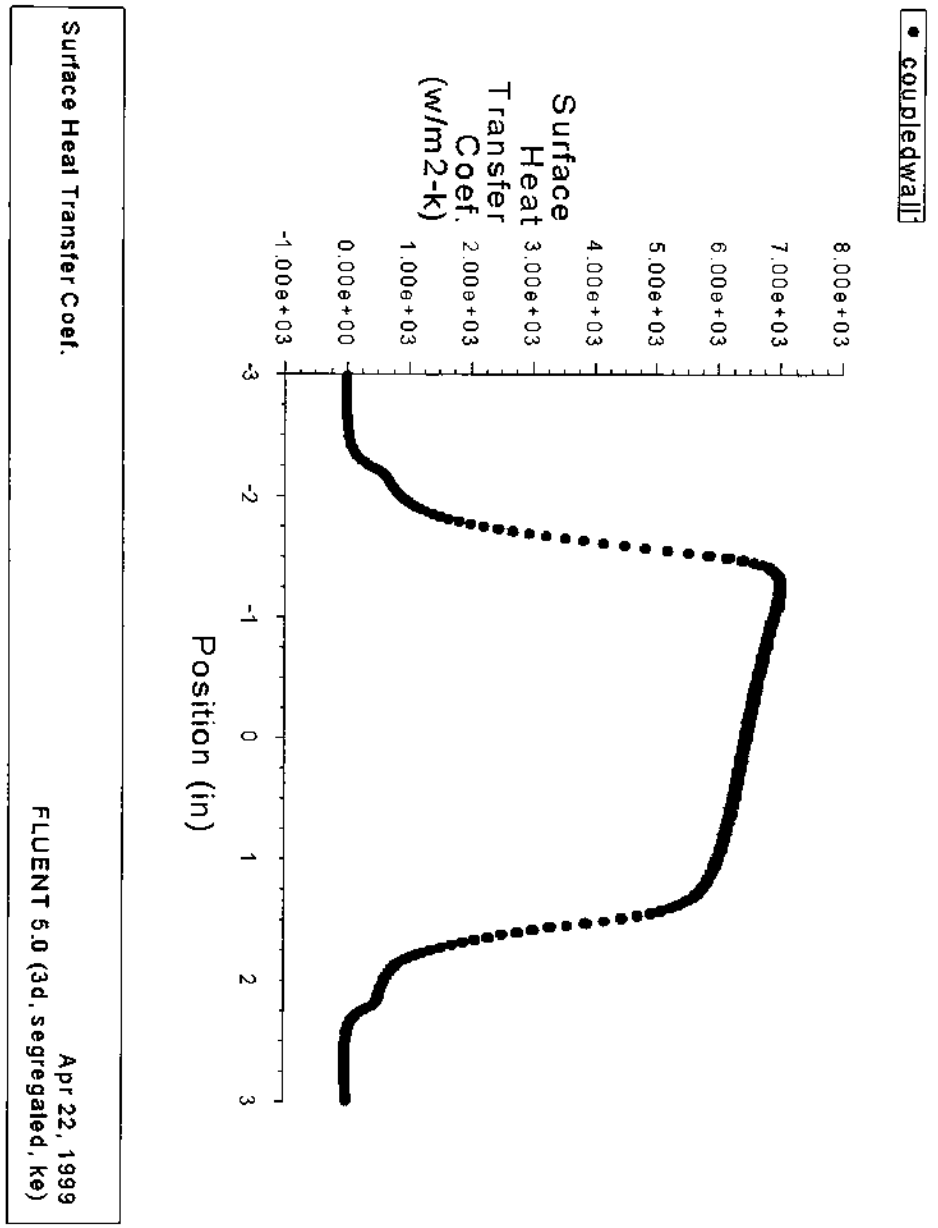

Figure 8m, X-Y plot of the heat transfer coefficient on the channel wall along the axial direction for turbulent flow. Flow direction is from (-) to (+) and the axial center is at z=0.

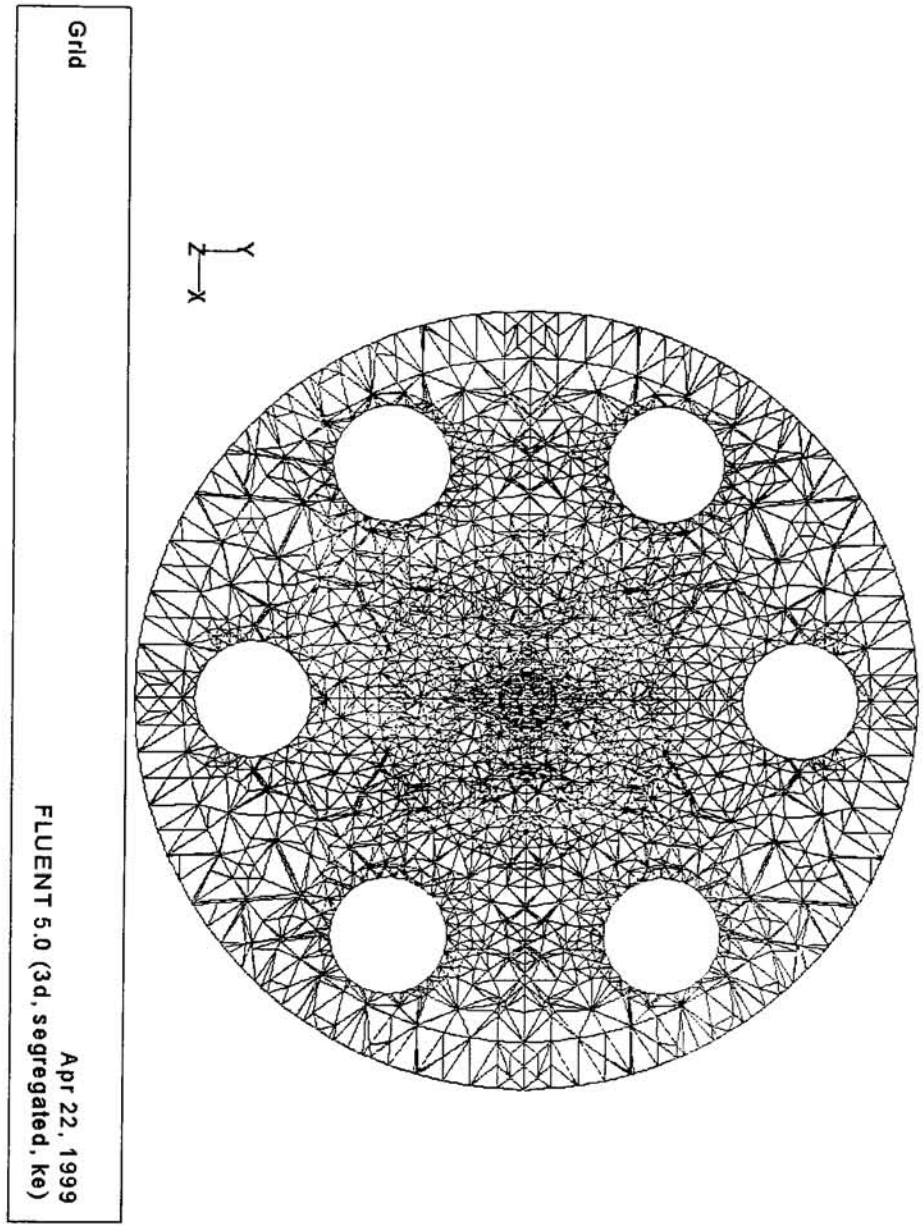

Figure 8n, an image of the grid in a cross section showing the mesh grading scheme.

8.7 Discussion of CFD results

8.7.1 Layout of this section

The discussion will be given in two parts for this section. First, each figure between 8e and 8n will be discussed briefly by pointing out features significant to the case simulated. Second, a comparison of the model's performance will be given.

8.7.2 Figure 8e, scaled residuals

The plot describes the sum of the errors as the solution progresses. The trend provides information on the convergence of the solution. A residual line with a negative slop indicates convergence (the solver is converging on a particular solution) and a positive slope indicates that the solver is experiencing divergence (the solver cannot determine a direction to continue iterating in).

The residuals shown indicate the solution was well behaved and its low residuals at the finish provide a guarantee in the accuracy of the solution.

8.7.3 Figure 8f, contours of static temperature

This graphic is of a cross section in the solid at an axial midpoint. The solution is superimposed over that part of the domain with filled isotherms. The important points that can be taken from this plot are

(1) Uniform temperature field in the locations where thermocouples would be embedded in the solid.

(2) Large temperature gradient near the channel wall

8.7.4 Figure 8g, contours of static temperature

This graphic represents temperature contours in a longitudinal cross section. Flow is from the bottom of the page to the top. There are some very interesting features that provide insight into the conduction heat transfer and fluid temperature distribution in this case.

(1) There is a small temperature gradient through most of the solid followed by a sharp rise near the channel.

(2) The magnitude of the conduction effects from the solid out through the fittings becomes evident at the inlet and the outlet. Because of the degree of liquid subcooling, the inlet fitting experiences more cooling than the outlet fitting.

(3) The organization of the flow is also evident through the variation of the temperature distribution in the axial direction. The flow appears to be extremely stratified all along the test section and a thermal boundary layer develops. The stratification inhibits the heat transfer from the wall to the fluid, creating a blanket of fluid that heat must conduct through.

8.7.5 Figure 8h, x-y plot of static temperature

The axial flow direction (z) is oriented in the horizontal direction from left to right. The axial midpoint is at z=0 here, so the fittings would start at z=-

3 and end at z=3. The plot represents the surface temperature of the channel wall in the axial direction.

(1) The sharp increase in the wall temperature is due to the large temperature differences and the small thermal mass of the tubing.

(2) The changes in wall temperature are detected in the transitions from the fittings to the bulk solid. Ideally, these should be sharp jumps in temperature. The closer the inlet fitting is to the fluid temperature the more valid the length them (L) is, as applied in equation 7.17.

8.7.6 Figure 8i, x-y plot of heat transfer coefficient.

Sharp drops in the heat transfer coefficient are shown with steps corresponding to the tubing transitioning to the fitting and then to the bulk solid. More than half of the 3 inch channel is below 1000 w/m^2K.

8.7.7 Figure 8j, contours of static temperature

This image is effectively the same as figure 8f, but for a turbulent flow rate. The are a few notable features such as:

(1) Uniform temperature field in the locations where thermocouples would be embedded in the solid. The star shaped isotherm around the heaters shows the temperature distribution due to the alternating heat source/sink pattern set up by the array.

(2) A shallower temperature gradient through the solid compared with the laminar case.

8.7.8 Figure 8k, contours of static temperature This image is effectively the same as figure 8g, but for a turbulent flow rate. Some notable features are:

(1) The effect of turbulence on the fluid temperature distribution is seen. Turbulence facilitates mixing in the fluid and promotes more interactions between the boundary layers and the bulk fluid, as compared to a laminar flow pattern.

(2) The heat transfer is much more effective in this case compared with the laminar case, seen in figure 8m. With the convection through the 3 inch channel length being enhanced, the conduction out through the fittings is not significant, therefore the validity of the length (L) term in equation 7.17 can be assumed.

8.7.9 Figure 8l, x-y plot of static temperature

This figure is an analog of figure 8h. The large steps in temperature at z= –1.5 and 1.5 inches are the ideal shape and support the assumptions stated in 8.6.8. A slight shadow of the fitting mass effect can be seen at –2.25 inches.

8.7.10 Figure 8m, x-y plot of heat transfer coefficient.

This figure can be interpreted the same as figure 8l and it follows a similar trend as figure 8l. One significant conclusion that can be drawn from this plot is that heat flux, being a proportional to the heat transfer coefficient, will not be constant in the axial direction. In this case it decreases by up to

14% of the z=-1.5 value. This is important because the laminar flow analysis assumes a constant heat flux wall.

8.7.11 Figure 8n, grid

This image shows the grid in a cross section for both the fluid and solid zones.

8.8 Performance comparison

8.8.1 Turbulent flow

Some results corresponding to the figures shown in this section for the turbulent flow case are listed below in figure 8o

	Experimental	Fluent	
Wall temp z=1	41.6	33.2	°C
Wall temp z=2	42.9	34.2	°C
heat transfer coefficient, z=1	7739	7000	W/m^{2}K
heat transfer coefficient, z=2	6925	6000	W/m^{2}K
Bulk fluid temp increase	2.08	1.79	C°
Heater temperature	46.1	40.3	°C

Figure 8o, experimental and Fluent data comparison

Overall, the simulation underpredicted the values by 10 to 20% compared to the experimental data.

8.8.2 Laminar flow

	Experimental	Fluent	
Wall temp z=1	73.52	82	°C
Wall temp z=2	74.98	83	°C
heat transfer coefficient, z=1	1876	1500	W/m^{2}K
heat transfer coefficient, z=2	1330	990	W/m^{2}K
Bulk fluid temp increase	4.65	15	C°
Heater temperature	83.9	85.6	°C

Figure 8p, experimental and Fluent data comparison

In this case, the data was either over or underpredicted by –25 to 10 %. The inconsistency in the trend can be cleared up by using a finer mesh at the coupled wall, since this case is so dependent on the phenomena near the wall.

Even with the differences in the numerical data, the model can still be used for quantitative assessments. Another comparison is given in section 9 against correlated values.

9 Verification of single phase data

9.1 Scope

The transport phenomena associated with single phase convective heat transfer in tubes has been well established in the engineering literature as outlined in Kakac, Shah and Aung (1987). Comparison of the data taken for single phase convective heat transfer can be used to substantiate the performance of the instrumentation. A successful comparison of the single phase data to the available correlations can be used to support the heat transfer data taken in the flow boiling regime.

9.2 Approach

There were two approaches taken to verify the validity of the instrumentation.

(1) Selecting empirical correlations for laminar and turbulent flow which can be fit to the data.

(2) Postprocessing of the CFD solution to generate x-y charts and alphanumerics which can be compared to the data.

9.3 Procedure

9.3.1 Overview

For the empirical correlations the procedure used is based on the equations outlined in section 7, data reduction. Data is acquired and processed in a spreadsheet which includes thermocouple linearization and

determination of an experimental Nusselt number. The choice of the empirical correlation used is based on the critical Reynolds number (ReD≈2300)

The steps outlined in section 8, CFD simulations are used for generating and extracting solution data.

9.3.1.1 Turbulent flow data

A predicted local Nusselt number is calculated directly from the Gnielinski correlation which is valid for turbulent, fully developed flow with $0.5<Pr<2000$ and $3000<Re_D< 5 \times 10^6$.

9.3.1.2 Laminar flow data

The local Nusselt number is predicted based on the thermal entry length and the inverse Graetz number. The correlation is based on a chart found in figure 7b and is valid for determining Nusselt numbers for the Gz^{-1} range of 10^{-2} to 10^{-4} and a Pr of about 5. This is suitable for water in a thermally non-fully developed setting. This assumption is realistic because the test section is a short tube with an unheated starting length, so the flow can only be considered fully developed hydrodynamically.

9.3.1.3 CFD data

The software is able to export x-y plots for surfaces, such as the channel wall, in the axial (z) direction. The alphanumerics are extracted and compared to the data.

9.4 Results

The results are tabulated and summarized in figures 9a for turbulent flow, figure 9b for laminar flow and figure 9c for the CFD case.

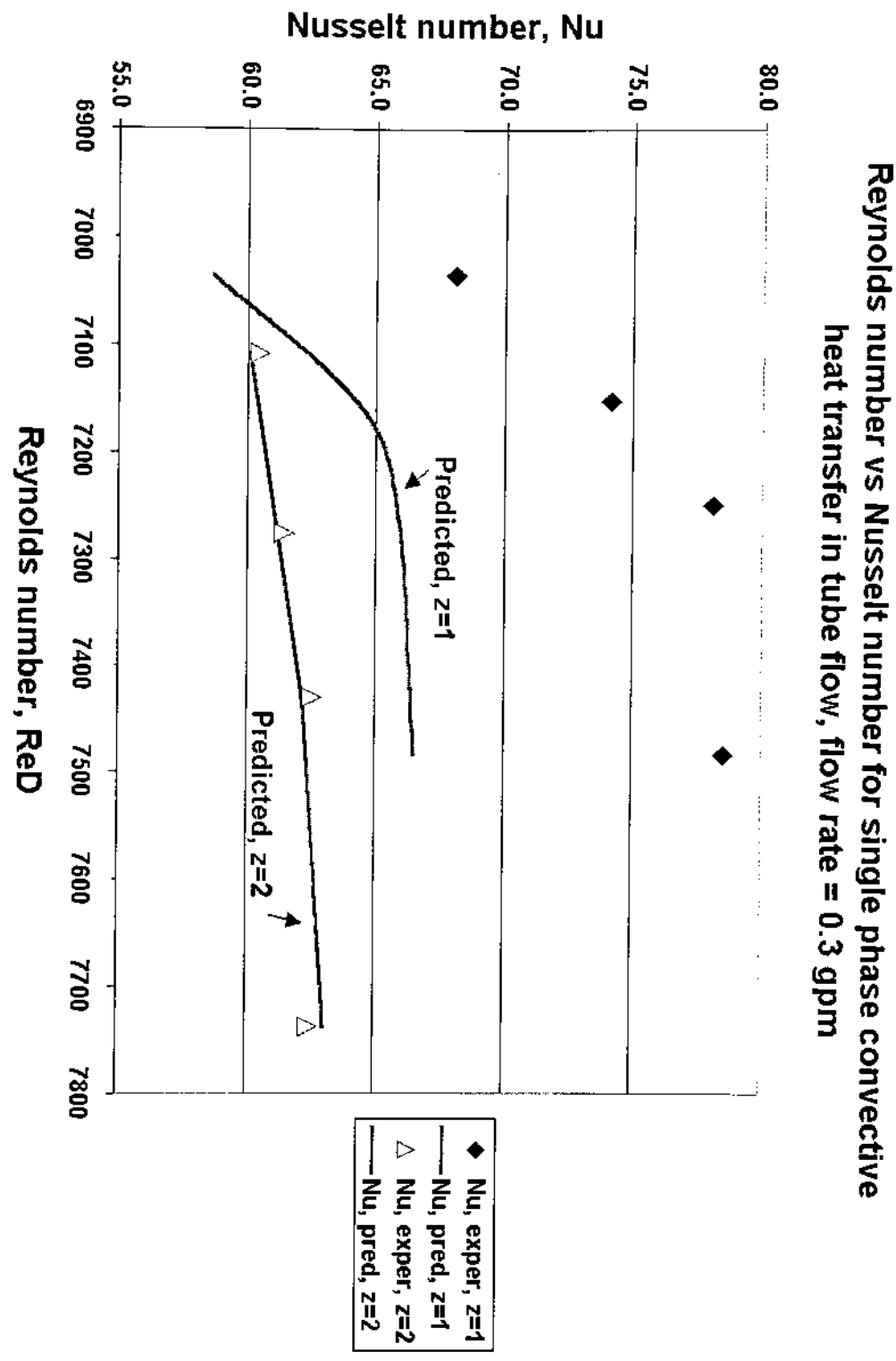

Figure 9a, comparison of data for turbulent Reynolds numbers

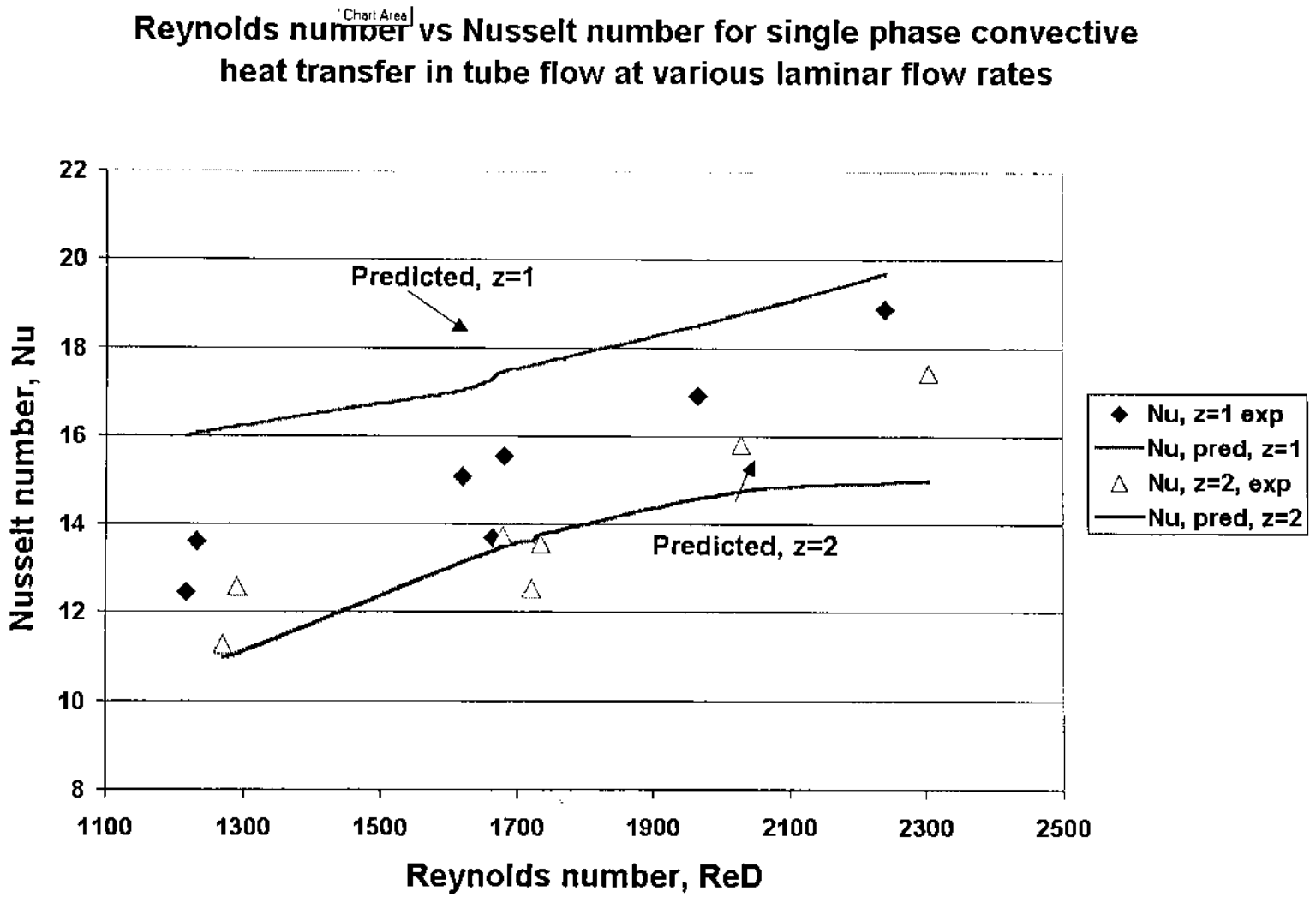

Figure 9b, comparison of data for laminar Reynolds numbers

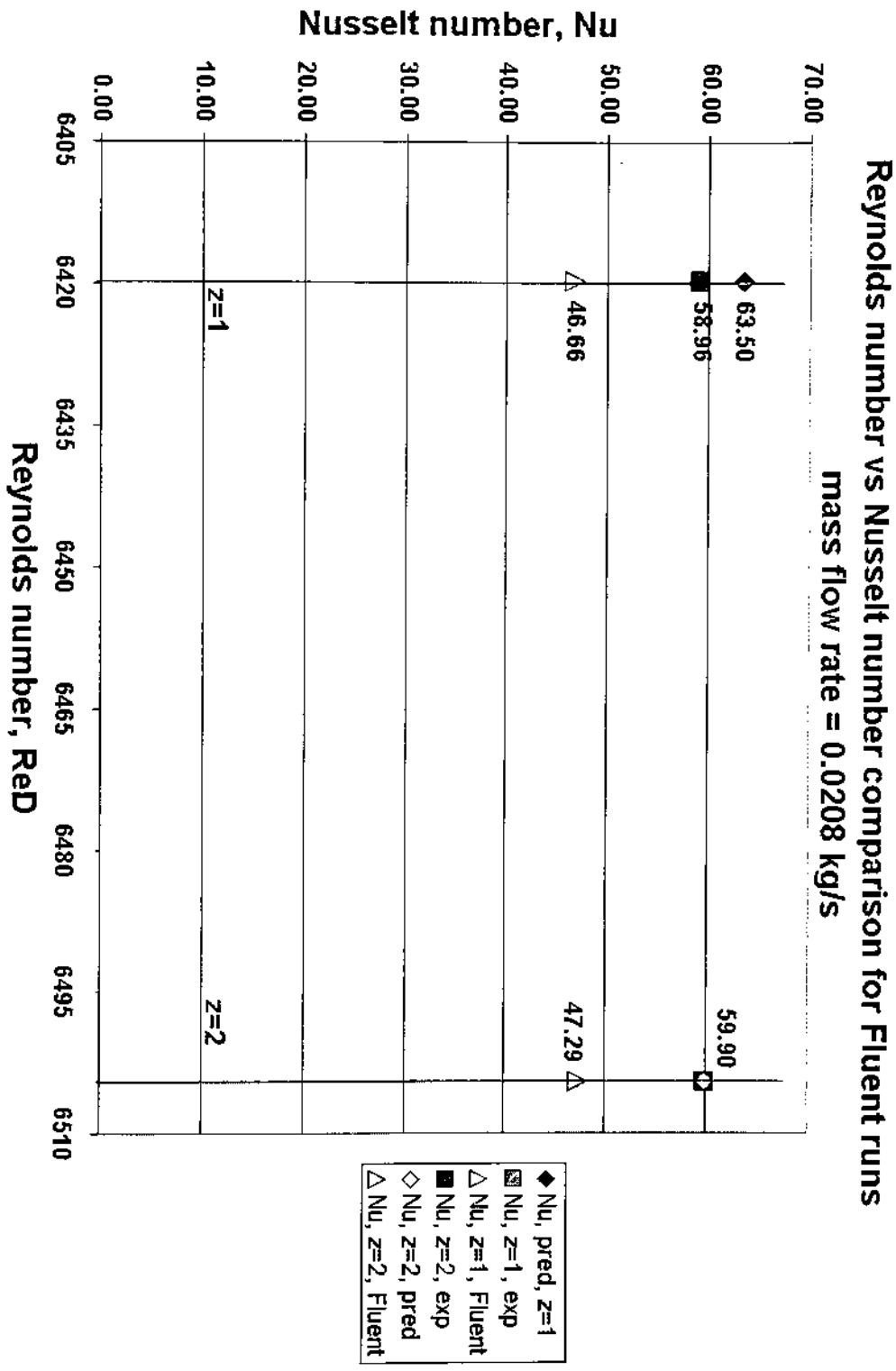

Figure 9c, comparison of data for a turbulent Reynolds number CFD simulation

9.5 Discussion of correlation

9.5.1 Turbulent flow

The trends of the data match expected system behavior for this case with Nusselt number increasing with Reynolds number. Also, the z=1 station experiences a higher Nusselt number than the z=2 station, due to the higher degree of subcooling in the bulk fluid. Figure 9e shows a plot of how the Gnielinski correlation values deviate from the experimental data values. The correlated values at the z=1 station are off by approximately –15% compared with the experimental values. The z=2 station had values predicted that were no more than 1% different than the experimental values.

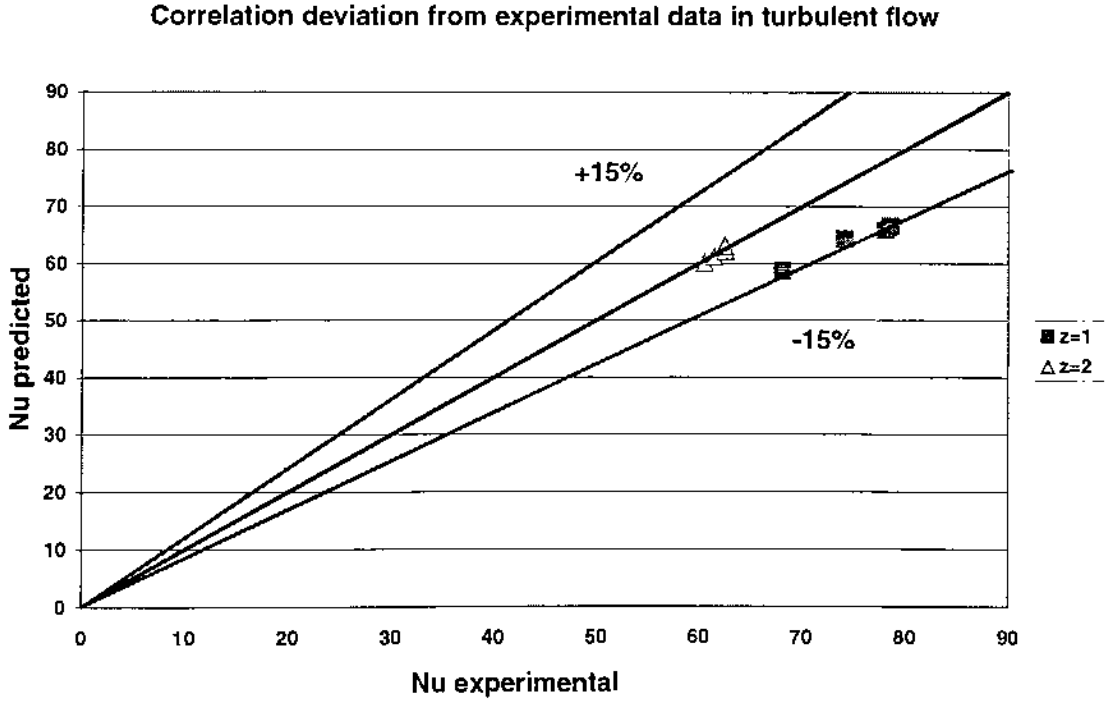

Figure 9e, Percentage of error in turbulent Gnielinski correlation with respect to experimental data. 15% criteria is based on z=1 values.

9.5.2 Laminar flow data

The predicted trends follow the experimental data up to a transitional Reynolds number where there is divergence. Figure 9f shows a plot of how the Graetz number correlation values deviate from the experimental data values. The chart overpredicted the values for the z=1 station between 10 to 15% where the values for the z=2 station were underpredicted by an average of – 4%.

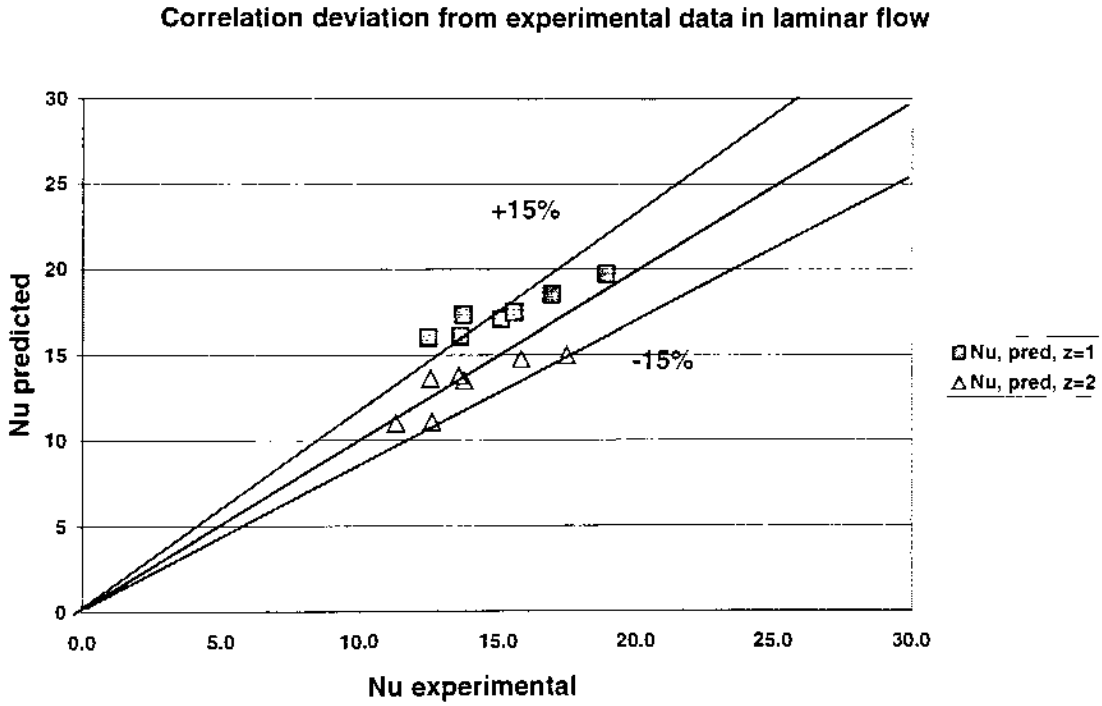

Figure 9f, Percentage of error in laminar correlation with respect to experimental data. 15% criteria is based on z=1 values.

9.5.3 CFD Simulations

The simulation underpredicted the experimental data by 21% for the z=2 station and by 26% for the z=1 station. This discrepancy does not necessarily invalidate the CFD model. CFD modeling often requires modifying constants and adapting grids to simulate the process better. In this case the κ-ε turbulence constant can be increased or the thermal/viscous boundary layers meshed with a finer grid to promote more interaction at the wall.

9.6 Conclusions for validation

9.6.1 Turbulent flow

It becomes evident that there may be an issue with applying the assumptions of the Gnielinski correlation at the z=1 station. Provisions were made in the experiment to develop the flow hydrodynamically, but since it is a short heated tube, thermal entrance length considerations must be made. The z=2 station does not seem to experience this problem. The analysis of Notter and Sleicher (1957) is presented in Kakac, Shah and Aung (1987) (pp 4.50-4.53) for the thermal entry length problem in turbulent flow for a Prandtl number of 3 the approximate thermal entry length is 2.86 cm (1.25 inches). This can be used to account for the discrepancy in the data presented in figure 9a.

The preliminary conclusion is that the z=2 is a reliable station to acquire data from. It is recognized that the Gnielinski correlation can be associated with errors of up to 10% but for this case the system and the

correlation are well matched. The data presented supports the recommendation of Kandlikar (1998) to use the Gnielinski correlation in conjunction with the nucleate dominant boiling heat transfer coefficient correlation, Kandlikar (1990,1991).

9.6.2 Laminar flow

The data supports the recommendation made in the present work to focus on the z=2 station for data acquisition. The use of a lookup chart makes the determination of the Nusselt number somewhat less automated than the method used in the turbulent case and is suspected to lead to a readoff error of +/-1 Nu.

9.6.3 CFD simulation

20-26% error is outside of the acceptable criteria for engineering approximations if it assumed the above data are correct. Refinements can be made to the model based on the recommendations in section 9.5.3. The model can still be used to make qualitative conclusions for the experiment.

10 Experimental results

10.1 Scope

The purpose of this section is to provide the results of the experiments in graphical form. The results of flow boiling experiments have three correlations fitted to them. Included after these results are data for CHF and film boiling. The following sections will be devoted to discussion and error analysis.

10.2 Single phase data

The single phase data acquired for the runs reported in this section were used to supply a parameter for the equations used to correlate fully developed boiling.

10.3 Nucleate boiling data

Data acquired for nucleate boiling focused on the fully developed boiling region as found in figures 10 a,b and c. The data for three different flow rates and subcooled inlet temperatures are reported. These are fit with three correlations available in literature for heat flux (q"). It should be emphasized that the correlations fitted are valid for the fully developed boiling region, which means that the contribution from nucleate boiling dominates the heat transfer, compared to the contribution from convective heat transfer. The bulk fluid temperature is plotted in figures 10 a,b and c as an indication of the fully developed boiling conditions present.

(1) Kandlikar (1998)

$$q'' = \left[1058\left(Gh_{lf}\right)^{-0.7} F_{fl}\alpha_{lo}\Delta T_{sat}\right]^{(1/0.3)} \qquad \textbf{(10.1)}$$

Where the fluid surface parameter F_{fl} is equal to 1 in this case. G is the mass flux, h_{lf} is the heat of vaporization, α_{lo} is the single phase heat transfer coefficient and ΔT_{sat} is the excess wall temperature.

(2) Shah (1977)

$$q'' = \left[\left(230Gh_{lf}\right)^{-0.5}\alpha_{lo}\Delta T_{sat}\right]^{2} \qquad \textbf{(10.2)}$$

Many of the same parameters as equation 10.1 are used. G is the mass flux, h_{lf} is the heat of vaporization, α_{lo} is the single phase heat transfer coefficient and ΔT_{sat} is the excess wall temperature.

(3) Jens and Lottes (1951)

$$q'' = \left(\frac{\Delta T_{sat}}{e^{\frac{p}{62}}}\right)^{\frac{1}{0.25}} \qquad \textbf{(10.3)}$$

Uses only ΔT_{sat} and the pressure, *p* as the variables.

10.4 Critical Heat flux

Critical heat flux was used as a design criterion for the test section. It was reached experimentally during flow rate excursions due to vapor generated backpressure. Measurements of the CHF were taken for near saturated inlet temperatures and very low flow rates. Figure 10d reports a measurement of CHF.

10.5 Film Boiling

Data were acquired for transition and fully developed film boiling as shown in figure 10e. Measurements were possible in the heating up as well as cooling down directions. For concern of burnout, power to the heaters was cancelled before radiation effects became significant. Therefore the upward inflection in the right portion of boiling curve is not observed in the data.

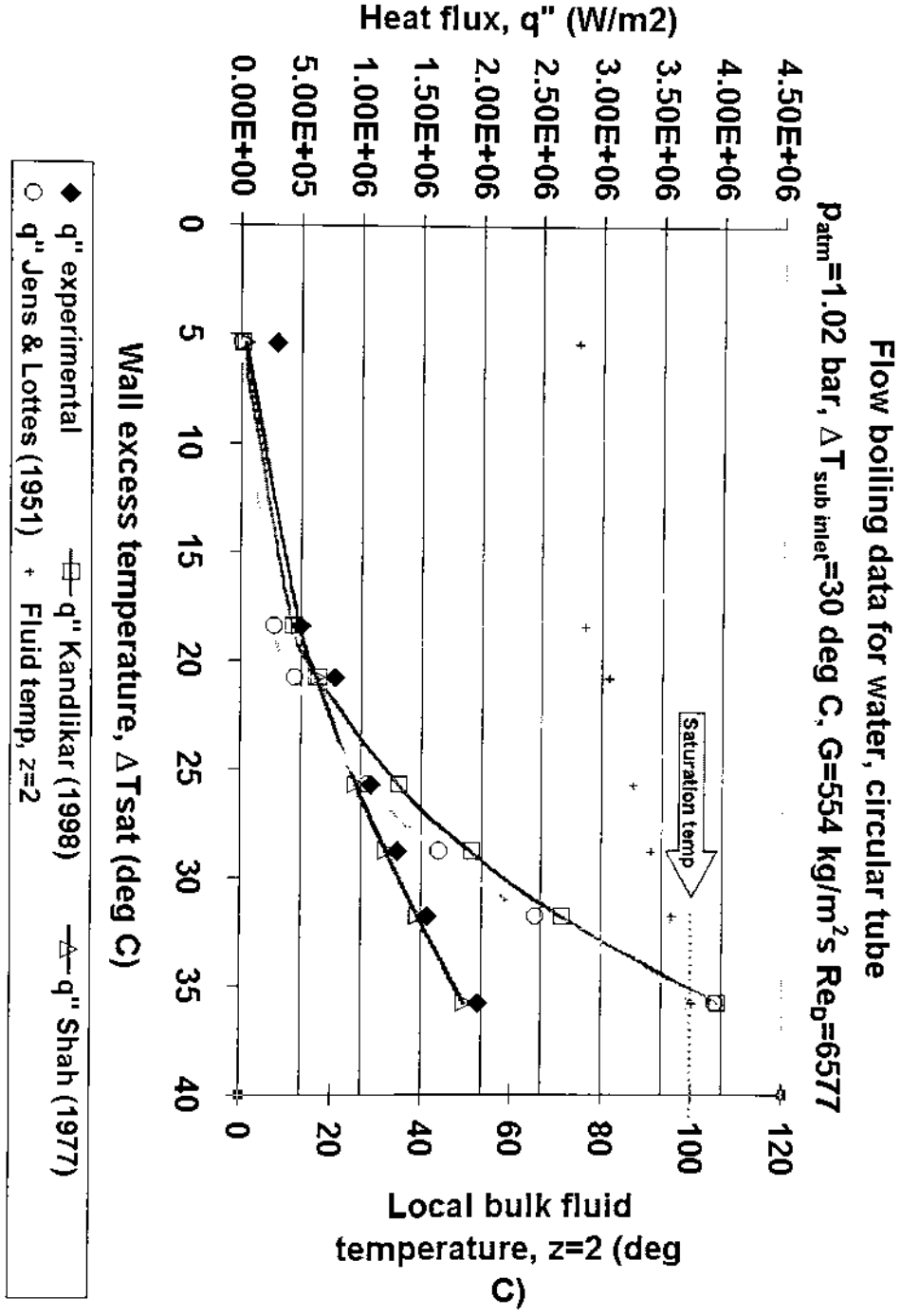

Figure 10a, Comparison of subcooled flow boiling data with Shah correlation (1977) .

(Also shown are FDB correlations by Jens & Lottes (1951) and Kandlikar (1998))

p_atm=1.02 bar, subcooled inlet temp =30 deg C, G=554 kg/m^{2}s ReD =6577

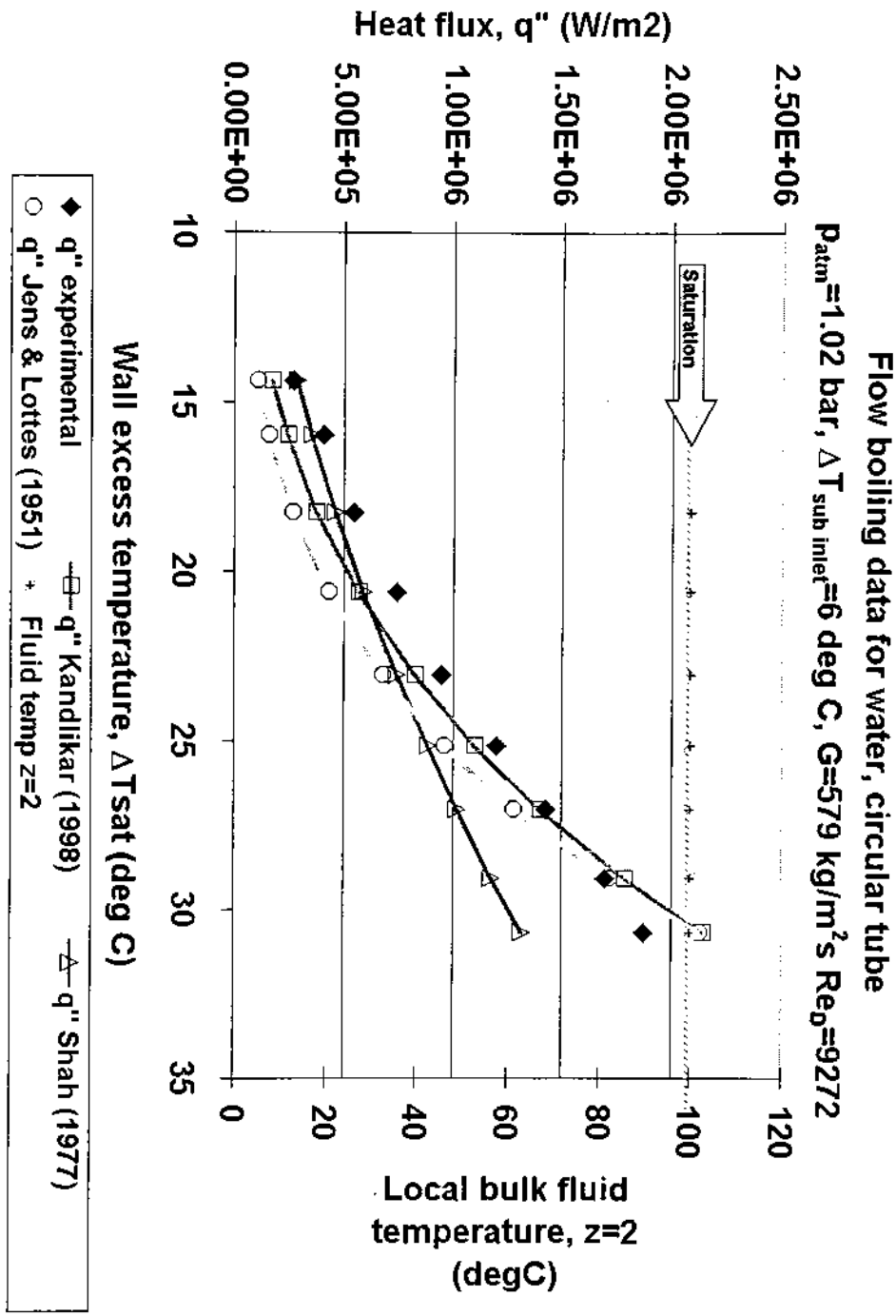

Figure 10b, Comparison of subcooled flow boiling data with Shah correlation (1977) . (Also shown are FDB correlations by Jens & Lottes (1951) and Kandlikar (1998))

p_atm=1.02 bar, subcooled inlet temp =6 deg C, G=579 kg/m^{2}s ReD =9272

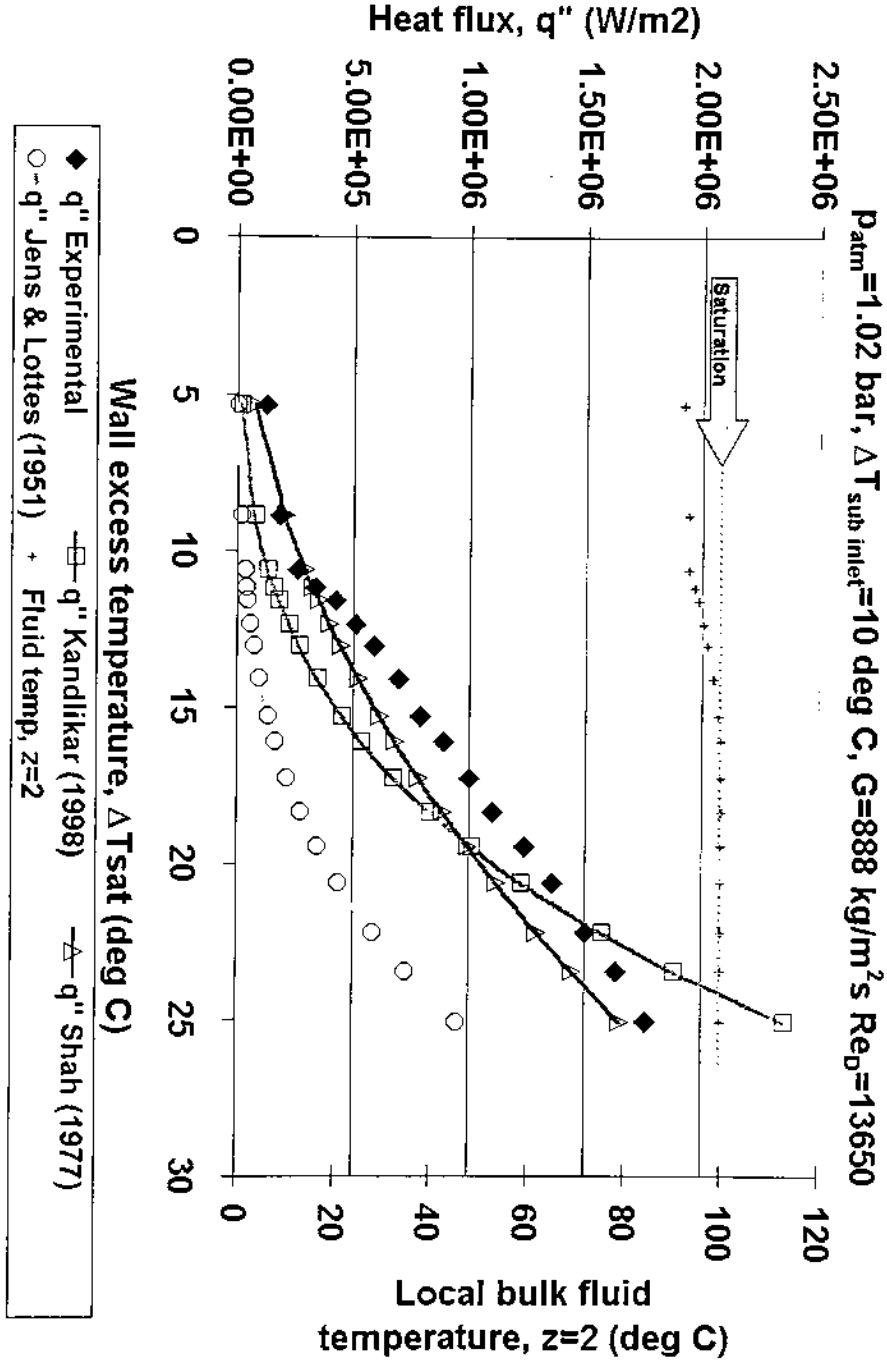

Figure 10c, Comparison of subcooled flow boiling data with Shah correlation (1977) . (Also shown are FDB correlations by Jens & Lottes (1951) and Kandlikar (1998)) p_atm=1.02 bar, subcooled inlet temp=10 deg C, G=888 kg/m^{2}s ReD=13650

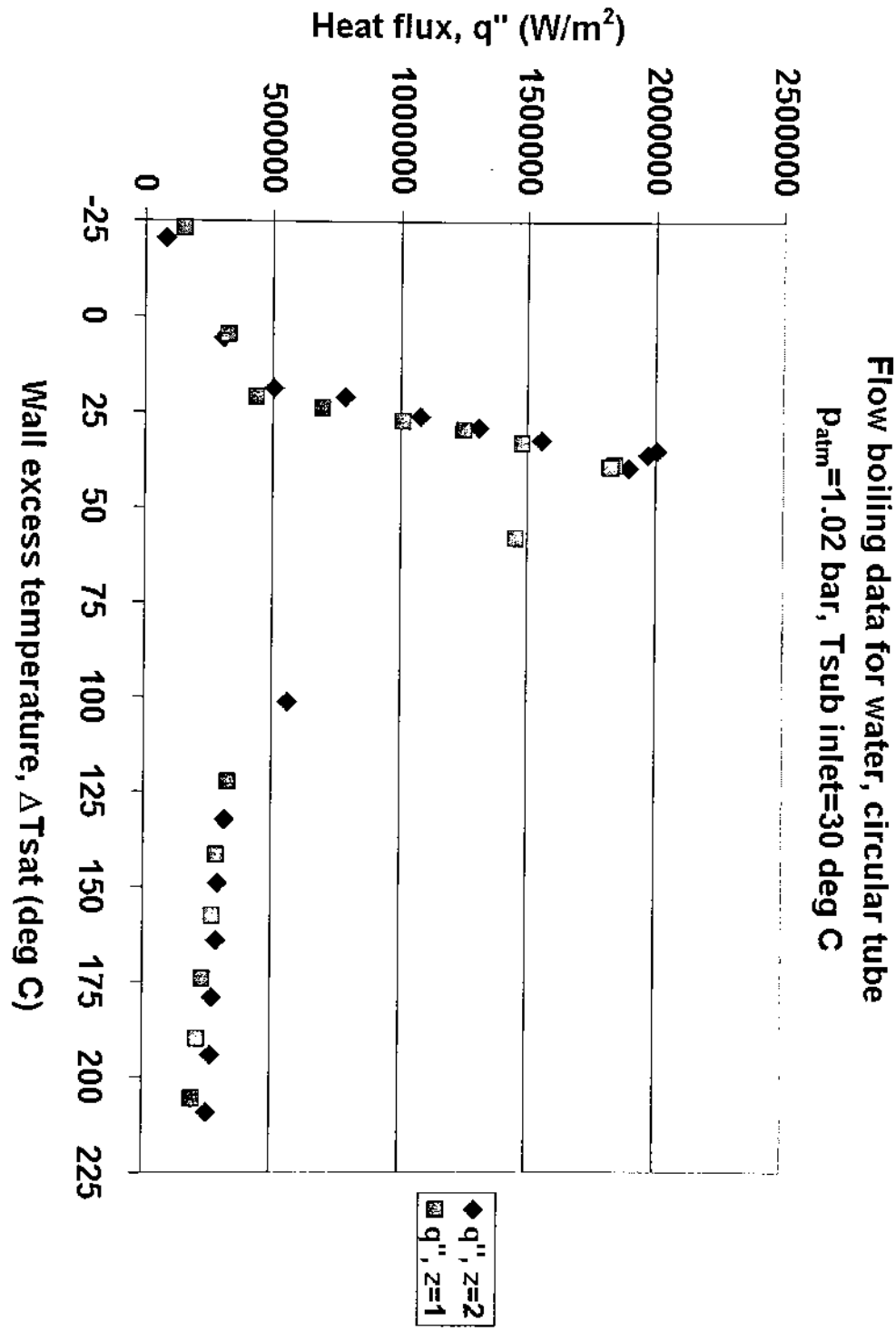

Figure 10d, Boiling curve illustrated experimentally, from single phase to film boiling

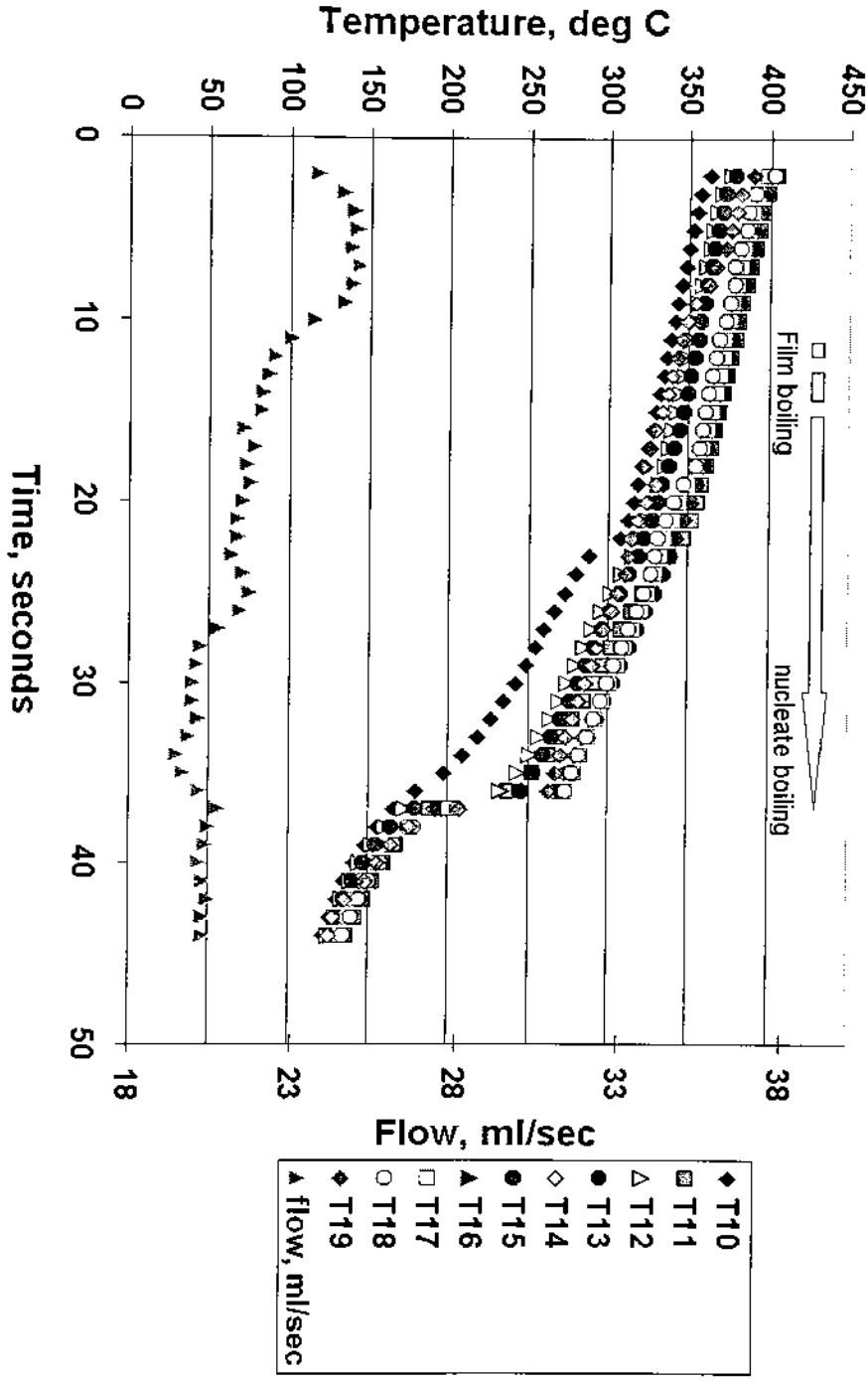

Figure 10e, Transient temperatures taken at axial locations 1.4 mm from channel wall. Further reduction of the data with transient conduction equations will yield heat flux values

11 Discussion

11.1 Fully developed nucleate boiling

It becomes necessary to differentiate between the various boiling regimes when analyzing the data. The accepted model to determine the location of the fully developed boiling has been given by Bowring (1962). This method involves a few geometric construction curves to be drawn, namely an extension of the single phase line and the extension of the fully developed curve into the partial boiling region. The heat flux (q''_D) at the intersection is transcribed over to the boiling curve horizontally and a heat flux value is read off of the boiling curve. The correlation, developed by Forster and Grief and reported by Bowring is give by the relation

$$q''_{FDB} = 1.4 q''_D \qquad \textbf{(11.1)}$$

As the inlet temperature approaches saturation, it becomes necessary to determine the occurrence of saturated flow boiling as well. A simple criterion for this is to compare the local bulk fluid temperature to the saturation temperature. A local bulk fluid temperature close to the saturation temperature may indicate a transition from the subcooled into the saturated boiling regime.

11.2 Correlation of the equations with data in literature

After comparing the Jens and Lottes (1951) correlation with more extensive data Thom et al. (1965) found that the correlation underpredicted their data. The Shah correlation (1977) uses a database of twelve fluids from

fifteen different sources. There is no clear distinction between the fully developed boiling and partial boiling regions. It also appears that the $q'' \propto \Delta T_{sat}$ is not supported by data. One of the significant features of the Kandlikar correlation (1998) is said to be its ability to predict the trends in the heat transfer coefficient vs. quality in the lower quality region. All of the FDB correlations used in the present study have been reported as valid for water.

11.3 Discussion of figure 10a

The data in Figure 10 is characterized by a high inlet subcooling and moderate flow rates. The q''_{FDB} is about $7*10^5$ W/m^2 for this run and there is a high amount of divergence in the Kandlikar and Jens & Lottes correlations after this point. The local bulk temperature was calculated to stay below saturation until wall superheats of $35C^0$, so the experimental configuration would appear to be ideal for mapping the FDB correlations. The Shah correlation represented the trend the closest, within 10% or lower difference after q''_{FDB}. Figure 11a shows the error scatter graphically.

11.4 Discusion of figure 10b

This data is characterized by a relatively low inlet subcooling which makes the transition into saturated boiling realistic at higher wall superheats. The calculation of the local bulk fluid temperature indicates a near saturation condition, which may explain the divergence of the Shah correlation at the higher wall superheats. Alternatively, the intersection of the data with the Kandlikar and Jens & Lottes correlations may suggest agreement with FDB conditions. Although the bulk fluid temperature indicates saturation, it is only a

mean temperature which does not account for heat transfer in partial boiling. The $q"_{FDB}$ would likely occur at around $3*10^5$ W/m^2 for this run, but the uncertainty associated with the single phase data at inlet temperatures close to saturation propagates into the calculation of $q"_{FDB}$. All three correlations underpredict the data on the left half of the curve. This is consistent with the trends reported in the literature for the Shah and Jens & Lottes correlations. The best agreement is with the Kandlikar and Jens & Lottes formulas in the region suspected to be in saturated boiling. Figure 11b shows the error distribution for this run graphically.

11.5 Discussion of figure 10c

$q"_{FDB}$ was calculated to occur near $3.7*10^5$ W/m^2 for this run. Two of the correlations intersected the data, the Shah correlation at low superheats and the Kandlikar correlation at high superheats. The overall trend was an underprediction of the correlated values. The amount of vapor generation at the outlet noted during the experiment would seem to indicate that saturated boiling was occurring at the higher superheats. Figure 11c shows the error graphically.

11.6 Discussion of figure 10d

A boiling curve constructed with experimental data points shows four heat transfer regimes, the single phase, the nucleate boiling up to CHF, CHF to transition film boiling and lastly, film boiling with inverted annular flow. The range of wall temperatures and heat fluxes achievable underscore the apparatus' versatility.

11.7 Discussion of figure 10e

The transient data for transitional film boiling in the cooling down mode is presented as a function of the near wall temperature. Since this run has to do with transient conduction, another equation is to be used to translate the data into heat flux. The temperatures appear to drop more sharply as the axial (z) location approaches the outlet. There is also some variation in the flow rate due to the vapor-generated backpressure. The run progressed with a tranquil beginning in film boiling and finished with a violent roar as the vapor blanket collapsed returning the heat transfer back into nucleate boiling.

Figure 11a, Error scatter in Re=6577 case

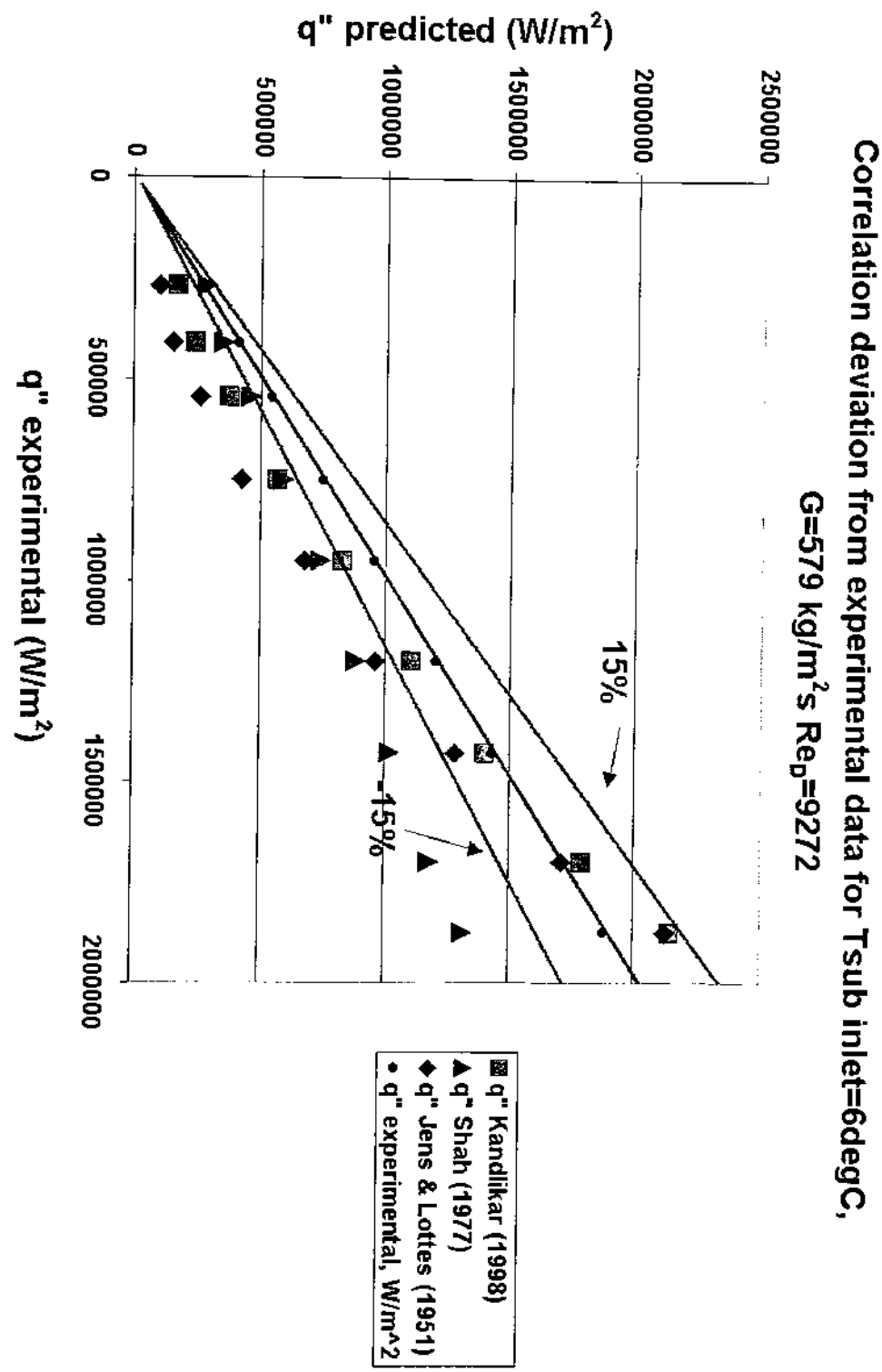

Figure 11b, Error scatter in Re=9272 case

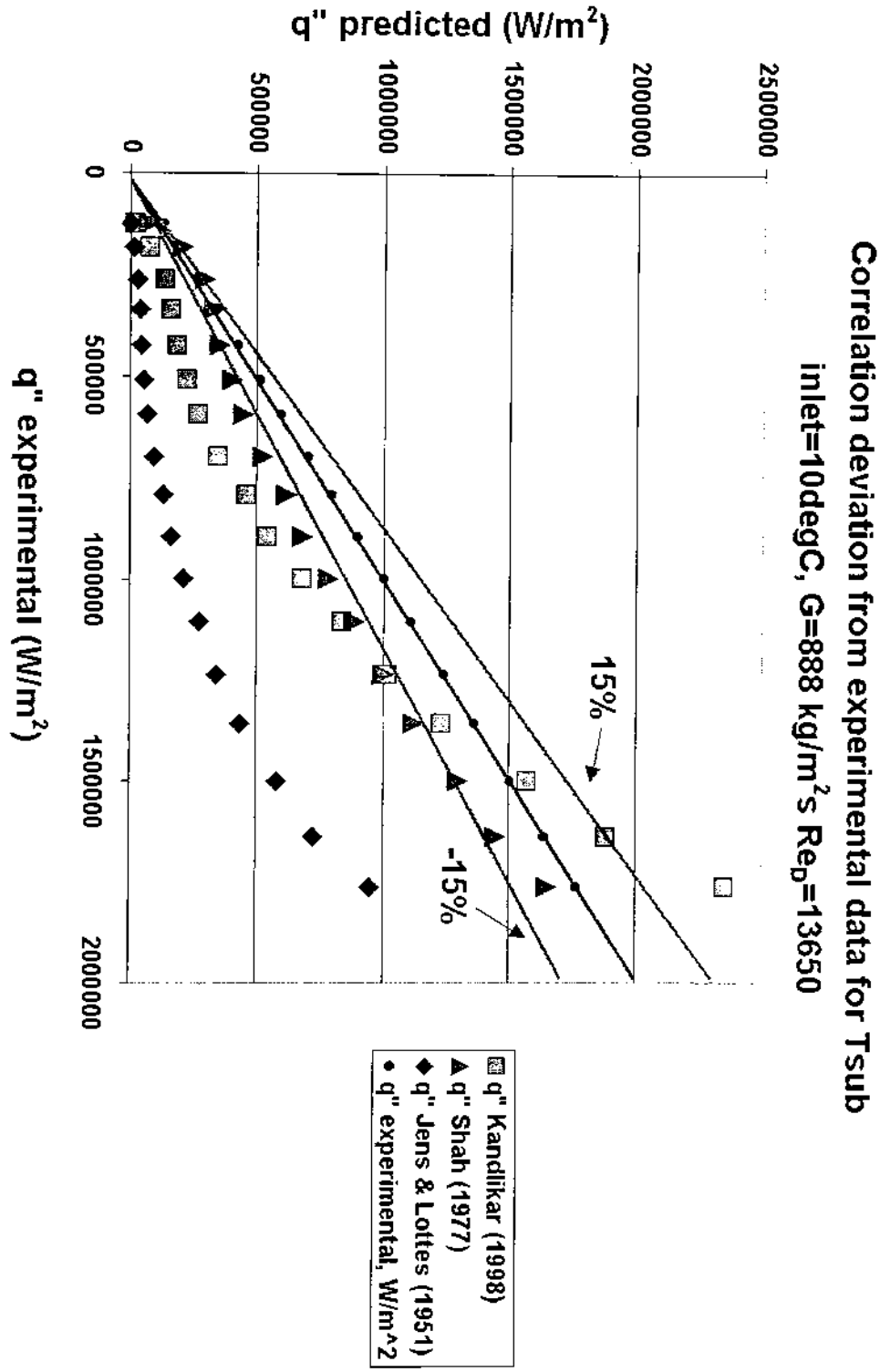

Figure 11c, Error scatter in Re=13650 case

12 Uncertainty analysis

12.1 Scope

An experimental result will involve some level of uncertainty that may be caused by lack of accuracy in measurement equipment, random variations in the measurements and approximations in the data reduction relations. Error from individual sources combine in the governing equations such as for heat flux and surface temperature and translate into uncertainty in the final results.

The calculations shown in this section are representative of a test with an inlet subcooling of 10 deg C, a mass flow rate of 888 kg/m^{2}s and a Reynolds number of 13650. A confidence level of 95% is assumed throughout this analysis.

The uncertainty U is obtained from its components, the bias limit B and the precision limit P by equation 11.1

$$U^2=B^2+P^2 \qquad \textbf{(12.1)}$$

12.2 Bias limit

Bias limit is an estimate of the magnitude of the fixed error. The value for bias limit can be determined from calibration or taken from manufacturer's specifications. The bias limit can be calculated from the following equation.

$$B_R = \left[\sum_{i=1}^{n}\left(B_i \frac{\partial R}{\partial x_i}\right)^2\right]^{1/2} \qquad \textbf{(12.2)}$$

12.3 Precision limit

Precision limit is an estimate of the lack of repeatability caused by random errors. The precision limit for a single measurement variable can be obtained from

$$P_x = t\, S_x \qquad \textbf{(12.3)}$$

where t is the value of the Student's *t* distribution table for the degrees of freedom *v* and *S* is the standard deviation. If the sample sizes used to determine the precision uncertainties are greater than 30 the *t* value is only a function of the confidence interval. For a 95% confidence level the precision limits can be calculated from 2 times the standard deviation. For calculated parameters the precision limit can be determined by using the following formula.

$$P_R = \left[\sum_{i=1}^{n} \left(P_i \frac{\partial R}{\partial x_i} \right)^2 \right]^{1/2} \qquad \textbf{(12.4)}$$

12.4 Uncertainty

The total uncertainty can be calculated by rearranging equation 12.1. in a sum squared root formula.

$$U_R = \sqrt{B_R^{\,2} + P_R^{\,2}} \qquad \textbf{(12.5)}$$

12.5 Summary

Figure 12.1 shows that the uncertainty in heat flux can be very significant at low heat fluxes and approaches a steady value at higher heat fluxes. This effect is primarily due to smaller differences in the temperature values T2 and T4. In general, the bias uncertainty is the major contribution. The low precision uncertainty is due solely to the degree of repeatability in the thermocouples.

Temperature measurements, T2 and T4	0.2	K
Thermocouple location	0.15	mm
Thermal conductivity	3	W/mK

Table 12.1, Bias limits used in calculations

Uncertainty associated in the calculation of heat flux

q", z=2	Precision %	Bias %	Uncertainty %
125584	4.99	43.19	43.48
182671	3.43	30.87	31.06
260724	2.40	23.16	23.28
336282	1.86	19.40	19.49
422100	1.48	16.97	17.04
508734	1.23	15.50	15.55
592702	1.06	14.58	14.62
696873	0.90	13.82	13.85
790230	0.79	13.36	13.39
893597	0.70	13.00	13.02
998514	0.63	12.74	12.75
1103777	0.57	12.54	12.55
1237152	0.51	12.36	12.37
1357887	0.46	12.23	12.24
1500888	0.42	12.12	12.13
1636525	0.38	12.04	12.05
1762011	0.36	11.98	11.99

Table 12.2, Heat flux uncertainty

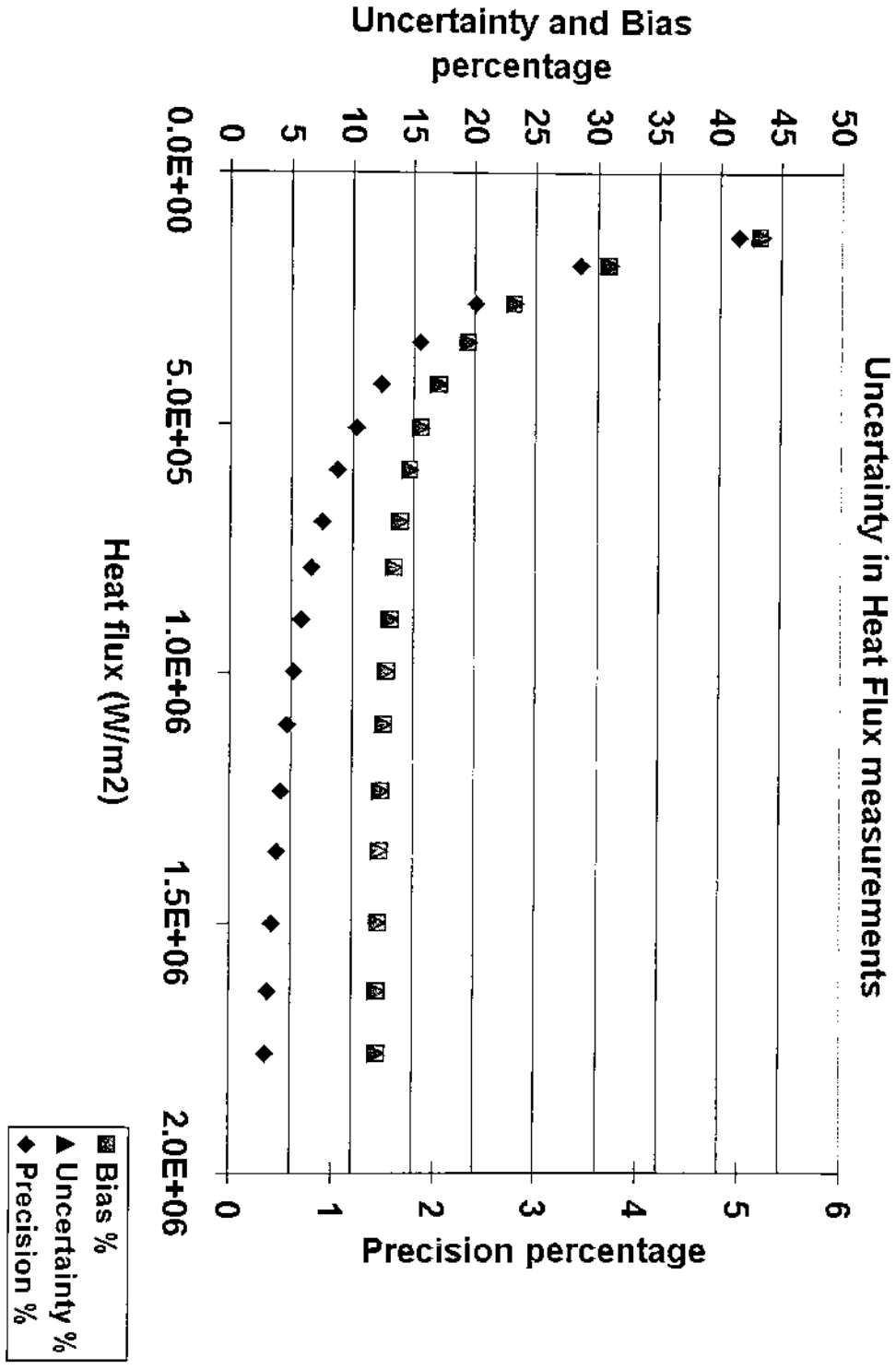

Figure 12.1, Uncertainty in heat flux measurements, Inlet subcooling =10°C, G=888 kg/m^{2}s and Re =13650.

13 Conclusions

This paper has provided a fundamental study on the characteristics of boiling heat transfer in a circular tube. The apparatus was analyzed critically and its validity established so that future testing may be performed.

13.1 Recommendations for further research

13.1.1 Transient film boiling data

To further the study of transition film boiling based on the database developed in this study, an equation will have to be developed to account for the transient conduction in a hollow cylinder. The problem is inverted, in that the temperature distribution is known and the values at the boundaries are desired. Özisik (1980) gives a table of solutions to the transient hollow cylinder problem in terms of Bessel functions. Assuming the temperature distribution has no z dependence, the form of the transient heat conduction equation is given by

$$\frac{\partial^2 T}{\partial r^2}+\frac{1}{r}\frac{\partial T}{\partial r}+\frac{1}{r^2}\frac{\partial^2 T}{\partial \phi^2}=\frac{1}{\alpha}\frac{\partial T}{\partial t} \qquad \textbf{(13.1)}$$

The separated equations and their elementary solutions become

$$\frac{d^2 R\nu}{dr^2}+\frac{1}{r}\frac{dR_\nu}{dr}+\left(\beta_2-\frac{\nu^2}{r^2}\right)R_\nu=0 \qquad \textbf{(13.2)}$$

$$R_\nu(\beta,r): J_\nu(\beta r) and\ \mathrm{Y}_\nu(\beta r)$$

Özisik lists an solution that uses an adiabatic outer surface boundary condition and an inner surface boundary condition as a form of the Biot

number. Carslaw and Jaeger also give solutions to equation 13.1 based on Laplace transforms or Green's functions.

13.2 Improvements in the experimental equipment

Studies in the augmentation of CHF could be furthered if the test section were modified. The surface area of the channel plays an important role in the wattage-density that the fluid is exposed to. A smaller diameter channel will allow critical heat flux to be achieved with fewer demands on the power supply equipment because any heat rate will be focused on a smaller area, making it more concentrated. Literature has indicated that CHF increases with decreasing diameter, but in a case where the diameter is decreased by a factor of 1.5 the CHF will only be increased by a factor of 1.13.

The concept of a compression fitting has proven to be reliable in sealing and convenient in field stripping for cleaning. CFD analysis has shown that the conduction losses through the fittings can vary depending on the heat transfer coefficient. Turning down the wall thickness of the neck between the threaded portion of the fitting and the test section body can further reduce the heat flux into the fittings. Currently the wall thickness is 3/32 inches (2.38 mm). This can be re-machined to half of the present wall thickness (to 3/64 inches) as long as filleting is incorporated for smooth transitions.

The FTB-101 turbine flow meter from Omega engineering is designed to give readings within +/- ½% for flow ranges of 0.35 to 3.5 gallons per minute of water. At flow rates below 0.2 gpm, which is where CHF was attainable with the equipment at hand, steady readings were difficult to obtain. If flow rate is a parameter, then a flow meter in the 0.1-2 liter per minute (0.026-0.53 gpm) range is mandatory. The FTB601 model from Omega engineering fits the specifications for the flow rate. This can be perhaps the best investment to improve the test stand on its own. As was mentioned in earlier sections, the occurrence of vapor generation influences the backpressure in the flow loop and thus the flow rate immensely. In fully developed boiling, adjustments must be made after each change in heat rate to maintain a constant flow rate. It is highly recommended that a low range flowmeter be installed in this test stand.

Fabricating a new test section from 4-inch diameter stock could reduce the error associated with the radial location of the thermocouples. The new layout would facilitate more distance between the probes while maintaining locations in radially uniform temperature fields.

Aggour, M.A., 1979 "Hydrodynamics and heat transfer of two-phase two-component flows" Ph.D. thesis, University of Manitoba,

Bejan, Adrian "Heat Transfer" 1993 John Wiley and Sons, pp 305 New York

Berenson, P.J., 1962, "Experiments on pool boiling heat transfer" Int'l J. of Heat and Mass Transfer, vol. 5, pp. 985-999.

Bergelson, B.R., 1980, "Burnout under conditions of subcooled boiling and forced convection", Thermal engineering, Vol. 27, n.1, pp. 48-50.

Bergles, A.E. 1963, "Subcooled burnout in tubes of small diameter" ASME Paper 63-WA-182

Bowring, W. R., 1962, "Physical model of bubble detachment and void volume in subcooled boiling" OECD Halden reactor project report HPR-10

Boyd, R.D., 1985, "Subcooled flow boiling critical heat flux (CHF) and its application to fusion energy components, part 1: A review of fundamentals of CHF and related data base" Fusion Technology, Vol. 7, n.1, pp. 7-30

Carslaw, H.S, Jaeger, J.C., "Conduction of heat in solids", 1959, Oxford University press, pp 334 & 353

Celata, G.P., 1998 "Critical heat flux in subcooled flow boiling", Heat and Technology, vol 16, n.1,

Celata, G.P., Cumo, M. and Mariani, A., 1994c "Assesment of correlations and models for the prediction of CHF in subcooled flow boiling" Int J. of heat and Mass Transfer Vol. 37, n. 2, pp 237-255.

Celata, G.P., Cumo, M., Inasaka, F., Mariani, A. and Nariai, H., 1993b, "Influence of channel diameter on subcooled flow boiling burnout at high heat fluxes". Int Jou of Heat and Mass Transfer, Vol 36, n. 5, pp 1269-1285.

Celata, G.P., Cumo, M., Katto, Y. and Mariani, A. 1998a, "A new mechanistic model for the prediction of the CHF in water subcooled flow boiling" Proc. 3rd int'l Conference on Multiphase flow, Lyon, 8-12 June.

Celata, G.P., Cumo, M., Mariani, A., Simoncini, M. and Zummo, G., 1994c, "Rationalization of existing mechanistic models for the prediction of water subcooled flow boiling critical heat flux" Intnl J. Heat and Mass Transfer, vol. 37, suppl. 1, pp. 347-360.

Chen, J.C. and Hsu, K.K., 1995 "Heat transfer during liquid contact on superheated surfaces ASME JHT August, vol 177 pp 693

Chenoweth J.M. and M. Impagliazzo, Eds.; 1981 "Fouling in Heat Exchange Equipment" American Society of Mechanical Engineers Symposium Vol. HTD-17, ASME, New York,

Doroshchuk, VE, Levitan, LL, and Lantzman, F.P., 1975a, "Investigation into the burnout of heated tubes", ASME Paper, 75-WA/HT-22

Doroshchuk, VE, Levitan, LL, and Lantzman, F.P., 1975b, "Recommendation for calculating the burnout in a round tube with uniform heat release" Teploenergetika, Vol. 22, pp. 66-70

Engleberg-Forster, K. and Gref, R., 1959, "heat transfer to a boiling liquid-mechanism and correlations" Trans. ASME J. of Heat Transfer, Series C, 81, pp. 43-53

Fiori, M.P. and Bergles, A.E. 1970, "Model of the critical heat flux in subcooled flow boiling" , Fourth Intnl. Heat Transfer Conf., Paris-Versailles, vol. 4., B 6.3.

France, D.M., Carlson, R.D, Chiang, T. Priemer, R. 1978 "Characteristics of transition boiling in Sodium heated steam generator tubes", ASME, JHT vol 101 pp 270-275

Gnielinski, V., 1976 "New Equations for heat and mass transfer in turbulent pipe and channel flow", Int Chem eng. Vol 16, , pp 359-368

Groeneveld, D.C., Cheng, S.C., and Doan, T. 1986, AECLUO critical heat flux lookup table, Heat Transfer Engineering, Vol. 7, pp. 46-62.

Hebel, W., 1981, Detavernier, A., and Decreton, M., 1981, "A contribution to the hydrodynamics of flow boiling crisis in the forced flow of water" Nuclear Engineering and Design, Vol. 64, pp. 433-445.

Incropera, F and Dewitt, D Fundamentals of heat and Mass Transfer, 4th ed., 1996, John Wiley and sons, New York, p 835

Jens, W.H and Lottes, P.A, 1951, "An analysis of heat transfer, burnout pressure drop and density data for high pressure water" Argonne Natnl Lab report no. ANL-4627-1951

Kakac, S, Shah, R.K., Aung, W, "Handbook of single phase convective heat transfer". John Wiley and Sons, New York, 1987, chapter 3

Kandlikar, S.G, 1998 "Heat transfer characteristics in partial boiling, fully developed boiling and significant void flow regions of subcooled flow boiling" Journal of Heat Transfer, May 1998, vol 120, pp 395-401

Kandlikar, S.G. 1991, "Development of a flow boiling map for subcooled and saturated flow boiling of different fluids inside circular tubes" ASME Journal of Heat transfer, Vol. 113, pp. 190-200.

Kandlikar, S.G., 1990, "A general correlation for saturated two phase flow boiling inside horizontal and vertical tubes" ASME Journal of Heat transfer, Vol 112, pp. 219-228.

Katto, Y., 1990a, "A physical approach to critical heat flux of subcooled flow boiling in round tubes" Intnl J. Heat and Mass Transfer. Vol. 33, pp. 611-620.

Katto, Y., 1994, "Critical heat flux"", Int. Jou. Multiphase Flow, Vol. 20, Suppl., pp. 53-90

Katto, Y., 1995, "Critical heat flux mechanisms", Proc. Eng. Foundation Convective flow boiling conference, keynote lecture V, Banff, May.

Kutateladze, S.S., and Leontiev, A.I. 1966, "Some applications of the asymptotic theory of the turbulent boundary layer", Proc. 3rd Intnl Heat Transfer Conference, Chicago, Ill. Aug 8-12, vol. 3, pp. 1-6, AIChE, NY.

Lee, C.H. and Mudawar, I., 1988, A mechanistic critical heat flux model for subcooled flow boiling based on local bulk fluid conditions." Int'l J. Multiphase Flow, Vol. 711-728.

Moody, L.F., 1944, "Friction factors for pipe flow", Transactions of the ASME, vol. 66

Nariai, H., and Inasaka, F., 1992, "Critical heat flux and flow characteristics of subcooled flow boiling with water in narrow tubes" in Dynamics of Two Phase Flows, Jones, O.C. and Michiyoshi, I. Eds, CRC Press, pp 689-708.

Nariai, H., and Shimura, T. and Inasaka, F., 1987, "Critical heat flux of subcooled flow boiling in narrow tubes", ASME JSME Thermal Engineering Joint Conference, Honolulu, March 22-27

Notter, R.H. and Sleicher, C.A., 1972, "A solution to the turbulent Graetz problem III, Fully developed and entry region heat transfer rates" Chem. Eng. Sci. Vol. 27, pp. 2073-2093

Özisik, M. N., "Heat conduction" 1980, John Wiley and Sons, New York, pp 93-99

Shah, M.M., 1977, "A general correlation for the heat transfer during subcooled boiling in pipes and annuli" ASHRAE Trans, Vol. 83, Part 1, pp. 205-215

Styrikovich, M.A., Newstueva, E.I. and Dvorina, G.M., 1970, "The effect of two phase flow pattern on the nature of heat transfer crisis in boiling" Proc. 4th Int'l. Heat transfer Conference, Vol. 9., pp. 360-362, Hemisphere, New York.

Thom, J.R.S., Walker, W.M., Fallon, T.A. and Reising, G.F.S., 1965, "Boiling in subcooled water during flow up heated tubes or annuli", Presented at the symposium on boiling heat transfer in steam generating units and heat exchangers, Manchester, sept 15-16, Institute of Mech. Eng., London.

Tong, L.S., Currin, H.B., Larsen, P.S. and Smith, O.G., 1965, "Influence of axially non-uniform heat flux on DNB", AicHE Symposium Series Vol. 64, pp. 35-40.

Weisman, J. 1992, "The current status of theoretically based approaches to the prediction of critical heat flux in flow boiling" Nuclear Technology, Vol. 99, pp. 1-21, July.

Weisman, J. and Ying, S. H., 1983, "Theoretically based CHF prediction at low qualities and intermediate flows" Transaction American Nuclear Society, Vol. 45, pp. 832-833.

Appendix A

Experimental data

heater power input, W	inlet temperature, deg C	outet temperature, deg C	flow rate, gpm	wall superheat, deg C	q" experimental, W/m^2	q" Kandlikar (1998)	q" Shah (1977)	q" Jens & Lottes (1951)	Tfluid, z=2
216	94.2	99.3	0.16	14.4	268599	170314	288217	102064	100
306	94.2	100.3	0.20	15.9	407966	240974	354937	154787	100
413	94.3	100.3	0.19	18.2	543333	376631	464000	264527	100
536	94.2	100.3	0.15	20.6	745648	564760	591680	430138	100
674	94.3	100.5	0.21	23.0	949558	823369	741865	676213	100
829	94.3	100.4	0.19	25.2	1198896	1103320	884279	960754	100
999	94.3	100.4	0.18	27.0	1426502	1401005	1020545	1279671	100
1185	94.2	100.5	0.17	29.1	1698309	1786351	1180724	1712895	100
1284	94.3	100.5	0.16	30.7	1874534	2139666	1315758	2127089	100
1387	94.3	100.4	0.13	30.7	1874534	2139666	1315758	2127089	100

α lo	5874	W/m^2K
G	579	kg/m^2s
p_atm	1.02	bar
Re_D	9272	

%diff Kandlikar (1998)	%diff Shah (1977)	%diff Jens & Lottes (1951)	Tfluid, z=2
36.6	7.3	62.0	100
40.9	13.0	62.1	100
30.7	14.6	51.3	100
24.3	20.6	42.3	100
13.3	21.9	28.8	100
8.0	26.2	19.9	100
1.8	28.5	10.3	100
5.2	30.5	0.9	100
14.1	29.8	13.5	100
14.1	29.8	13.5	100

heater power input, W	inlet temperature, deg C	outet temperature, deg C	flow rate, gpm	wall superheat, deg C	q" experimental, W/m^2	q" Kandlikar (1998)	q" Shah (1977)	q" Jens & Lottes (1951)	Tfluid, z=2
216	69.0	77.6	0.16	5.4	305217	7301	42775	2061	74.6
306	67.0	99.9	0.16	18.4	505143	428031	492116	272779	76.3
472	67.1	99.9	0.15	20.8	779529	643218	628344	444703	81.4
674	67.0	99.8	0.08	25.7	1077572	1312531	963936	1046579	86.8
829	67.0	99.8	0.07	28.8	1305152	1915570	1209375	1647396	91.0
999	66.8	99.8	0.05	31.8	1558359	2662731	1473597	2445870	95.4
1284	66.5	99.9	0.045	35.8	1975000	3957198	1869024	3934648	100

α lo	5870	W/m^2K
G	554	kg/m^2s
p_atm	1.02	bar
Re_D	6577	

%diff Kandlikar (1998)	%diff Shah (1977)	%diff Jens & Lottes (1951)	Tfluid, z=2
97.6	86.0	99.3	74.6
15.3	2.6	46.0	76.3
17.5	19.4	43.0	81.4
21.8	10.5	2.9	86.8
46.8	7.3	26.2	91.0
70.9	5.4	57.0	95.4
100.4	5.4	99.2	100

heater power input, W	inlet temperature, deg C	outet temperature, deg C	flow rate, gpm	wall superheat, deg C	q" experimental, W/m^2	q" Kandlikar (1998)	q" Shah (1977)	q" Jens & Lottes (1951)	Tfluid, z=2
141	90.8	94.3	0.27	5.3	125584	13628	75134	1960	92.2
176	91.1	95.4	0.28	8.9	182671	73528	206564	14818	93.0
216	90.8	95.8	0.32	10.6	260724	132979	294751	30171	93.2
259	90.7	97.5	0.27	11.2	336282	158150	327060	37148	94.3
306	90.6	98.7	0.27	11.6	422100	178368	351541	42917	95.2
358	90.6	99.3	0.27	12.3	508734	220627	399375	55391	96.2
413	90.5	100.4	0.27	13.0	592702	263989	444771	68700	97.0
472	90.5	100.4	0.27	14.1	696873	343529	520911	94234	98.3
536	90.4	100.2	0.26	15.3	790230	452304	614389	131089	99.4
603	90.2	100.2	0.25	16.1	893597	535005	679516	160354	100
674	90.5	100.2	0.27	17.2	998514	675576	781609	212158	100
749	90.6	100.2	0.27	18.3	1103777	830118	884441	271655	100
829	90.6	100.2	0.26	19.5	1237152	1008524	994024	343142	100
912	90.0	100.2	0.26	20.6	1357887	1224681	1116861	433190	100
999	90.7	100.2	0.24	22.2	1500888	1568968	1295847	583160	100
1090	90.4	100.2	0.24	23.4	1636525	1878922	1443878	724004	100
1185	90.4	100.2	0.24	25.1	1762011	2350912	1651684	947402	100

α lo	9974	W/m^{2}K
G	888	kg/m^{2}s
p_atm	1.02	bar
Re_D	13650	

%d Kandlikar (1998)	%d Shah (1977)	%d Jens & Lottes (1951)	Tfluid, z=2
89.1	40.2	98.4	92.2
59.7	13.1	91.9	93.0
49.0	13.1	88.4	93.2
53.0	2.7	89.0	94.3
57.7	16.7	89.8	95.2
56.6	21.5	89.1	96.2
55.5	25.0	88.4	97.0
50.7	25.3	86.5	98.3
42.8	22.3	83.4	99.4
40.1	24.0	82.1	100
32.3	21.7	78.8	100
24.8	19.9	75.4	100
18.5	19.7	72.3	100
9.8	17.8	68.1	100
4.5	13.7	61.1	100
14.8	11.8	55.8	100
33.4	6.3	46.2	100

Transient film boiling data

t, sec	flow, ml/sec	T2	T4	T10	T11	T12	T13	T14	T15	T16	T17	T18	T19	T20	T21	T25	T27
2	23.7	370.6	371.5	362.7	404.0	375.9	377.8	403.8	402.9	402.4	397.7	401.9	389.3	372.4	373.3	95.3	98.6
3	24.5	364.6	365.5	356.8	397.6	369.9	371.9	397.1	396.4	395.9	391.4	390.3	381.8	366.5	367.4	95.6	98.8
4	24.9	362.2	363.1	354.5	395.1	367.6	369.7	394.6	393.8	393.3	388.8	386.1	379.2	364.2	365.0	95.8	98.9
5	24.9	359.8	360.7	352.2	392.6	365.2	367.4	391.9	391.2	390.6	386.1	384.7	376.1	361.8	362.6	96.0	99.0
6	24.7	357.5	358.4	350.0	390.1	362.9	365.1	389.4	388.7	388.1	383.7	380.7	372.2	359.5	360.3	96.1	99.0
7	25.0	355.2	356.1	347.7	387.6	360.6	362.9	386.8	386.2	385.6	381.6	377.8	366.9	357.2	358.1	96.2	99.1
8	24.8	352.9	353.7	345.4	385.2	358.3	360.7	384.3	383.6	383.1	379.2	377.4	362.0	354.9	355.8	96.3	99.2
9	24.5	350.6	351.5	343.2	382.8	356.0	358.6	381.8	381.1	380.5	376.9	375.0	353.6	352.8	353.6	96.4	99.3
10	23.6	348.3	349.2	341.0	380.4	353.7	356.5	379.2	378.6	378.0	374.6	372.2	348.7	350.5	351.3	96.4	99.3
11	23.0	346.0	346.9	338.8	378.0	351.4	355.3	376.7	376.1	375.5	372.0	368.7	345.4	348.3	349.1	96.4	99.5
12	22.5	343.7	344.6	336.5	375.5	349.0	353.2	374.2	373.7	373.1	371.5	366.5	342.6	345.9	346.7	96.4	99.5
13	22.2	341.4	342.2	334.3	373.2	346.8	350.9	371.8	371.3	370.6	369.2	364.2	339.8	343.7	344.4	96.4	99.5
14	22.1	339.0	339.9	332.0	370.8	344.6	348.6	369.3	368.8	368.1	366.5	361.6	336.9	341.4	342.2	96.4	99.7
15	22.1	336.4	337.4	329.7	368.3	342.2	346.3	366.8	366.2	365.5	363.9	359.8	333.4	339.0	339.9	96.4	99.7
16	21.5	333.9	334.8	327.4	365.9	339.9	344.0	364.3	363.6	362.7	361.2	358.4	329.9	336.7	337.4	96.4	99.9
17	21.8	331.2	332.2	325.0	363.4	337.6	340.3	361.6	360.9	359.9	358.1	356.7	325.8	334.3	335.1	96.4	100.0
18	21.6	328.2	329.4	322.4	361.0	335.1	337.5	359.0	358.1	356.9	355.0	354.1	320.9	331.9	332.6	96.4	100.3
19	21.7	323.2	324.9	318.3	357.2	331.4	333.2	354.7	353.8	352.1	349.2	346.0	329.4	327.7	328.8	96.4	100.4
20	21.5	318.7	320.6	315.9	354.8	328.8	330.3	351.2	349.8	347.7	344.2	340.5	323.7	325.0	325.9	96.4	100.3
21	21.3	314.7	316.6	312.9	351.5	325.4	326.9	347.4	345.7	343.4	339.7	335.7	318.8	321.9	322.8	96.4	100.4
22	21.3	310.3	312.5	307.8	346.3	320.2	322.2	342.2	340.5	338.1	334.4	330.6	314.1	317.6	319.0	96.4	100.3
23	21.1	307.6	309.1	288.2	337.0	315.3	318.6	338.8	337.7	335.5	332.1	328.8	312.8	313.5	314.8	96.4	100.5
24	21.5	304.5	306.0	279.6	327.8	308.1	312.6	333.8	333.4	331.8	328.8	325.8	310.6	307.2	308.6	96.4	100.5
25	21.7	300.4	302.0	272.6	320.8	301.8	306.8	328.1	328.3	327.1	324.5	321.5	306.3	301.3	302.8	96.4	100.5
26	21.4	296.1	297.7	266.5	314.5	296.2	301.3	322.5	323.0	322.2	319.9	317.3	302.4	295.7	297.3	96.4	100.5
27	20.7	291.5	293.1	259.8	307.9	290.3	295.6	316.7	317.7	317.1	315.0	312.5	297.6	290.0	291.8	96.4	100.5
28	20.2	287.1	288.6	254.2	302.0	285.0	290.4	311.3	312.5	312.1	310.2	308.0	293.6	284.8	286.5	96.4	100.5
29	20.1	282.6	284.1	248.6	296.4	279.9	285.3	306.2	307.5	307.4	305.6	303.5	289.5	279.7	281.5	96.4	100.5
30	19.9	278.2	279.7	241.9	290.5	274.8	280.4	301.1	302.6	302.5	300.9	299.0	285.3	274.6	276.3	96.4	100.5
31	19.9	273.8	275.2	234.4	284.0	269.3	275.2	295.8	297.5	297.7	296.2	294.6	281.3	269.3	271.1	96.4	100.5
32	20.1	269.4	270.7	226.5	277.1	263.4	269.9	290.6	292.5	292.9	291.7	290.3	277.8	263.8	265.7	96.4	100.5
33	19.8	265.1	266.3	218.2	269.9	257.3	264.0	285.1	287.4	288.1	287.1	286.1	274.1	258.1	260.1	96.4	100.5
34	19.4	260.6	261.8	209.0	262.5	251.0	258.8	279.5	282.2	283.2	282.5	281.8	270.5	252.2	254.5	96.4	100.5
35	19.6	256.1	257.2	197.1	252.3	243.2	252.8	273.2	276.6	278.1	277.8	277.6	267.1	245.3	247.9	96.4	100.5
36	20.2	251.3	252.5	179.2	237.0	232.4	245.0	265.9	270.4	272.7	272.8	273.0	263.0	236.9	240.5	96.4	100.7
37	20.7	203.9	225.5	165.6	188.2	173.1	178.8	191.9	193.6	201.4	200.7	205.6	207.6	187.5	206.8	96.3	102.6
38	20.5	175.3	195.1	156.0	176.4	161.2	163.9	174.3	174.2	178.6	175.9	178.0	176.4	171.6	188.2	96.4	101.3
39	20.4	162.1	178.6	148.0	167.0	152.4	154.3	163.8	163.4	166.8	164.4	166.2	164.6	160.6	174.6	96.4	101.8
40	20.2	151.9	165.7	141.2	159.1	145.1	146.5	155.5	154.9	157.6	155.5	157.2	155.7	151.6	163.4	96.4	101.5
41	20.3	143.6	155.3	135.4	152.4	139.1	139.9	148.6	148.0	149.8	148.3	150.0	148.5	144.1	154.1	96.4	101.1
42	20.4	137.0	146.9	130.6	146.8	134.0	134.5	142.8	142.1	144.0	142.3	143.9	135.4	137.9	146.5	96.4	100.9
43	20.3	131.4	139.9	126.4	142.0	129.7	130.7	138.0	137.3	138.8	137.4	138.9	128.0	132.6	140.0	96.4	100.8
44	20.3	127.1	134.4	122.5	135.3	125.5	126.3	125.6	132.6	128.0	132.7	134.3	125.2	128.3	134.9	96.3	80.5

Appendix B

Detailed drawings

REV1:4/24/99 DTP

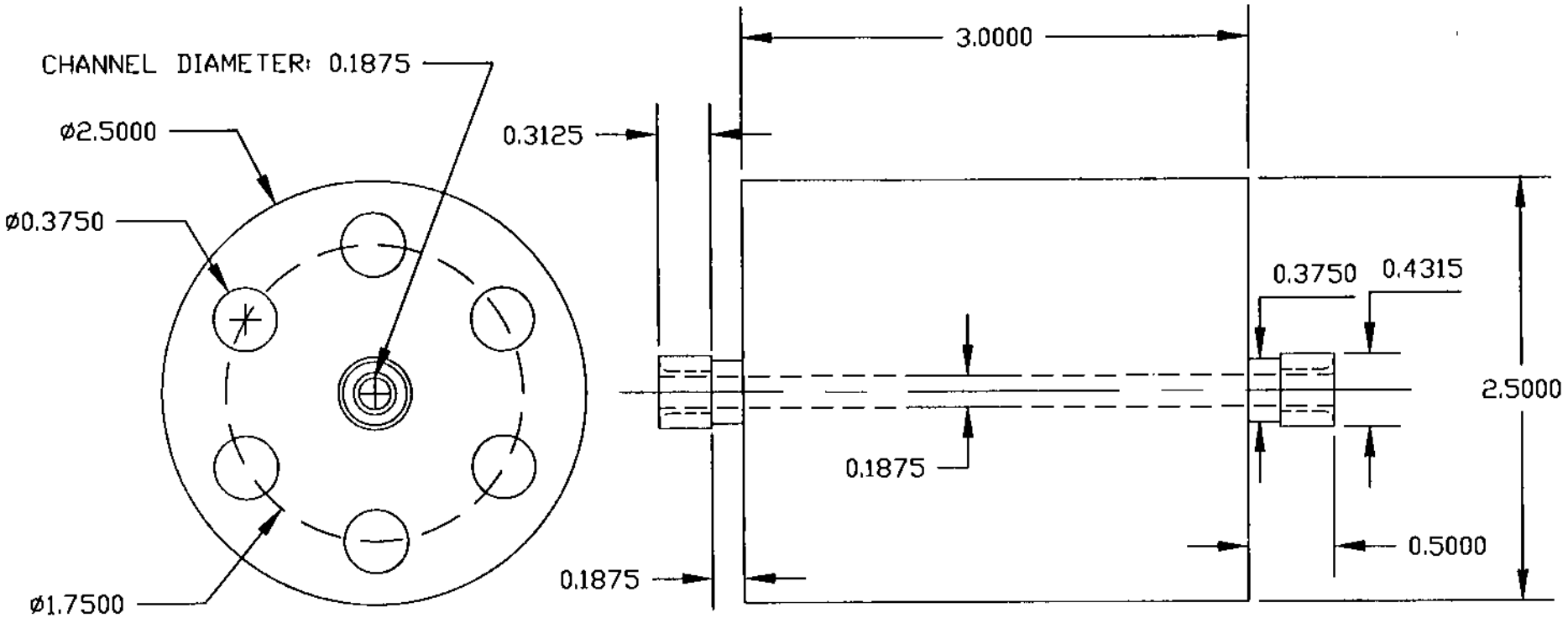

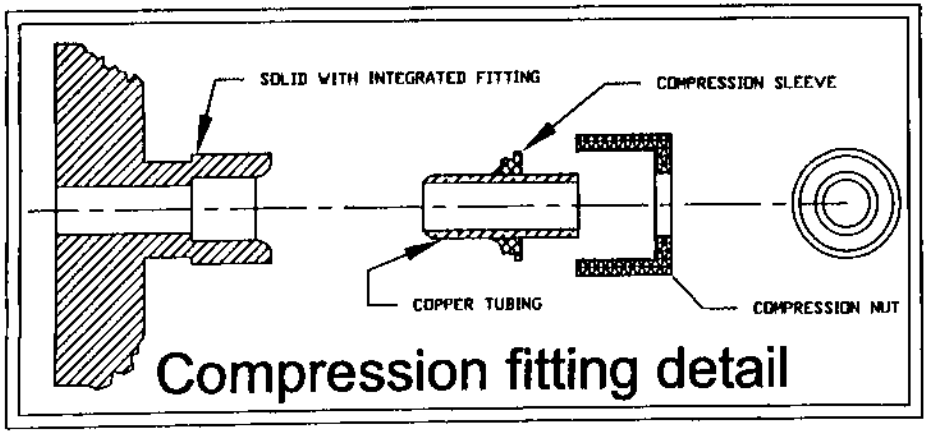

Compression fitting detail

ALL DIMENSIONS ARE IN INCHES (U.O.S.)

TEST SECTION LAYOUT GEOMETRY DETAILS

DRAWN BY: D.T. PETERS

REVISION 0: 4/23/99

R.I.T

FILENAME: TC_RADIAL_LOC.DWG

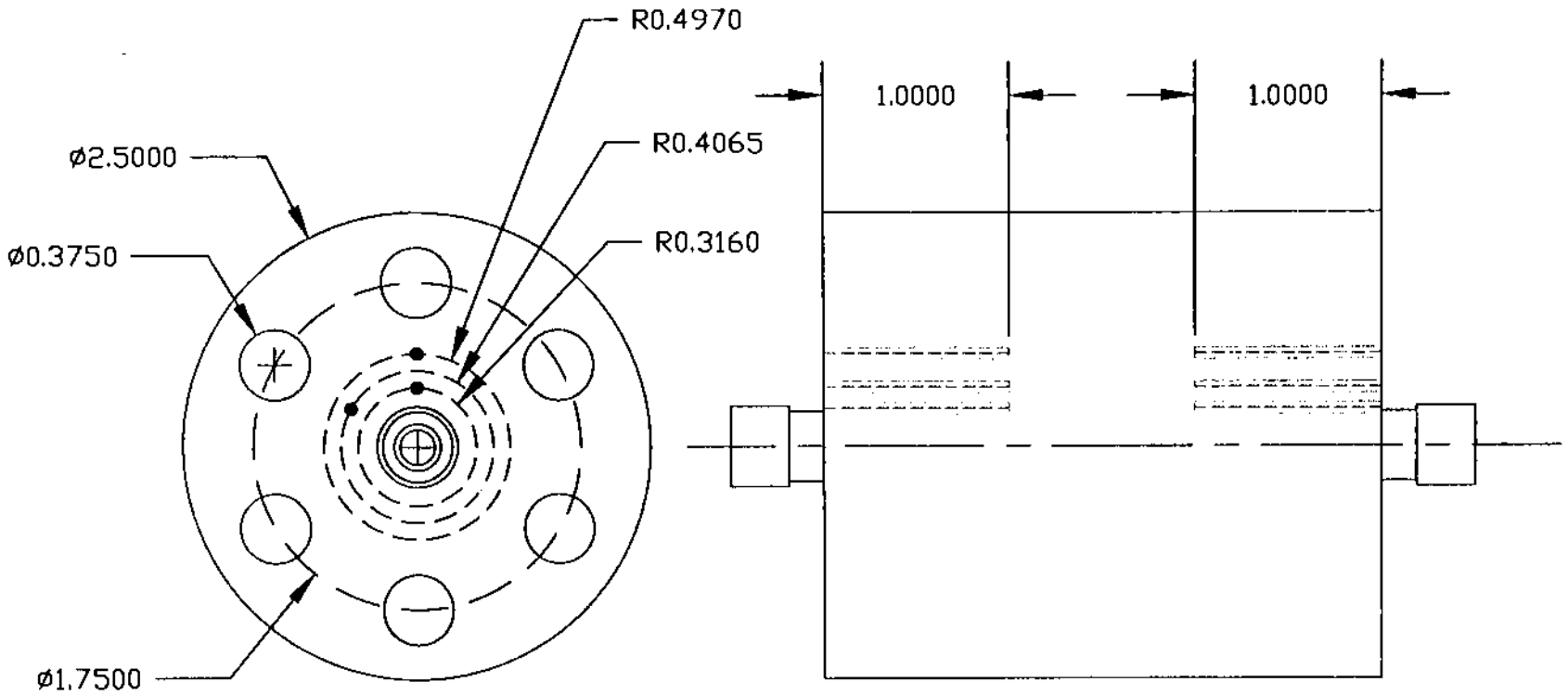

THERMOCOUPLE LAYOUT PATTERN (RADIAL DISTANCES) ARE THE SAME FOR BOTH TOP AND BOTTOM

ALL DIMENSIONS ARE IN INCHES (U.D.S)

TEST SECTION LAYOUT THERMOCOUPLE LOCATION DETAILS- RADIAL TRAVERSE

DRAWN BY: D.T. PETERS

REVISION 0: 4/23/99

R.I.T

REV1:4/24/99 DTP, FILENAME: TCsched.dwg

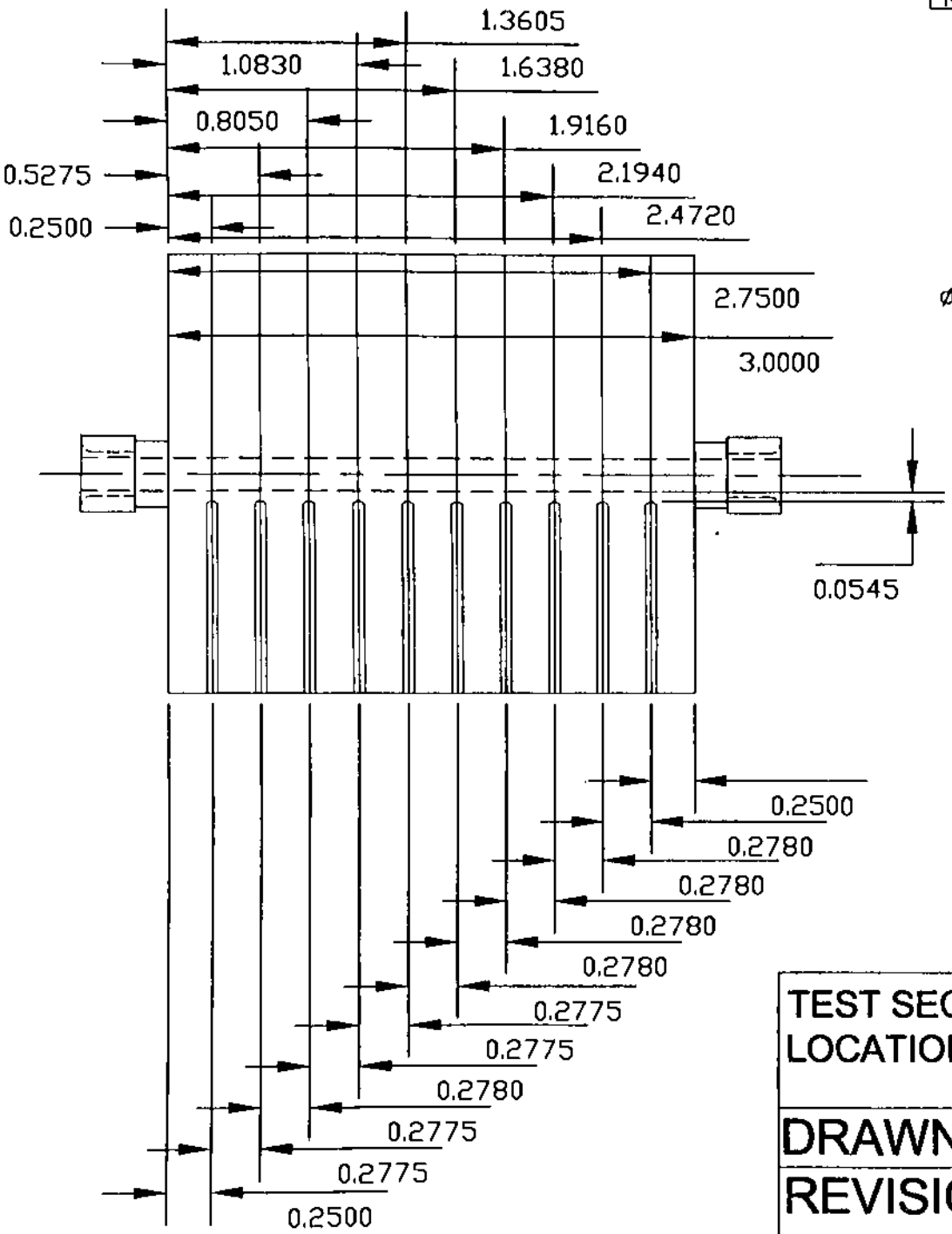

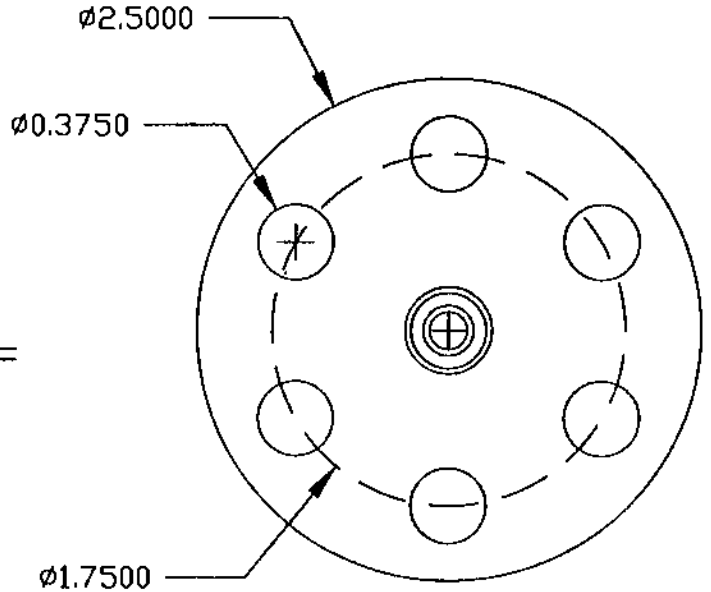

ALL DIMENSIONS ARE IN INCHES (U.S.)

TEST SECTION LAYOUT-THERMOCOUPLE LOCATION DETAILS, AXIAL TRAVERSE

DRAWN BY: D.T. PETERS

REVISION 0: 4/23/99

R.I.T

REV0:4/26/99 DTP,
FILENAME TC_numberscheme.DWG

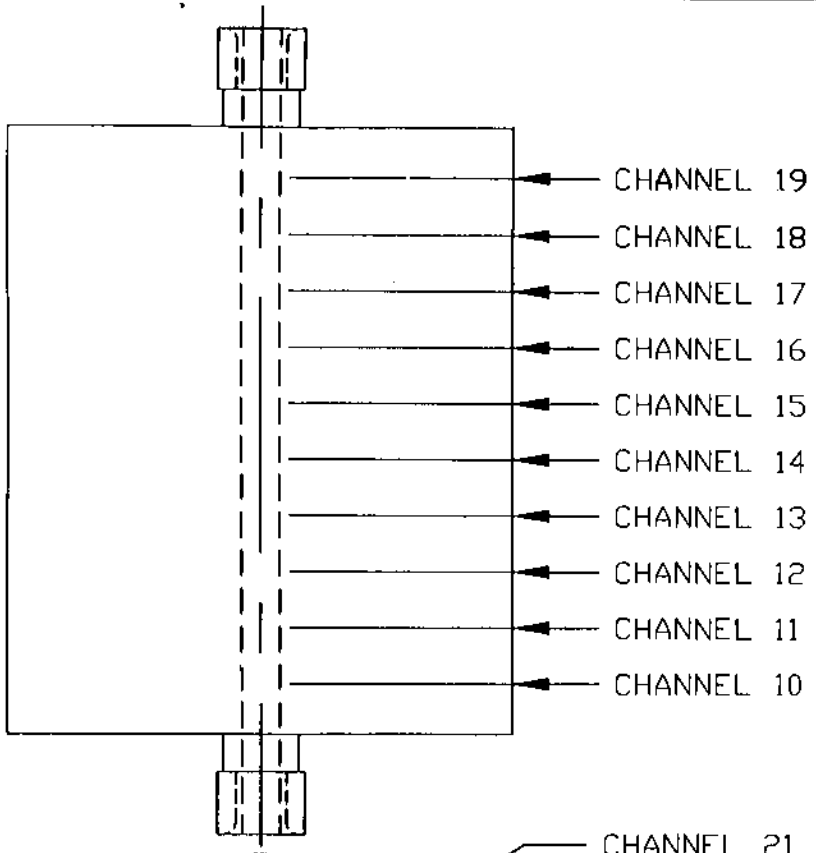

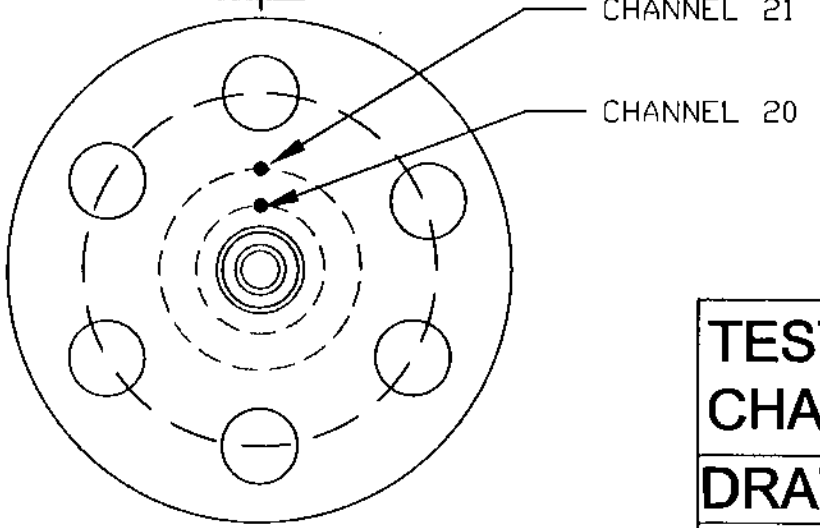

BOTTOM VIEW

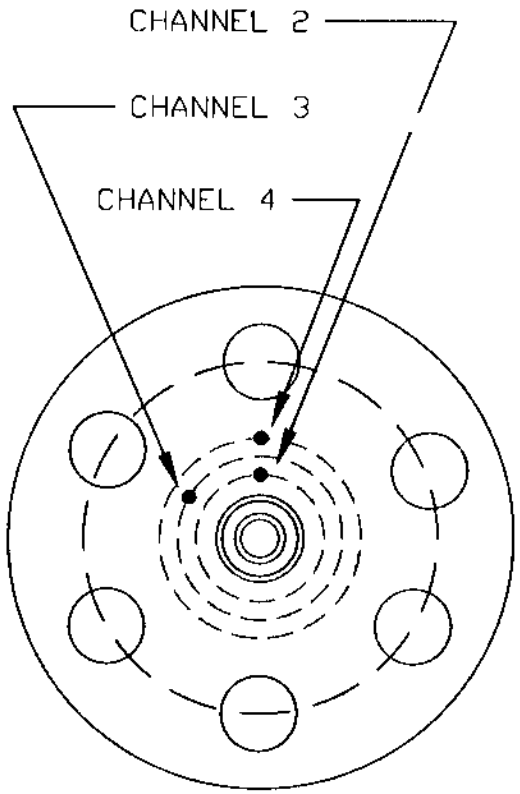

TOP VIEW

ALL DIMENSIONS ARE IN INCHES (U.O.S.)

TEST SECTION LAYOUT
CHANNEL NUMBER IDENTIFICATION

DRAWN BY: D.T. PETERS

REVISION 0: 4/26/99

R.I.T

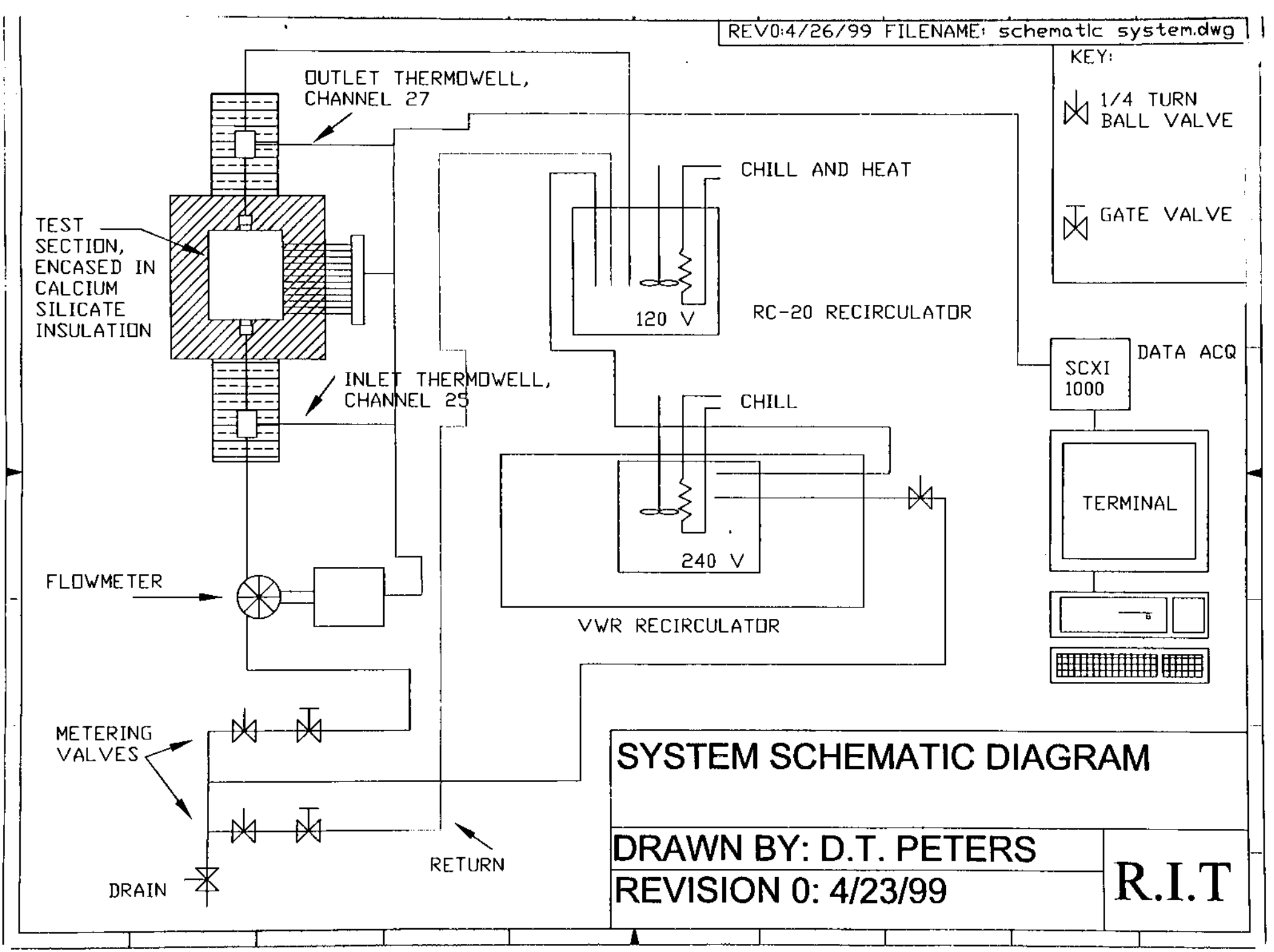
REV0:4/26/99 FILENAME: schematic system.dwg
KEY:
1/4 TURN BALL VALVE
GATE VALVE
OUTLET THERMOWELL, CHANNEL 27
CHILL AND HEAT
TEST SECTION, ENCASED IN CALCIUM SILICATE INSULATION
120 V
RC-20 RECIRCULATOR
SCXI 1000
DATA ACQ
INLET THERMOWELL, CHANNEL 25
CHILL
TERMINAL
FLOWMETER
240 V
VWR RECIRCULATOR
METERING VALVES
RETURN
DRAIN
SYSTEM SCHEMATIC DIAGRAM
DRAWN BY: D.T. PETERS
REVISION 0: 4/23/99
R.I.T

Appendix C

Temperature Profiles in the Axial Direction

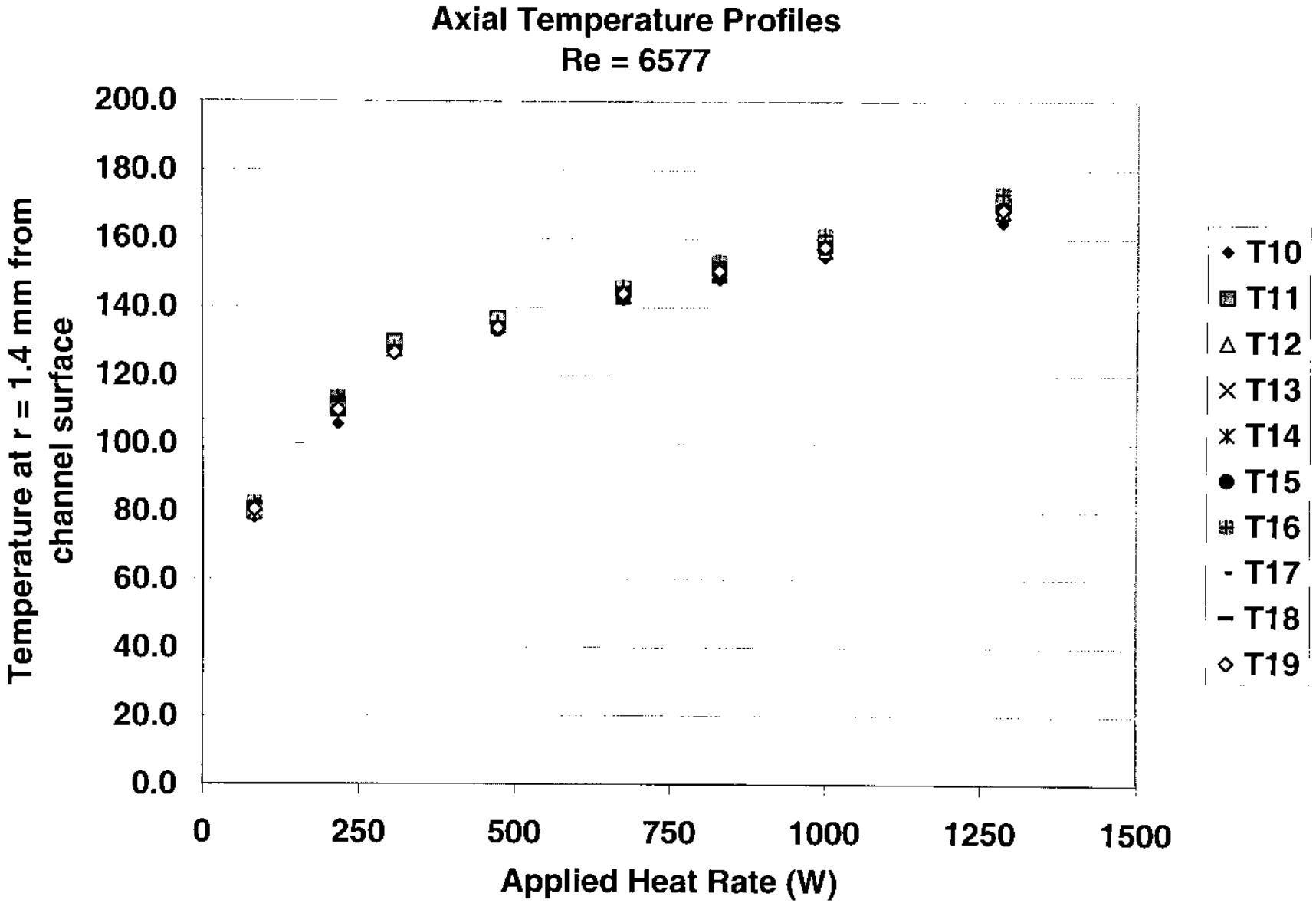
Axial Temperature Profiles
Re = 6577
Temperature at r = 1.4 mm from channel surface
200.0
180.0
160.0
140.0
120.0
100.0
80.0
60.0
40.0
20.0
0.0
0
250
500
750
1000
1250
1500
Applied Heat Rate (W)
T10
T11
T12
T13
T14
T15
T16
T17
T18
T19

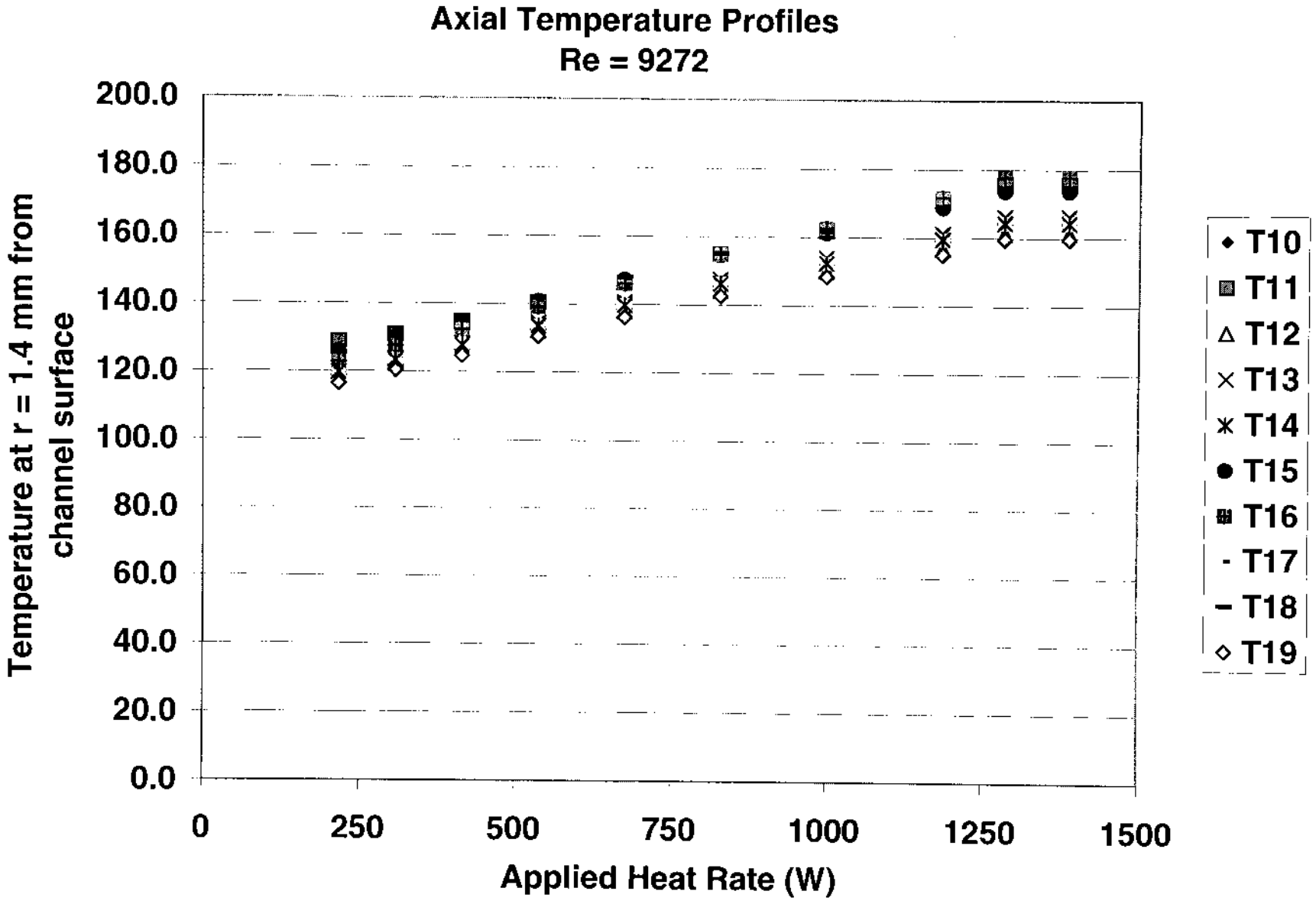
Axial Temperature Profiles
Re = 9272
Temperature at r = 1.4 mm from channel surface
200.0
180.0
160.0
140.0
120.0
100.0
80.0
60.0
40.0
20.0
0.0
0
250
500
750
1000
1250
1500
Applied Heat Rate (W)
T10
T11
T12
T13
T14
T15
T16
T17
T18
T19

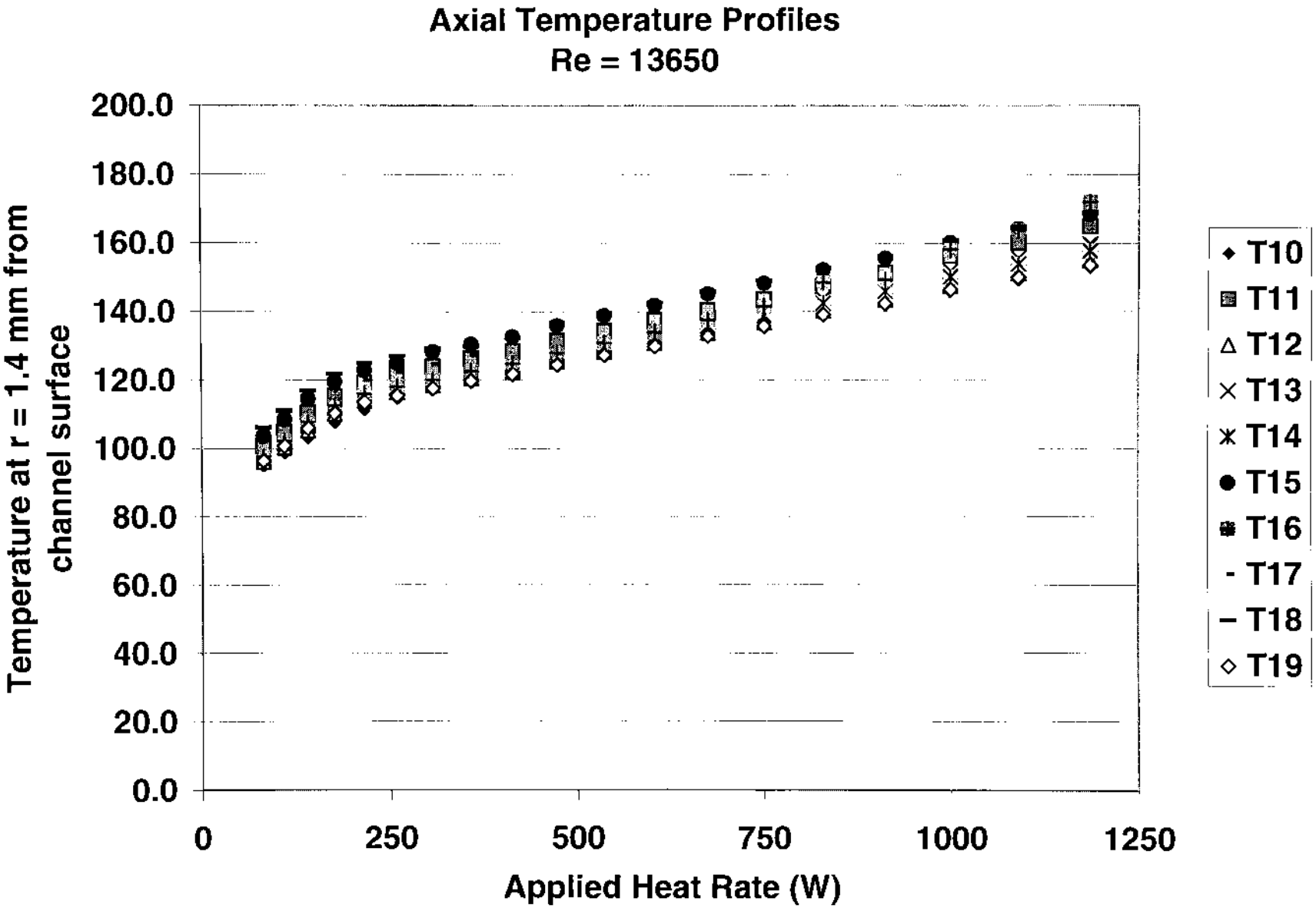
Axial Temperature Profiles
Re = 13650
Temperature at r = 1.4 mm from channel surface
200.0
180.0
160.0
140.0
120.0
100.0
80.0
60.0
40.0
20.0
0.0
0
250
500
750
1000
1250
Applied Heat Rate (W)
T10
T11
T12
T13
T14
T15
T16
T17
T18
T19